Supervised-Learning-Enabled EM-Driven Development of Low Scattering Metasurfaces

Muhammad Abdullah

Doctor of Philosophy

May 2022

Electrical Engineering

Reykjavík University

PhD Dissertation

Supervised-Learning-Enabled EM-Driven Development of Low Scattering Metasurfaces

Dissertation of 30 ECTS credits submitted to the Department of Engineering
at Reykjavík University in partial fulfilment of
the requirements for the degree of
Doctor of Philosophy (PhD) in Electrical Engineering

May 2022

Thesis Supervisors:

   Slawomir Koziel, Professor
   Reykjavík University, Reykjavík, Iceland

   Anna Pietrenko-Dabrowska, Associate Professor
   Gdansk University of Technology, Poland

Thesis Committee:

   Slawomir Koziel, Professor
   Reykjavík University, Reykjavík, Iceland

   Anna Pietrenko-Dabrowska, Associate Professor
   Gdansk University of Technology, Poland

   Ágúst Valfells, Dean of Department of Engineering
   Reykjavík University, Reykjavík, Iceland

   Ubaid Ullah, Assistant Professor
   Al-Ain University, UAE

Thesis Examiner:

   Adam Narbudowicz, Senior Research Fellow
   Trinity College Dublin, Ireland

Supervised-Learning-Enabled EM-Driven Development of Low Scattering Metasurfaces

Muhammad Abdullah

May 2022

Abstract

The recent advances in the development of coding metasurfaces created new opportunities to elevate the stealthiness of combat aircrafts. Metasurfaces, composed of optimized geometries of meta-atoms arranged as periodic lattices, are devised to obtain desired electromagnetic (EM) scattering characteristics, and have been extensively exploited in stealth applications to reduce radar cross section (RCS). They rely on the manipulation of backward scattering of electromagnetic (EM) waves into various oblique angles. Despite potential benefits, a practical obstacle hindering widespread metasurface utilization is the lack of systematic design procedures. Conventional approaches are largely intuition-inspired and demand heavy designer's interaction while exploring the parameter space and pursuing optimum unit cell geometries. Another practical obstacle that hampers efficient design of metasurfaces is implicit handling of RCS performance. To achieve essential RCS reduction, the design task is normally formulated in terms of phase reflection characteristics of the unit cells, whereas their reflection amplitudes—although contributing to the overall performance of the structure—is largely ignored. A further practical issue is insufficiency of the existing performance metrics, specifically, monostatic and bistatic evaluation of the reflectivity, especially at the design stage of metasurfaces. Both provide a limited insight into the RCS reduction properties, with the latter being dependent on the selection of the planes over which the evaluation takes place. As a consequence of raised concerns, the existing design methodologies are still insufficient, especially in the context of controlling the EM wavefront through parameter tuning of unit cells. Furthermore, they are unable to determine truly optimum solutions. Therefore, we have introduced a novel machine-learning-based framework for automated and computationally efficient design of metasurfaces realizing broadband RCS reduction. We have employed a three-stage design procedure involving global surrogate-assisted optimization of the unit cells, followed by their local refinement. In its final stage, a direct EM-driven maximization of the RCS reduction bandwidth has been performed, facilitated by appropriate formulation of the objective function involving regularization terms. Moreover, to handle the combinatorial explosion in the design closure of multi-bit coding metasurfaces, a sequential-search strategy has been developed that enabled global search capability at the concurrent unit cell optimization stage. Latterly, the metasurface design task with explicit handling of RCS reduction at the level of unit cells has been introduced that has accounted for both the phase and reflection amplitudes of the unit cells. The design objective has been defined so as to directly optimize the RCS reduction bandwidth at the specified level (e.g., 10 dB) w.r.t. the metallic surface. The appealing feature of the said framework has consisted in its ability to optimize the RCS reduction bandwidth directly at the level of the entire metasurface as opposed to merely optimizing unit cell geometries. Besides, the obtained design has required minimum amount of tuning at the level of the entire metasurface. Lastly, a new performance metric for evaluating scattering characteristics of a metasurface, referred to as Normalized Partial Scattering Cross Section (NPSCS), has been proposed. The metric involved integration

of the scattered energy over a specific solid angle, which allows for a comprehensive assessment of the structure performance in a format largely independent of the particular arrangement of the scattering lobes. Our design methodologies have been utilized to design several instances of novel scattering metasurface structures with the focus on RCS reduction bandwidth enhancement and the level of RCS reduction. Experimental validations confirming the numerical findings have been also provided. To the best of the author's knowledge, the presented study is the first systematic investigation of this kind in the literature and can be considered a step towards the development of efficient, low-cost, and more high performing scattering structures.

The undersigned hereby certify that they recommend to the Department of Engineering, School of Technology, Reykjavík University that this dissertation, entitled **"Supervised-Learning-Enabled EM-Driven Development of Low Scattering Metasurfaces"** submitted by **Muhammad Abdullah** be accepted as partial fulfilment of the requirements for the degree of **Doctor of Philosophy (Ph.D.) in Engineering**.

...............━━━━━━━━━━━━━━
Date: 04-05-2022

...............━━━━━━━━━━━━━━━..
Slawomir Koziel, Professor, Supervisor
Reykjavík University, Iceland

...............━━━━━━━━━━━━━━━..
Anna Pietrenko-Dabrowska, Associate Professor, Supervisor
Gdansk University of Technology, Poland

...............━━━━━━━━━━━━━━━..
Ágúst Valfells, Department of Engineering
Reykjavík University, Iceland

...............━━━━━━━━━━━━━━━..
Ubaid Ullah, Assistant Professor
Al-Ain University, UAE

...............━━━━━━━━━━━━━━━..
Adam Narbudowicz, Senior Research Fellow
Trinity College Dublin, Ireland

The undersigned hereby grants permission to the Reykjavík University Library to reproduce single copies of this Dissertation entitled **Supervised-Learning-Enabled EM-Driven Development of Low Scattering Metasurfaces** and to lend or sell such copies for private, scholarly or scientific research purposes only.

The author reserves all other publication and other rights in association with the copyright in the Dissertation, and except as herein-before provided, neither the Dissertation nor any substantial portion thereof may be printed or otherwise reproduced in any material form whatsoever without the author's prior written permission.

Date: 04-05-2022

……………━━━━━━━━━━━━━━━━━━━━━━━━━━━………………………………………………………
Muhammad Abdullah
Doctor of Philosophy

To my beloved parents, siblings, and fiancée

For their endless love, support and encouragement

Acknowledgments

This work would not have been possible without constant support of people who helped me overcome research failures, interpersonal difficulties and disapproval. I would like to acknowledge people and institutions that have had the greatest impact on my work.

In the first place, I would like to express deep gratitude to Prof. Sławomir Kozieł, supervisor of this doctoral work. His constant support, guidance, and cheerful responses to my endless 'knock, knocks' on his doors have allowed me to vastly develop my research skills and understand enigma of contemporary surrogate-assisted optimization techniques and their applications in high-frequency design. I appreciate his invaluable research advice, inspiring discussions, open-door mentality, general kindness, and great patience very much. His trust in my abilities allowed me to conquer all the difficulties came across during this research, hence achieving the required goals.

I would also like to convey my sincere gratitude to my co-supervisor, Prof. Anna Pietrenko-Dabrowska, for her help in my papers and discussions.

Finally, I wish to express my heartfelt thanks and gratitude to my family. They have always done their best to provide me every possible facility of life. Their never-ending love, unconditional support and advice over the years have shaped me into the human being I am today.

I would like to thank Computer Simulation Technology AG, Darmstadt, Germany, for making CST Microwave Studio available.

Preface

This dissertation is the original work of the author, Muhammad Abdullah. A portion of the thesis (Chapter 3 through Chapter 7) is based upon the journal papers, published during the Ph.D. study. Note that these papers appear as per their online version in the chapters. The overall list of journal papers throughout this study is listed below.

Journal papers:

1. M. Abdullah and S. Koziel, "Surrogate-Assisted Design of Checkerboard Metasurface for Broadband Radar Cross-Section Reduction," *IEEE Access*, vol. 9, pp. 46744-46754, 2021.

2. S. Koziel and M. Abdullah, "Machine-Learning-Powered EM-Based Framework for Efficient and Reliable Design of Low Scattering Metasurfaces," *IEEE Trans. Microwave Theory and Tech.*, vol. 69, no. 4, pp. 2028-2041, April 2021.

3. M. Abdullah and S. Koziel, "Supervised-Learning-Based Development of Multi-Bit RCS-Reduced Coding Metasurfaces," *IEEE Trans. Microwave Theory and Tech.*, vol. 70, no. 1, pp. 264-274, Jan. 2022.

4. S. Koziel, M. Abdullah, and S. Szczepanski, "Design of High-Performance Scattering Metasurfaces through Optimization-Based Explicit RCS Reduction," *IEEE Access*, vol. 9, pp. 113077-113088, 2021.

5. M. Abdullah, S. Koziel, and S. Szczepanski, "Normalized Partial Scattering Cross Section for Performance Evaluation of Low-Observability Scattering Structures," *Electronics*, vol. 10, pp. 37656-37667, 2021.

6. M. Abdullah and S. Koziel, "A Novel Versatile Decoupling Structure and Expedited Inverse Model-Based Re-Design Procedure for Compact Single-and Dual-Band MIMO Antennas," *IEEE Access*, vol. 9, pp. 37656-37667, 2021.

Contents

List of Figures

List of Acronyms

AF   Array Factor

AI   Artificial Intelligence

AMC   Artificial Magnetic Conductor

CST   Computer Simulation Technology

EBG   Electromagnetic Bandgap

EA   Evolutionary Algorithms

EM   Electromagnetic

FEM   Finite Element Method

FSS   Frequency Selective Surface

GA   Genetic Algorithm

HIS   High Impedance Surface

ML   Machine Learning

PEC   Perfect Electric Conductor

PMC   Perfect Magnetic Conductor

PR   Polarizer Rotator

PSO   Particle Swarm Optimization

RCS   Radar Cross Section

RMSE   Root Mean Squared Error

SBO   Surrogate-Based Optimization

VNA   Vector Network Analyzer

List of Symbols

U	Objective function
GHz	Gigaherz, 10^9 Hertz
dB	Decibels
$\boldsymbol{R}_f$	Response vector of an EM-simulation model
$\boldsymbol{x}$	Vector of designable variables
∇	Gradient
λ	Wavelength
μ	Permeability
$\boldsymbol{x}^*$	Optimum design
ρ	Gain ration for trust-region framework
P	Population (in metaheuristic algorithms)
σ	Scattering cross section
$S(\boldsymbol{x})$	Response vector of a surrogate model
$C_{eq.l}$	Equality constraints
$C_{ineq.l}$	Inequality constraints
f	Frequency
ε_r	Relative permittivity

Chapter 1

1 Introduction

1.1 Introduction

The observed rapid advancements in the detection and stealth technology, has made the improved stealth performance of the military targets is highly desirable. With the advent of different types of radars featuring advanced electronic equipment, the research on reducing the observability of the military targets has been rapidly evolving. Under the impetus of the development of science and technology, the contemporary wars have been gradually transformed into the modern ones largely dependent on electronic information. In order to master the initiative in modern warfare, and to improve the survival rate of military targets, i.e., aircraft, missiles, tanks, and ships, it is imperative to develop target stealth technology. The improvement of the stealth technology can reduce the detection range of the target, the detection probability of the target, and improve the lethality and survivability of the weapons in the war, which is of great strategic significance.

Nowadays, many countries are conducting research on the fifth-generation fighter jets to improve their air superiority on the battlefield. The important aspect to improve the performance of the fighter jets is to reduce their observability from the enemy radars. Initially, the research on the stealth technology of the military targets started in America. As early as the 1950s, different technologies were used to improve the stealth performance of the aircraft. In 1945, a "quasi" type stealthy aircraft was produced, namely, the U-2 high flying reconnaissance aircraft [1]. It was small in size and passive in the airborne navigation system. Its fuselage was coated with the radar absorbing materials (RAM) to reduce the scattering of radar waves. The SR-71 reconnaissance plane produced in the 1960s [1], with the wing body fusion technique for the first time, replacing the right angle reflection structure with a smooth transition, which significantly reduced the radar cross-section of the entire machine. The F-117 was the most famous stealthy jet due to its special shape, which was developed in the 1970s by the US [2]. The polyhedral fuselage technique was used to reduce the RCS, but compared with the later B-1B and B-2 bombers (aircraft) [3], the stealth performance was relatively poor. In the 1980s and 1990s, the stealth performance of the aircraft improved more significantly, as the new stealth aircrafts such as F-22 Raptor [4] and F-35 Flash [4] were introduced. Stealth performance of these aircrafts increased their superiority and advantage over other fighter aircrafts. In 2010, Chinese armed forces deployed J-20 [5] as a stealth aircraft for the offensive and defensive operations. J-20 has the ability of high stealth, high sense of potential, and high manoeuvrability. It has a delta flyer shape or triangular designated form. Overall, its weight and stealth performance is similar to US F-35 [4]. According to the defence experts, F-35 (US), SU-57 (Russian), and J-20 (Chinese) are the best currently available stealth aircrafts. Figure 1.1 shows the photographs of the J-20 and F-35 stealth aircrafts.

The stealth performance of the object is generally determined by the scattering ability of its surface. If the surface of the object scatters more, it means that the object has a lower stealth

performance as more of the incident signals are transmitted back. Similarly, if the surface of the object scatters less, it indicates that the surface has a stealth property. The scattering from the surface of the targets is generally defined in terms of the radar cross section (RCS). The scattering ability of the target to the incident electromagnetic wave (EM) determines the stealth performance of the target. The scattering ability is usually described quantitatively by RCS, so it is necessary to reduce the target RCS to achieve the goal of invisibility to radars. In the recent years, the main methods for reducing RCS have been as follows: geometry modification technique, adding absorbing material, and active and passive cancellation of EM waves [6], [7]. In the modification technique, the structure of the target is modified in order to reduce the RCS. With the use of absorbing material, the RCS of the target can also be reduced by absorbing the incoming EM waves. These two techniques have been effectively and commonly used in the past.

The state-of-the-art approach proposed for RCS reduction is based on destructive interference, as conceptually shown in Fig. 1.2. The original idea was to bring together artificial magnetic conductor (AMC) with 0° and perfect electric conductor (PEC) with 180° reflection phase coefficient in a chessboard-like configuration [8]. As the incident wave impinges on the chessboard-like surface, the induced current densities re-radiate in phase and out of phase. Thus, by using the array theory the superposition of the reflected fields becomes zero at $\theta = 0°$, [8].

(a) J-20
(b) F-35

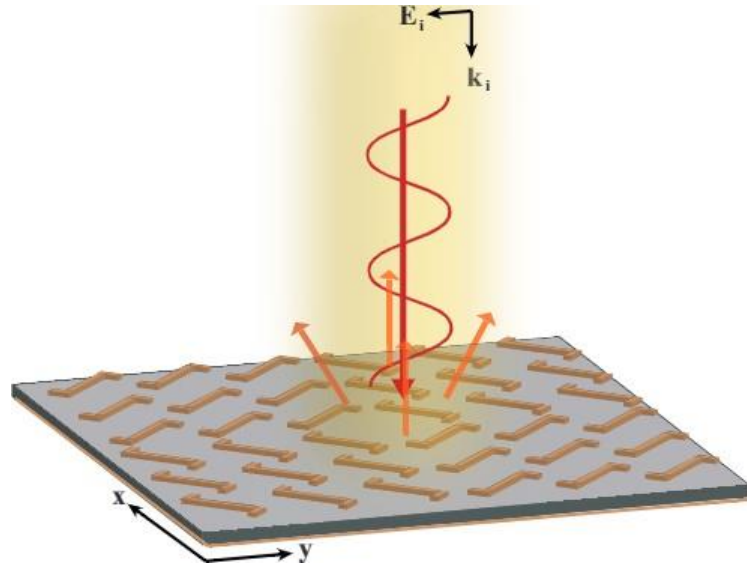Figure 1.1: Photographs of the stealth aircrafts J-20 and F-35 [84]

Figure 1.2: Scattering concept based on the method of destructive interference [84]

Alongside improving the RCS reduction bandwidth of artificially-engineered surfaces, some preliminary studies have been also carried out to facilitate and optimize the design procedure by applying heuristic methods [9], [10]. Although such algorithms are capable of solving complex optimization tasks, they often end up at local extrema. Notwithstanding, the broadband RCS reduction is a necessity to improve the stealth performance of the system. In the recent years, the researchers have shown a great interest in reducing the RCS of the artificially engineered surfaces to achieve low observability from the radars.

1.2   Contribution of the Thesis

The contributions of this thesis have been described in five journal publications that constitute Chapters 3 through 7. These are publications selected from the overall record of the candidate (six journal articles) prepared during his Ph.D. study. Their common theme is the development of low scattering metasurfaces with the emphasis on design optimization.

- **Paper #1:** Metasurfaces have been extensively exploited in stealth applications to reduce radar cross section (RCS). We propose a surrogate-based approach for rapid design optimization of checkerboard metasurfaces. Our methodology involves fast metamodels, and a combination of surrogate-assisted global optimization with local, gradient-based tuning. It permits an efficient control of the EM wave reflection characteristics, and ensures arriving at that the globally optimum solution within the assumed parameter space. The framework is employed to develop a novel broadband checkerboard metasurface. According to our conducted experiment, the proposed structure outperforms the designs reported in the literature.

    - **Bibliographic Note:**
      M. Abdullah and S. Koziel, "Surrogate-Assisted Design of Checkerboard Metasurface for Broadband Radar Cross-Section Reduction," *IEEE Access*, vol. 9, pp. 46744-46754, 2021.

- **Paper #2:** We introduce a novel machine-learning-based framework for automated and computationally efficient design of metasurfaces realizing broadband RCS reduction. Our methodology is a three-stage procedure that involves global surrogate-assisted optimization of the unit cells, followed by their local refinement. The last stage is direct EM-driven maximization of the RCS reduction bandwidth, facilitated by appropriate formulation of the objective function involving regularization terms. The appealing feature of the proposed framework is that it optimizes the RCS reduction bandwidth directly at the level of the entire metasurface as opposed to merely optimizing unit cell geometries. We applied the proposed framework to several metasurface designs reported in the literature; it leads to the RCS reduction bandwidth improvement by 15 to 25 percent as compared to the original designs.

  o **Bibliographic Note:**

  S. Koziel and M. Abdullah, "Machine-Learning-Powered EM-Based Framework for Efficient and Reliable Design of Low Scattering Metasurfaces," *IEEE Trans. Microwave Theory and Tech.*, vol. 69, no. 4, pp. 2028-2041, April 2021.

- **Paper #3:** This study is concerned with the development and design optimization of coding metasurfaces featuring broadband RCS reduction. Here, we adopt a two-stage optimization procedure that involves data-driven supervised-learning, sequential-search strategy, and direct EM-based design closure of the entire metasurface oriented toward maximizing the RCS reduction bandwidth. By applying the aforementioned algorithmic framework, a novel two-bit coding metasurface has been developed. It has been validated using simulation and measurement results that the proposed metasurface outperforms similar structures in literature in terms of all of the considered performance figures.

  o **Bibliographic Note:**

  M. Abdullah and S. Koziel, "Supervised-Learning-Based Development of Multi-Bit RCS-Reduced Coding Metasurfaces ," *IEEE Trans. Microwave Theory and Tech.*, vol. 70, no. 1, pp. 264-274, Jan. 2022.

- **Paper #4:** One of the practical obstacles hindering efficient design of metasurfaces is implicit handling of RCS performance. In this study, we presented a novel formulation of the metasurface design task with explicit handling of RCS reduction at the level of meta-atoms. Our methodology accounts for both the phase and reflection amplitudes of the unit cells. The design objective is defined to directly optimize the RCS reduction bandwidth at the specified level (e.g., 10 dB) w.r.t. the metallic surface. The benefits of the presented scheme are twofold: (i) it provides a reliable insight into the metasurface properties even though the design process is carried out at the level of meta-atoms, (ii) the obtained design requires minimum amount of tuning at the level of the entire metasurface.

o **Bibliographic Note:**

S. Koziel, M. Abdullah, and S. Szczepanski, "Design of High-Performance Scattering Metasurfaces through Optimization-Based Explicit RCS Reduction," *IEEE Access*, vol. 9, pp. 113077-113088, 2021.

- **Paper #5:** A practical obstacle in the development of diffusion metasurfaces is the insufficiency of the existing performance metrics, specifically, monostatic and bistatic evaluation of the reflectivity. Both provide a limited insight into the metasurface properties. We proposed a novel performance metric, referred to as Normalized Partial Scattering Cross Section (NPSCS), for evaluating backward scattering properties of a metasurface. The metric involves integration of the scattered energy over a specific solid angle, which allows for a comprehensive assessment of the structure performance in a format largely independent of the particular arrangement of the scattering lobes. It has been demonstrated using two specific application examples that the introduced metric can be used to discriminate between the various surface configurations (e.g., checkerboard versus random), which cannot be conclusively compared using traditional methods.

o **Bibliographic Note:**

M. Abdullah, S. Koziel, and S. Szczepanski, "Normalized Partial Scattering Cross Section for Performance Evaluation of Low-Observability Scattering Structures," *Electronics*, vol. 10, pp. 37656-37667, 2021.

1.3   Thesis Organization

The remainder of the thesis is organized into six chapters. Chapter 2 delivers a brief background on the radar systems, RCS reduction, and the key components of design process, namely periodic structures and surrogate-based modelling. A literature review is provided as well. In Chapter 3, the surrogate-assisted design procedure, enabling the development of high-performance checkerboard metasurfaces is described, and its main components are outlined. Within this chapter, a detailed discussion on the utility of the proposed methodology is provided, supported by the design of a novel checkerboard metasurface for broadband RCS reduction. Moreover, simulations and measurements are conducted for both monostatic and bistatic RCS reduction to verify the efficiency and feasibility of the proposed design procedure. Chapter 4 extends the previous design procedure, and introduces a three-stage design optimization strategy that involves machine-learning at the level of the unit cell design, followed by a gradient-based local refinement. The last stage is direct EM-driven maximization of the RCS reduction bandwidth at the level of the entire metasurface, facilitated by appropriate formulation of the objective function, which involves the regularization terms. Moreover, the practical utility of the introduced algorithmic framework is demonstrated in the context of broadband scattering metasurface design using three application examples. In the last part, a novel metasurface architecture is introduced featuring over one hundred percent relative RCS reduction bandwidth. In Chapter 5, a systematic and efficient approach to globally optimum multi-bit coding metasurface design is introduced, based on the supervised-learning based algorithms. A detailed discussion of the data-driven modelling procedure and formulating the design problem in a sequential manner is addressed. Towards the end, a novel

high-performance two-bit coding metasurface is presented that offers broadband RCS reduction as well as exhibits angularly-invariant characteristics. In Chapter 6, a novel metasurface design task formulation is presented. It involves explicit handling of RCS reduction at the level of meta-atoms and it accounts for both the phase and reflection amplitudes of the unit cells in the formulation. A detailed discussion on the novel way of formulating the design problem as well as surrogate-based modelling procedure is provided. In the latter part, a discussion about the utility of the new methodology as well as benchmarking its performance against standard methodologies is given. Simulations and measurements results are also presented to verify the efficacy of the new design methodology. Chapter 7 introduces a new performance metric, referred to as Normalized Partial Scattering Cross Section (NPSCR), for evaluating backward scattering properties of metasurfaces. Further, the underlying concepts behind RCS of scattering metasurfaces, as well as is relation to monostatic and bistatic characteristics are investigated. Later on, a formal definition and mathematical formulation of a novel performance metric is given. Furthermore, the significance of the metric is demonstrated through benchmarking of two specific metasurface architectures.

Chapter 8 concludes the thesis by summarizing the conducted works over the course of this Ph.D. work, highlighting possible challenges and open questions, as well as drawing potential directions for the future research.

Chapter 2

2   Background and Literature Review

Radar Cross-Section (RCS) is an essential object signature that determines the detectability of an object by a radar. Reducing RCS is a principal demand in military and civil applications. The concept of RCS reduction (or stealth) has been a topic of attention since World War II [11], and has faced many challenges up to now. In 2007, Paquay *et al.* proposed an effective method for reducing RCS of an object based on the theory of destructive interference [12]. To date, the principle of RCS reduction based on the idea of destructive interference has been widely acknowledged; this approach has been based upon the design of unit cells with 180° reflection phase difference, and employing them in a configuration that results in far-field power cancellation. In terms of practical realization of this concept, artificial magnetic conductor (AMC) and similar periodic structures can be precisely designed to satisfy the 180° reflection phase difference condition. Machine-learning-based modelling techniques can be implemented to facilitate the design process, and to optimize the structures implementing RCS reduction to ensure their best possible performance. This chapter provides an overview of the main components of the research conducted under this Ph.D. work, and also reviews some of the widely utilized approaches adopted by other researchers to accomplish RCS reduction of targets.

2.1   Radar Systems

Although utilization of radio waves for communication started in the early 1890s, the radar, as we know it now, was formally introduced in the time of World War II. Radar detection holds several advantages over other systems. Since radio waves experience a much lower atmospheric attenuation during propagation as compared to optical waves, radar system has a potential to detect a target long before it becomes optically detectable. Furthermore, as it utilizes radio waves and antennas, it is just as effective at night (dark) as during the daylight. An additional advantage is that the radar system does not demand auxiliary sources of energy, other than radar transmitters and receivers, to illuminate the target: being an active-device system, it monitors its own electromagnetic echo.

An understanding of electromagnetic theory and microwave engineering is instrumental in designing or countering radar systems. The fundamentals thereof are out of the scope of this work. The necessary material on electromagnetic theory and microwave engineering can be found in [13]-[17]. Additionally, an exposition of a basic knowledge of antenna theory has been provided in [18].

For a precise target detection, radar systems necessitate highly-directional radiation beams for both the transmitter and the receiver. Typically, realization of such challenging requirements is handled by employing large arrays of antenna elements. In particular, radiation patterns featuring narrow beams and low side lobe levels can be implemented using phased antenna arrays. As the pattern properties depend on the spacing between the individual antenna

elements and the relative phase of their excitation, the main radiating beam can be scanned (at a considerably high scanning rate) from one direction (angle) to another without any mechanical re-positioning in the radiating/receiving systems [18], [19].

As shown in Figure 2.1, based on the relative position of the transmitter and the receiver, radar systems can be broadly classified into two categories:

- Monostatic Radar system: both the transmitter and receiver are at the same location;
- Bistatic Radar system: transmitter and receiver are located at two different positions.
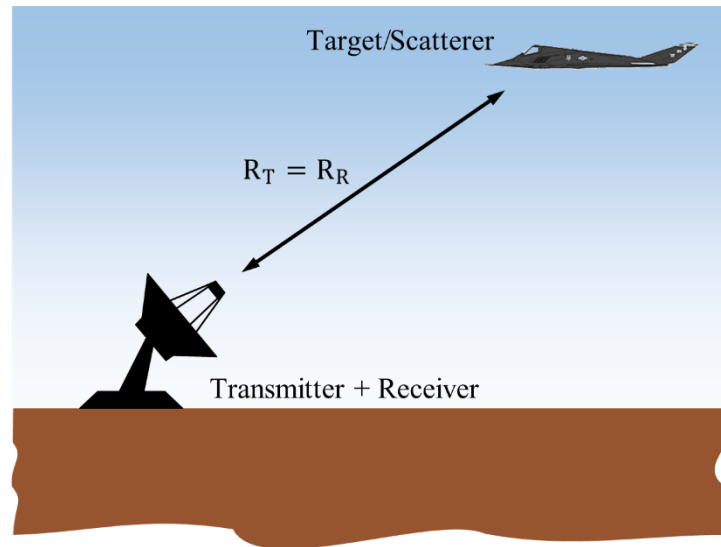
(a)
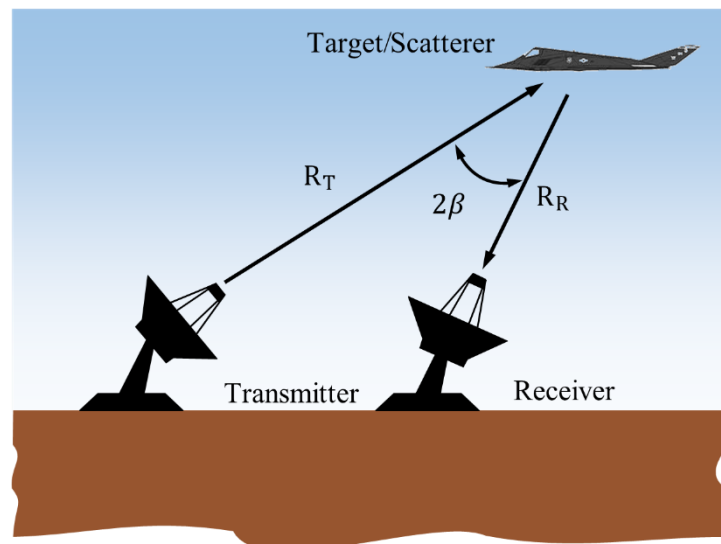
(b)

Figure 2.1: Radar Systems: (a) monostatic, (b) bistatic with bistatic angle of 2β [84]

2.2 Cross-Sections and Their Fundamental Relations

A target can be characterized by several types of cross-sections, which determine the effects of the incident wave on the target in relation to the incident power density. They are important in terms of characterization of the target or scatterer. Further, an understanding of relations between these cross-sections is pivotal in quantifying the scattering or absorption capabilities of the target.

2.2.1 Absorption Cross-Section (σ_a)

Every object has the capability to absorb a part of the incident power and convert it to other forms of energy (i.e., heat or thermal energy). If we consider a receiving antenna as a target/scatterer, a part of the incident power will be absorbed and transmitted to the coupled receiver. The residual of the incident energy primarily gets re-radiated/scattered. Hence, the absorption cross-section σ_a is defined as the power P_a absorbed by the target, normalized to the incident power density S_i [20].

$$\sigma_a(m^2) = \frac{P_a(W)}{S_i(W/m^2)} \tag{2.1}$$

where P_a is the power absorbed by the target and S_i is the incident power density.

2.2.2 Scattering Cross-Section (σ_s)

As mentioned in the previous sub-section, the residual power intercepted by the target primarily gets re-radiated/scattered after the absorption. Similarly to the definition of absorption cross-section, the scattering cross-section is defined as the power removed by the target, using scattering mechanisms, normalized to the incident power density [20].

$$\sigma_s(m^2) = \frac{P_s(W)}{S_i(W/m^2)} \tag{2.2}$$

where P_s is the scattered power scattered and S_i is the incident power density.

Note that the above definition presumes that the scattered energy is isotropically spread over all possible directions, which is not possible in practice [21].

2.2.3 Extinction Cross-Section (σ_e)

The collective incident energy withdrawn by the target through absorption and scattering, normalized to the incident power density, is known as the extinction cross-section (σ_e) [20].

$$\sigma_e(m^2) = \sigma_a + \sigma_s \tag{2.3}$$

where σ_a and σ_s is the absorption cross-section and scattering cross-section, respectively.

2.2.4 Bistatic Cross-Section (σ_b)

As mentioned earlier, the scattered energy has been assumed to be distributed isotropically. This assumption does not hold in practice, which fostered a development of other types of cross-section metrics. In reality, all targets exhibit certain scattering patterns $F(k_r)$, the meaning of which is similar to the radiation pattern of an antenna [18]. Therefore, the energy scattered in any particular direction k_r can be obtained in a way similar to the power radiated in a particular direction, namely, with the help of directivity patterns of an antenna:

$$P_s = D_s(k_r)P_s = D_s(k_r)\sigma_s S_i \tag{2.4}$$

where $D_s(k_r)$ is the directivity of the scattered pattern $F(k_r)$ in the direction k_r. Similarly, the bistatic cross-section (σ_b) along the direction k_r is defined as:

$$\sigma_b(k_r) = D_s(k_r)\sigma_s = D_s(k_r)\frac{P_s}{S_i} = \frac{P_s(k_r)}{S_i} = \lim_{R_r \to \infty} 4\pi R_r^2 \frac{S_s(k_r)}{S_i} \tag{2.5}$$

In addition, in the far-field, the power density of an electromagnetic wave can be sufficiently described using only one of the electric field E or magnetic field H, as in [18]

$$S = \frac{|\text{E}|^2}{2\eta} \tag{2.6}$$

where η is the medium's intrinsic impedance. Substituting (2.6) in (2.5), the bistatic cross-section becomes:

$$\sigma_b(k_r) = \lim_{R_r \to \infty} 4\pi R_r^2 \frac{|\text{E}_s(k_r)|^2}{|\text{E}_i|^2} \tag{2.7}$$

This bistatic cross-section as expressed in (2.6) is commonly referred to as Radar Cross-Section (RCS) [18].

2.3 Radar Equation and Importance of RCS Reduction

Before we proceed further, it is deemed important to derive the radar range equation (RRE). We can derive RRE in its basic form using elementary geometrical principles for both the Bistatic and Monostatic Radar systems. Besides, we will revisit the validity of the definition which we used in (2.5) to define bistatic cross section.

2.3.1 Bistatic Radar System

The power density radiated from the isotropic radiator (e.g., isotropic antenna) at a far-field distance $R_t(S_t{}^{R_t})$ can be derived by dividing the transmitted power (P_t) to the surface area of the sphere over which it has been evenly spread

$$S_t{}^{R_t} = \lim_{R_t \to \infty} \frac{P_t}{4\pi R_t^2} \tag{2.8}$$

When a directional antenna is involved, the power density at a point in space is multiplied by the overall gain of the directional antenna in that particular direction, G_t (θ, ϕ). Consequently, the expression of a generic power density at a distance R_t is written as:

$$S_t^{R_t} = \lim_{R_t \to \infty} \frac{P_t G_t}{4\pi R_t^2} \tag{2.9}$$

As a result, we can obtain the power intercepted and re-radiated by the target positioned at (θ, ϕ, R_t) with respect to the radiator by simply multiplying the RCS of the target (σ_b) by S_t^{Rt}:

$$P_t^{R_t} = \lim_{R_t \to \infty} \frac{\sigma_b P_t G_t}{4\pi R_t^2} \tag{2.10}$$

In a similar manner, the power density received by the receiving antenna (radar) positioned at R_r in the far-field region can be obtained as:

$$S_t^{R_r} = \lim_{\substack{R_r \to \infty \\ R_t \to \infty}} \frac{P_t^{R_t}}{4\pi R_r^2} = \lim_{\substack{R_r \to \infty \\ R_t \to \infty}} \frac{\sigma_b P_t G_t}{(4\pi R_t^2)(4\pi R_r^2)} \tag{2.11}$$

Finally, the power intercepted by the receiving antenna (radar) can be determined by multiplying the effective aperture of the receiving antenna to the received power density. Since the effective aperture of any antenna can be defined as [18]:

$$A_e = \frac{G_r \lambda^2}{4\pi} \tag{2.12}$$

Therefore, the power intercepted by the receiving antenna is given as:

$$P_r^{R_r} = S_r^{R_r} A_e = \lim_{\substack{R_r \to \infty \\ R_t \to \infty}} \frac{G_r \lambda^2}{4\pi} \frac{\sigma_b P_t G_t}{(4\pi R_t^2)(4\pi R_r^2)} \tag{2.13}$$

Consequently, the bistatic cross-section can be written as:

$$\sigma_b = \lim_{\substack{R_r \to \infty \\ R_t \to \infty}} \frac{4\pi S_r^{R_r} A_e (4\pi R_t^2)(4\pi R_r^2)}{G_r \lambda^2 P_t G_t} \tag{2.14}$$

At first, the definitions (2.5) and (2.14) seem to be inconsistent with each other. According to (2.5), the bistatic cross section σ_b is only dependent on R_r, however, (2.14) implies its dependency on both R_t and R_r. To demonstrate that both the definitions (2.5) and (2.14) are equivalent, let us first substitute the definition of effective aperture of (2.13), into (2.14), which leads to

$$\sigma_b = \lim_{\substack{R_r \to \infty \\ R_t \to \infty}} \frac{S_r^{R_r} (4\pi R_t^2)(4\pi R_r^2)}{P_t G_t} \tag{2.15}$$

Furthermore, the expression (2.9) for S_t^{Rt} can be substituted to (2.15), which results in

$$\sigma_b = \lim_{\substack{R_r \to \infty \\ R_t \to \infty}} 4\pi R_r^2 \frac{S_r^{R_r}}{S_t^{R_t}} \tag{2.16}$$

The definition (2.16) is same as derived in (2.5) for the bistatic cross-section. At this point, it becomes clear that the bistatic cross section is not explicitly dependent on R_t; yet it is indirectly dependent on R_t through the definition of S_t^{Rt} as given in (2.9).

2.3.2 Monostatic Radar System

Monostatic Radar system is a special case of Bistatic Radar system where the transmitting and receiving antennas (radars) are positioned at the same place (i.e., $R_t = R_r = R$); therefore, the received power can be simplified into

$$P_r^{R_r} = \frac{G_r \lambda^2}{4\pi} \frac{\sigma_b P_t G_t}{(4\pi R^2)^2} \tag{2.17}$$

Additionally, if the radar system employs the same antenna for both the transmission and reception purposes (i.e., $G_t = G_r = G$), then the received power can further be simplified into:

$$P_r^{R_r} = \frac{\sigma_b P_t G^2 \lambda^2}{(4\pi)^3 R^4} \tag{2.18}$$

It is known that every receiver requires a certain level of minimum power of the received signal ($P_r^{Rr} = P_{min}$) so that it can discriminate the actual signal from the noise and other interfering signals. This is typically characterized by the Signal to Interference-Noise Ratio (SINR). Hence, using (2.18) and the minimum power level P_{min} we can define the maximum radar detection range as:

$$R_{max} = \left[\frac{\sigma_b P_t G^2 \lambda^2}{(4\pi)^3 P_{min}} \right]^{1/4} \tag{2.19}$$

It can be noticed that reduction of RCS of any target by 10 dB (i.e., making it 10 percent of the original value), the maximum detection range of the radar becomes half of the original detection range.

2.3.3 Target Detection by a Radar System

To illustrate the formation of the target's signature and the fundamentals behind the target detection, let us consider a square plate made of a perfect electric conductor (PEC) of the dimension $5\lambda \times 5\lambda$. For illustration purpose, we have considered two angles of incidence: (i) normal incidence (i.e., 0° in Fig. 2.2), and (ii) oblique incidence (i.e., 30° in Fig. 2.3). Figures 2.2 and 2.3 depicts the incident fields, the scattered field, and bistatic RCS patterns. The latter corresponds to the respective scattered field patterns. Note that scattered fields in the forward direction are as strong as the incident fields, and they are 180° out of phase. It is evident from the plots of bistatic RCS patterns (cf. Fig. 2.2(c) and Fig. 2.3(c)) that the bistatic cross-section is substantial in the forward scattering direction. This is the primary explanation why radar systems can detect the target from their signature since it corresponds to the high bistatic cross-section. On the other hand, in order to make the target completely invisible from the radar systems, it is necessary to remove the scattered fields from each and every direction.

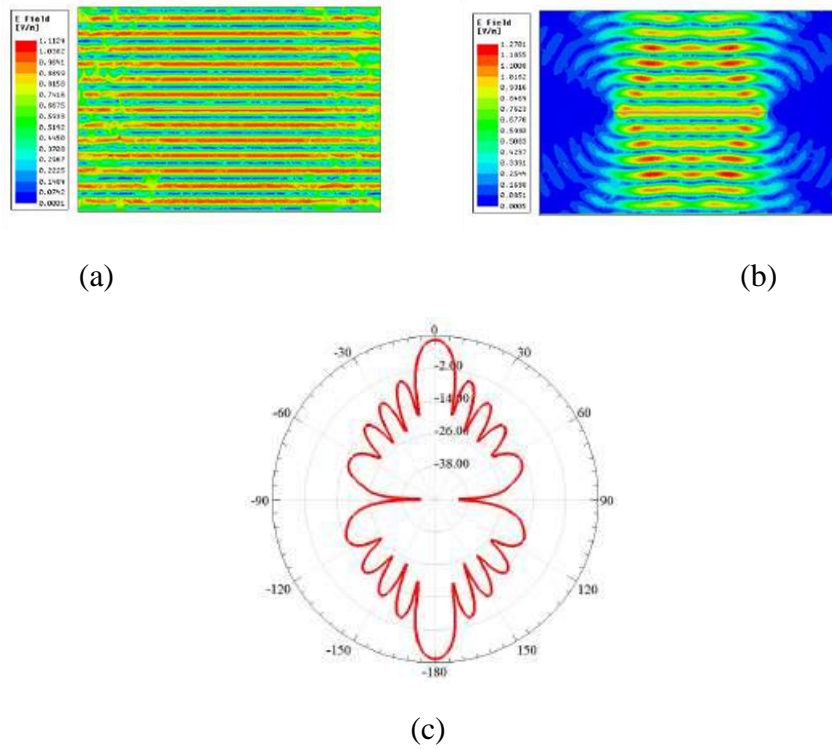This has been recently conceptualized in [22], [23] with the use of metasurfaces and antenna arrays.

(a)   (b)

(c)

Figure 2.2: Square PEC surface of 5λ×5λ under normal incidence: (a) incident fields, (b) scattered fields, and (c) bistatic cross-section [84]

(a)   (b)

(c)
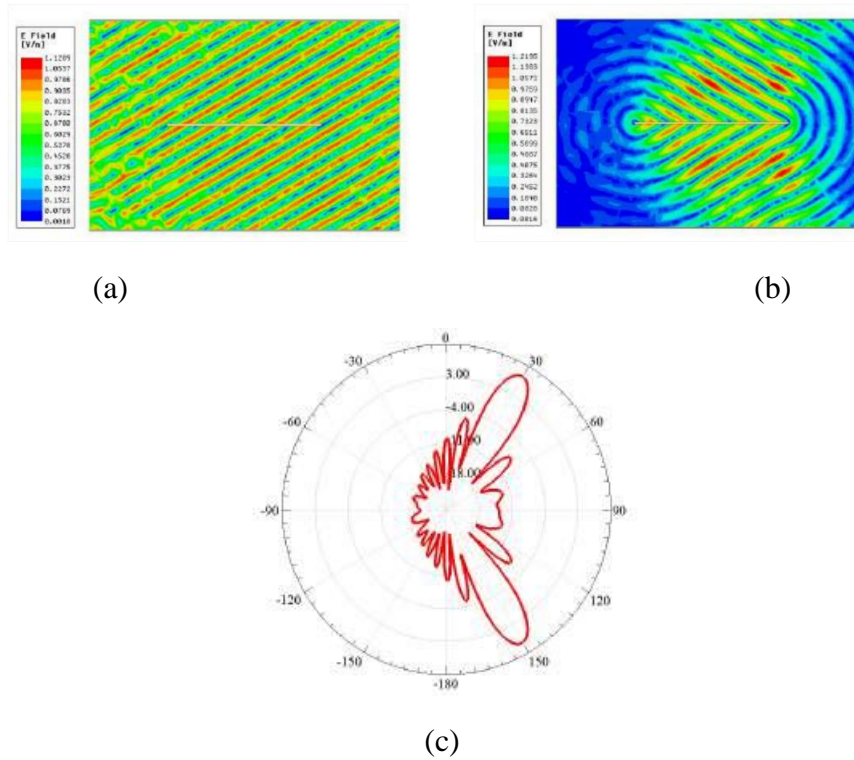
Figure 2.3: Square PEC surface of 5λ ×5λ under oblique incidence: (a) incident fields, (b) scattered fields, and (d) bistatic cross-section [84]

2.4 Fundamentals of Metasurfaces

Since the beginning of the 21st century, advanced manufacturing technologies, such as nano-fabrications, have encouraged scientist and researchers around the globe to think beyond natural materials. They started paying more attention to artificially engineered materials, referred to as metastructures. Typically, these are three-dimensional (3D) structures. Their unique properties are realized by arranging an array of small scatterers or artificial magnetic conductor (AMC) unit cells in a 3D space. The term metamaterial refers to structural characteristics that are more interesting than artificial dielectrics; however, they can still be categorized as bulky materials, in the same way as natural materials. Nevertheless, their extraordinary properties make these metamaterials highly versatile considering their operating frequencies, which can range form the low microwaves to optical. This, in turn, makes them ideal for purposes that include but are not limited to antennas, resonators, dielectrics, switches, EM-shielding, low-reflection materials, perfect lenses, cloaking, and, of course, stealth applications. On the downside, as the AMC unit cells need to be deployed in a 3D space, the practical utility of these metamaterials in real-world applications is questionable. This issues inevitably shifted the effort of exploration—in the first decade of the 21st century—from optimizing a 3D arrangement of the metamaterials to the arrangement of metasurfaces on a two-dimensional (2D) surface. More recently, metasurfaces have been gaining more attention than metamaterials owing to their simplicity and relative ease of fabrication. This is to be expected, given that metasurfaces 2D take up less physical space than their counterparts, 3D metamaterial structures.

2.4.1 Periodic Structures

Periodic structures are arrays of identical elements (typically called unit-cells), arranged along one, two, or three dimensions [24]. A unit-cell is characterized as a building block of a periodic structure, and it repeats itself with inter-element distance called periodicity [24]. An illustration of a 2D planar periodic structure of an arbitrary geometry and periodicity of p_x and p_y has been shown in Fig. 2.3, [24]. In electromagnetic (EM) design, periodic structures are implemented using metallic patches on dielectric slabs, metallic conductors, and dielectric materials. Printing metallic patches on dielectric substrates through these architectures is a popular implementation approach, primarily due to the ease of fabrication. Furthermore, the properties of patch-based periodic architectures are mainly characterized by the patch topology and its geometrical dimensions, where the relative permittivity ε_r, thickness h, and the unit-cell periodicity in x- and y-direction (p_x and p_y, respectively) are the major contributing factors controlling the frequency characteristics [25].
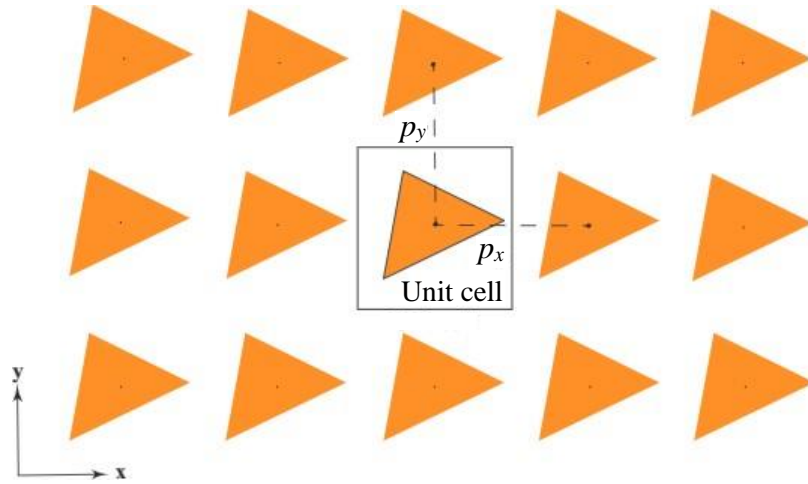
Figure 2.4: Schematic of a two-dimensional periodic structure with periodicity of p_x and p_y in the *x*- and *y*-direction, respectively [24].

To characterize a particular behavior of unit-cell-based periodic structures, several approaches are available, categorized as: (l) multi transmission line models, (2) lumped element model, and (3) full-wave numerical methods [25]. The first two approaches are only limited to simple architectures. They are not very accurate considering the number of approximations involved in the analysis. Full-wave numerical methods are available for a variety of structures, and they have the capacity to evaluate several EM characteristics of periodic architectures with substantially high accuracy. In the past decade, with powerful computing technology and sophisticated numerical techniques, several commercial software packages have surfaced and facilitated researchers and designers to design complex, novel and high-performance periodic structures. The commercial full-wave simulation software applies numerous numerical techniques such as finite-difference time-domain (FDTD), finite element method (FEM), and method of moments (MOM), to solve EM characteristics of the periodic structures [25]. All these methods solve Maxwell's equations under certain boundary conditions to characterize the EM behavior [26].

In this thesis, a commercial full-wave EM simulation software package CST Microwave Studio (mainly its frequency- and time-domain solver) is utilized, primarily based on FDTD and FEM method, to design and characterize unit-cell as well as the developed metasurfaces. The FDTD and FEM methods are among the most widespread numerical techniques for solving the field problems[27], [28].

2.4.2 AMC Unit Cell

Artificial magnetic conductor (AMC)-based unit cells fall under the category of electromagnetic band-gap (EBG) structures. Generally, EBG structures are characterized by a dispersion diagram, surface impedance, and reflection phase [25]. When a plane wave intercepts the EBG structure, an in-phase reflection coefficient analogous to the AMC surface becomes of interest. Therein, the corresponding AMC surface realizes perfect magnetic conditions (PMCs) over a specified frequency bands [25]. The PMC surfaces do not exist in nature; nevertheless, they can be artificially engineered by employing a sequence of metallic

patches on the top of the dielectric medium grounded by the uniform PEC sheet [33]. On the PMC surface, the incident and reflected *E* fields are in phase whereas the *H* fields are out of phase, therefore the total tangential *H* field is zero. Further, the amplitude of reflection coefficient is unity (one), and the corresponding phase is 0° [25], [33]. Since the AMC cells are backed by a uniform PEC sheet, all incident energy is reflected. As a result, the magnitude of the reflection coefficient is one (in lossless environment). In a similar vein, the reflection phase difference between the incident and reflected waves varies as a function of frequency [34]. Other critical parameters that contribute to the overall functionality of AMC unit cells are the incident and polarization angles. To date, various AMC topologies have been explored to improve functional bandwidth, oblique incidence and polarization independency [35]-[37]. In this thesis, we introduced novel AMC-based unit cell geometries to enhance their functional bandwidth, and incident angle stability.

2.4.3 Literature Review

Back in 1947, George Sinclair, the founder of the ElectroScience Laboratory (ESL) at Ohio State University, United States, proposed that an antenna was considered a target with strong scattering ability. Subsequently, many scholars began to discuss and study the scattering mechanism, and RCS control methods of the antenna. In 1949, D.D. King discussed the importance of the surface current distribution within the antenna to the RCS and backscattering, and drew the effect of the antenna load impedance on the scattering amplitude and the scattering pattern of the antenna [38]. In 1952, the backscatter characteristics of a cylindrical antenna in the case of short circuit and the matched load were studied [39]. The expression for the scattering field based on the conjugate matching conditions for the antennas was considered in [40], which fostered research on the antenna scattering technology. Afterwards, many theoretical considerations have been carried out during the 1990s. Low RCS of antennas can be obtained by changing the propagation direction of the target scattering peak away from the direction of the radar receiver. Ultimately, the radar receivers would not be able to pick the scattered signals, and the antenna surface would become of low observability to the radars. The radar signals could also be absorbed by the antenna surface. Consequently, four main techniques have been extensively studied in the literature in the context of the reduction of the target RCS, including radar absorbing materials (RAMs), reshaping of the target surface, using active cancellation, and passive cancellation methods [41]. RAMs use the absorption mechanism to reduce the reflected energy from the target surface. This absorption mechanism is mainly due to the several types of losses associated with the dielectric or magnetic properties of the material [42].

Based on the loss mechanisms, the radar absorbing materials can convert the incident electromagnetic energy into another form of energy. This results in minimizing the scattering from the surface, leading to low RCS. In [43], [44], the RCS reduction of different surfaces was implemented using RAMs, but it was concluded that the absorbing behavior of the surface is restricted to a narrow bandwidth.
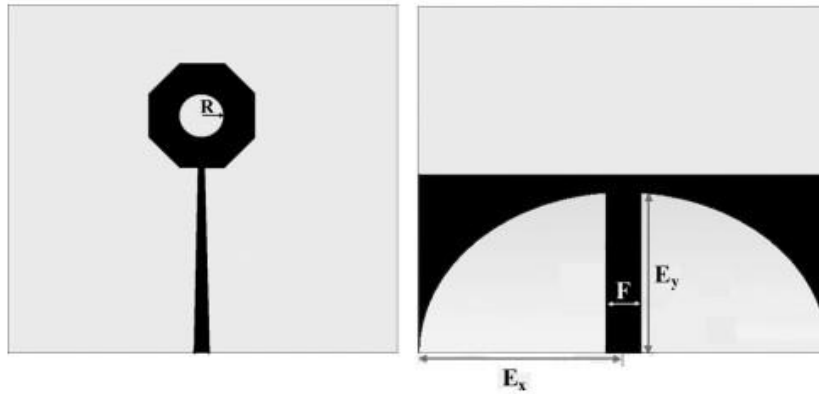
Figure 2.5: Top and bottom view of the modified antenna for RCS reduction [45].

The antenna surface can be reshaped to realize low scattering performance. Antenna reshaping techniques are often based on the analysis of the current distribution on the surface of the metallic patch during the radiating state of the antenna. The region that contributes less to the antenna radiation can be observed, and then the structure of antenna surface can be reshaped accordingly to reduce the RCS without affecting the antenna radiation performance. In [45], the RCS reduction of the UWB planar octogonal antenna was achieved by the geometrical shaping method. The structure of the modified UWB planar octagonal antenna can be seen in Fig. 2.5. With the employment of the reshaping technique, the surface of the target was modified to redirect the incoming electromagnetic energy (EM) away from the surface. The drawbacks of the reshaping approach include possible effects of reshaping on the radiation performance of the antenna, and the narrowband nature of the RCS reduction.

Without using wideband absorbers and reshaping the surface, the incident waves from the radars can be redirected to other directions by using negative-indexed materials. Over the past decade, the manipulation of EM waves has received tremendous interests, underpinned by the advent of the transformation method [46], [47], and metamaterials [48]. A wide variety of novel devices, such as invisibility cloaks and advanced lenses, have been realized in electromagnetics and other fields. Metamaterials are subwavelength artificial composites, based on periodic or non-periodic unit cells, that pave the way for unusual properties that are unavailable in nature.

As a new class of metamaterials, metasurfaces have been extensively utilized to generate the abrupt interfacial phase changes, for manipulating waves propagation, to analyze the reflective and transmissive properties, and to provide the unique way to redirect the incoming electromagnetic (EM) waves into various directions [49]-[53].

The unusual physical properties of metamaterials such as negative refraction can be utilized to realize low RCS. Many researchers have applied metasurfaces to reduce RCS of different surfaces. In [49], a combination of the perfect electric conductor (PEC) and artificial magnetic conductor (AMC) was employed in a periodic arrangement, chessboard configuration, to reduce the scattering of the surface as depicted in Fig. 2.6. Due to the 180° phase difference between the reflection of AMC and PEC, the waves reflected from AMC and PEC cancel each other when the incident electromagnetic wave is perpendicular to the
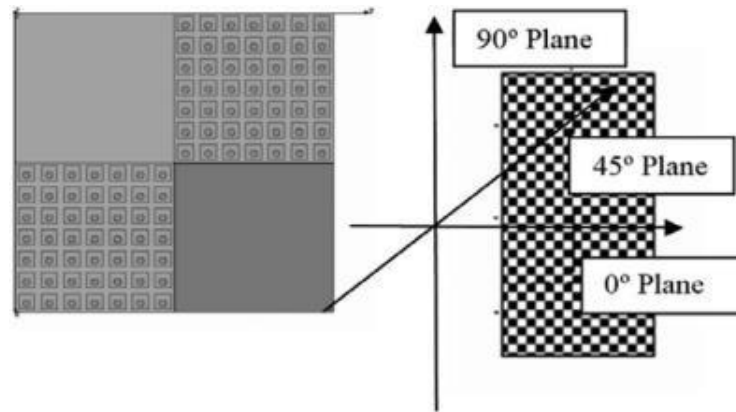
Figure 2.6: Arrangement of AMC and PEC structure in chessboard configuration [49].

surface. The chessboard structure scatters the electromagnetic energy into four main lobes at (φ=45°, 135°, 225°, and 315°), therefore, the backward RCS decreases significantly. However, due to the narrow band of out of phase reflection between AMC and PEC, the bandwidth of the RCS reduction was very narrow as well. In particular, the 10 dB RCS reduction was achieved over the relative bandwidth of only five percent.

To overcome the issue of the narrow-bandwidth RCS reduction, the combinations of AMCs with different configuration [50], [51] or different sizes [52], [53] were proposed to fulfill the phase cancellation criteria. The idea is to utilize the out-of-phase reflection of the unit cells to achieve the effective cancellation over a wider frequency band. Furthermore, these unit cells were arranged in a chessboard-like configuration to scatter the reflected energy into four diagonal directions with low level of scattered energy in the normal direction. In [50], 10 dB RCS reduction of the polarization-dependent surface was achieved over a relative bandwidth of 32%. The low scattering surface is subsequently integrated with the antenna for realized gain enhancement. In [51], the RCS reduction of the microstrip antenna was attained using the combination of two differently sized AMCs, arranged in a chessboard configuration, with the maximum RCS reduction of 31.9 dB. The design of AMCs based on Jerusalem crosses with different sizes was used in [52] to achieve 10 dB RCS reduction of the surface over a relative bandwidth of forty percent. In [53], low RCS of the circularly polarized (CP) array antenna was proposed by using tightly-coupled anisotropic element in a chessboard configuration. The in-band and out-of-band RCS reduction of the array antenna was also achieved.

Many researchers also implemented the electronic band gap (EBG) and frequency selective surfaces (FSS) to realize the RCS reduction of antennas. Every method has its advantages and disadvantages. For practical applications, we need to select appropriate methods to reduce the RCS of the antenna, according to the various performance requirements. Usually, RCS reduction in broad frequency range is highly desirable for stealth applications.

The RCS reduction from 3 GHz to 10 GHz bandwidth was achieved by using the combinations of FSS and microstrip resonators in [54]. Therein, the radiation performance of the microstrip antenna was less affected by the inclusion of the resonators. In [55], using the EBG structures, hexagonal and square shaped checkerboard surface was designed to reduce the RCS of the surface over the relative bandwidth of 60%.
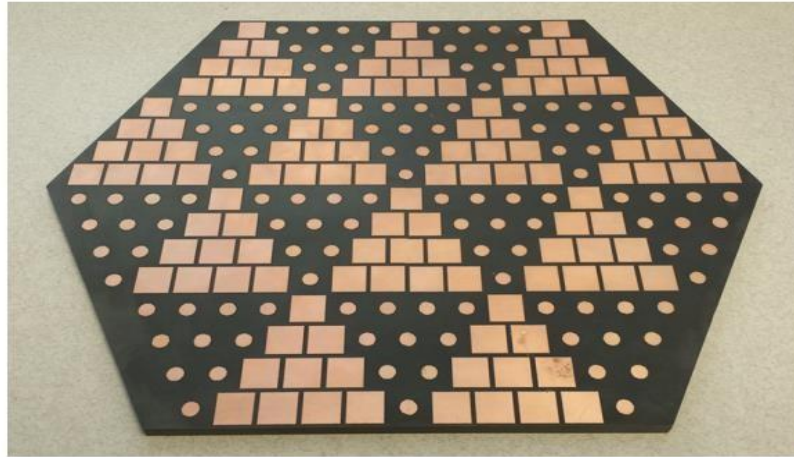
Figure 2.7: The structure of hexagonal shaped chessboard surface [55].

The hexagonal-shaped checkerboard surface can be seen in Fig. 2.7. It has also been expounded that the hexagonal shaped checkerboard surface redirects the incoming EM energy into six main lobes and it reduces RCS to a higher extent as the square-shaped chessboard surface.

In addition to the above methods, polarization conversion metasurfaces (PCM) were applied to reduce the RCS of the antennas. In [56], a technique for reducing the RCS of the antenna was implemented based on a fishbone-like element. The PCM was generated by the chessboard arrangement of the fishbone-like element and its mirror image, which greatly widened the RCS reduction bandwidth of the slot array antenna. The RCS reduction of Fabry-Perot (F-P) cavity antenna was reduced by using the combination of PCM and partially reflecting surface (PRS) in [57]. The antenna gain was increased by 7 dB, and its RCS reduction was achieved in the range of 9-20 GHz by using the phase cancellation principle. The average RCS reduction of 12.4 dB was obtained over the designed frequency band. In [58], the holographic surface was used to reduce the RCS of the antenna. The holographic surface is formed by using the four differently sized square shaped metallic sheets, which help to change the surface impedance periodically. After the holographic surface was designed, it was further loaded to the slot antenna array to achieve the RCS reduction. The principle thereof was associated with the working band of the holographic surface, over which the incident waves from the radar can be transformed into the surface wave. Therefore, the backscattered energy from the surface of the slot antenna array can be minimized.

To further reduce the RCS of the surfaces, an approach based on the coding metasurfaces was proposed in [58]. The RCS reduction was achieved by controlling and adjusting the phases of different coding elements named "0" and "1". The coding sequences of the metasurfaces can be optimized to further improve the RCS reduction properties. Nowadays, the research on the RCS reduction of the antenna is considered a hot topic due to its importance in practical applications. Many researchers are currently working on the associated problems that include the following questions: (i) how to keep the antenna radiation characteristics unaffected while reducing the RCS; (ii) how to reduce the RCS over the broad frequency range; (iii) how to reduce the in-band and out-of-band RCS. Therefore, it is important to explore such widely defined areas to further improve the performance of the stealth systems.

2.4.4 Existing Design Methodologies

The development of AMC unit-cell-based periodic structures (i.e., metasurfaces) involves handling of individual unit cell designs, as well as concurrent adjustment of their design variables. Thus far, numerous metasurface structures have been presented to achieve wideband RCS reduction [47]-[58]. Therewithal, the lack of reliable theoretical models compels conventional design methodologies to mostly rely on empirical reasoning, physical intuition, or trial and error. Additionally, a substantial involvement of human interaction makes such approaches laborious and ineffective. Further, they are time consuming due to the involvement of full-wave EM simulations to characterize the performance of AMC structures. Altogether, the aforementioned downsides pose serious concerns pertaining to the efficiency of experience-driven design practices, as well as their capability of finding truly (presumably global) optimum solutions. Considering the practical design measures, the problem is additionally exacerbated by highly non-linear input-output relationships between the design variables and the system responses. An additional obstacle limiting efficacious design of metasurfaces is implicit processing of RCS reduction characteristics. To accomplish essential RCS reduction, the design task is typically formulated in terms of phase reflection characteristics of the AMC unit cells. More precisely, it has been discussed in the literature that 10 dB RCS reduction can be provided over a frequency band if the phase difference between the two meta-atoms remains within the $180° \pm 37°$ range [54], [58]. On the contrary, their reflection amplitudes—although contributing to the overall performance of the AMC structure—are principally ignored. To handle this, a novel formulation of the metasurface design task with explicit handling of RCS reduction at the level of AMC unit cells is required. Altogether, the aforesaid challenges call for a new algorithmic solution that enable efficient development of high-performance metasurfaces going beyond interactive approaches, and permits design automation, reliability, and computational efficiency. Over the last decade, extraordinary advancements in computing hardware and software drastically boosted the popularity and extensive use of rigorous EM-driven design methodologies, principally based on numerical optimization [63]. Nevertheless, direct EM-based optimization of metasurface architectures may be prohibitively expensive when using traditional optimization algorithms, especially when global exploration is needed. A practical workaround is a utilization of machine learning techniques [59]-[62], [64], [65], together with surrogate-based modeling methods [63], [66]. By doing so, the computational burden can indeed be shifted to a cheaper representation of the structure at hand, thus expediting the design process. In the related vein, incorporation of other means such as problem decomposition [66], may also aid the parameter tuning process and facilitate global exploration, otherwise infeasible when operating directly on EM simulation models.

2.5 Design Optimization

This section presents a brief overview of numerical optimization that falls within the scope of the thesis. A short summary of standard optimization techniques, including gradient-based methods and population-based metaheuristics, as well as surrogate-based modelling techniques is a part of the discussion.

The metasurface optimization problem is formulated as the following nonlinear minimization task [67]:

$$\boldsymbol{x}^* = \arg\min_{\boldsymbol{x}} U(\boldsymbol{R}_f(\boldsymbol{x})) \tag{2.20}$$

Here, $\boldsymbol{R}_f \in R^m$ represents the EM simulation response vector of the metasurface performance characteristics of interest, e.g., the RCS reduction characteristics $|R_{red}|$ evaluated at m different frequencies; $\boldsymbol{x} \in R^n$ is a vector of metasurface designable variables to be adjusted, and U is a given scalar merit function encoding the design specifications, e.g., a minimax function with upper and lower specifications. The vector $\boldsymbol{x}^*$ is the optimal design to be determined. The composition $U(\boldsymbol{R}_f(\boldsymbol{x}))$ represents an objective function. As per definition (2.20), the objective function should be defined so that better designs correspond to the smaller values of U.

Figure 2.8 illustrates a particular example of design specifications for the RCS reduction characteristics. In this case, the objective function $U(\boldsymbol{R}_f(\boldsymbol{x}))$ is defined as the continuous frequency range for which the condition $|R_{red}| \geq 10$ dB holds. In other words, it is the RCS reduction bandwidth.

For the rest of the section, the composition $U(\boldsymbol{R}_f(\boldsymbol{x}))$ will be denoted using an abbreviated symbol of $f(\boldsymbol{x})$. In certain cases, the problem (2.20) is a constrained one. Three different sets of constraints can be considered:

- Lower and upper bounds for a vector of designable variables, i.e., $l_b \leq x_b \leq u_b$, $b = 1, \ldots, m$;

- Equality constraints, i.e., $c_{eq.l}(\boldsymbol{x}) = 0$, $l = 1, \ldots, M_{eq}$, where M_{eq} is the number of constraints;

- Inequality constraints, i.e., $c_{ineq.l}(\boldsymbol{x}) \leq 0$, $l = 1, \ldots, M_{ineq}$, where M_{ineq} is the number of in equality constraints.

Typically, design constraints are introduced to ensure that the device or the system (e.g., metasurface architecture) to be evaluated by the simulation software is physically valid (e.g., so that the unit cells and other elements of the architecture do not overlap, etc.). Further, the constraints can be implemented to make sure that the physical dimensions (length, width, and area) or selected characteristics of the structure is within the assumed values.

Figure 2.9 presents a typical flow of simulation-driven design optimization, here, gradient-based search. Typically, it is an iterative process where the solutions determined by the optimizer are validated by evaluating the structure at hand using the EM solver. Moreover, the search process is guided either by the model response itself or by the response gradients. In the subsequent sections, we briefly discuss gradient-based optimization techniques as well as population-based metaheuristics.
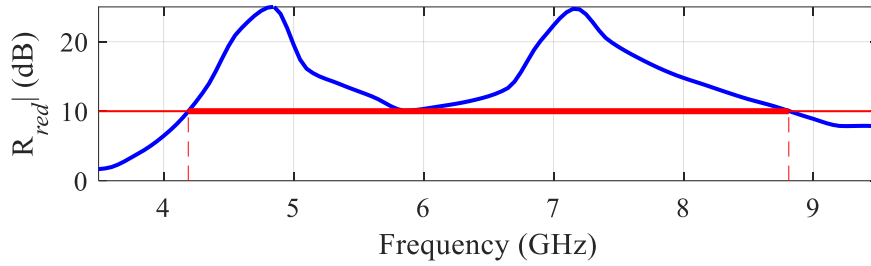
Figure 2.8: Exemplary design specifications for metasurface optimization. The objective function $U(\boldsymbol{R}_f(\boldsymbol{x}))$ is defined as the continuous frequency range for which the condition $|R_{red}| \geq 10$ dB holds. In other words, it corresponds to the RCS reduction bandwidth.
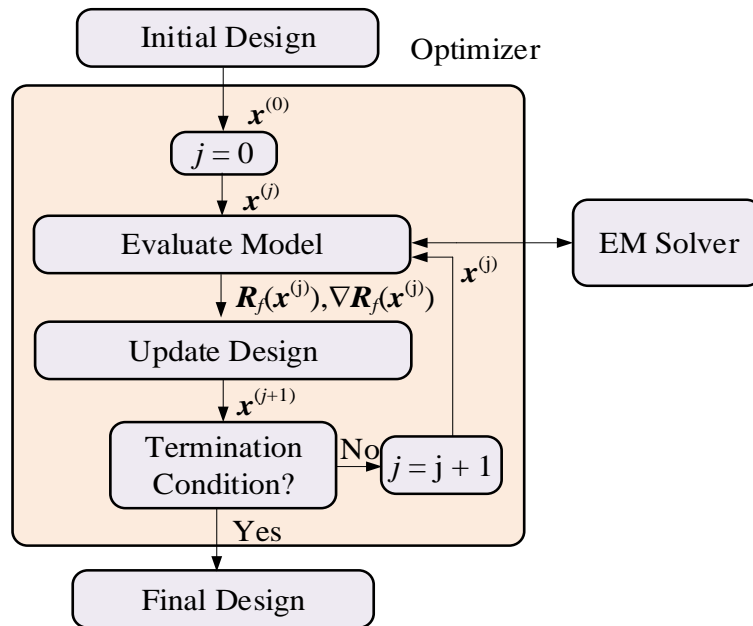

Figure 2.9: A flowchart of gradient-based simulation-driven optimization. The search process can be guided by the model response or by the response and its derivatives [66].

2.5.1 Gradient-based Optimization Methods

Gradient-based techniques are amongst the most widely utilized class of optimization methods [67]. Therein, the exploration is dependent upon the derivatives of the objective function. Assuming that the merit function $f(\boldsymbol{x})$ is sufficiently smooth (at least continuously differentiable), the gradient $\nabla f = [\partial f/\partial x_1 \; \partial f/\partial x_2 \; \ldots \; \partial f/\partial x_n]^T$ delivers the information about the descent of f in the vicinity of the design at hand. Particularly,

$$f(\boldsymbol{x}+h) \cong f(\boldsymbol{x}) + \nabla f(\boldsymbol{x})\boldsymbol{h} < f(\boldsymbol{x}) \tag{2.21}$$

if $\boldsymbol{h}$ is a descent direction, i.e., $\nabla f(\boldsymbol{x})\cdot\boldsymbol{h} < 0$. Specifically, $\boldsymbol{h} = -\nabla f(\boldsymbol{x})$ is the steepest descent direction. Though it is beneficial to follow this direction while away from the optimum, steepest descent techniques manifest poor overall performance and are not commonly used in practice [68]. A more practical approach is a conjugate-gradient method, where the search direction $\boldsymbol{h}$ is determined by the previous direction $\boldsymbol{h}_{i-1}$ and the current gradient. We have

$$h = -\nabla f(x^{(i)}) + \gamma h_{i-1} \tag{2.22}$$

One of the widely utilized approaches for selecting the coefficient γ is the Fleecher-Reeves method where

$$\gamma = \frac{\nabla f(x)^T \nabla f(x)}{\nabla f(x^{(i-1)})^T \nabla f(x^{(i-1)})} \tag{2.23}$$

The subsequent design $x^{(i+1)}$ is computed from the existing one $x^{(i)}$ as:

$$x^{(i+1)} = x^{(i)} + \alpha h \tag{2.24}$$

The selection of the step size $\alpha > 0$ relies on the line search or obtaining information from the second-order derivatives [69].

The Newton and quasi-Newton methods belong to another class of optimization techniques. If f is at least twice continuously differentiable, a second-order Taylor expansion of f can be defined as:

$$f(x+h) \cong f(x) + \nabla f(x)h + \frac{1}{2}hH(x)h \tag{2.25}$$

where, $H(x)$ is the Hessian of f at x, i.e., $H(x) = [\partial^2 f/\partial x_j \partial x_k]_{j,k=1,\dots,n}$. It entails that the next approximation of the optimal solution can be computed as:

$$x^{(i+1)} = x^{(i)} + [H(x)]^{-1}\nabla f(x) \tag{2.26}$$

The algorithm (2.26) delivers extraordinarily fast (quadratic) convergence rate; however, it is only applicable if the initial point is sufficiently close to the optimal solution and the Hessian is positive definite at all iterations [68]. Altogether, the aforesaid conditions are hardly ever satisfied, hence, the algorithm (2.26) is impractical. As an alternative, a variety of damped Newton techniques have been adopted [69].

Trust-region (TR) algorithms [70] also belong to gradient-based optimization approaches. The TR method iteratively approaches a local minimum of the objective function f by generating a series of approximations $x^{(i)}$, $i = 0, 1, \dots$, to the optimum design x^*. These are typically determined by optimizing the linear expansion model

$$L^{(i)}(x) = f(x^{(i)}) + \nabla f(x^{(i)}).(x - x^{(i)}) \tag{2.27}$$

In the ith iteration of the TR algorithm, the following optimization task is solved

$$x^{i+1} = \arg \min_{x;-d^{(i)} \le x-x^{(i)} \le d^{(i)}} U(L^{(i)}(x)) \tag{2.28}$$

The vector $d^{(i)}$ is the TR region size decided using the standard guidelines [70], i.e., based on the gain ratio $\rho = [U(R(x^{(i+1)})) - U(R(x^{(i)}))]/[U(L^{(i)}(x^{(i+1)})) - U(L^{(i)}(x^{(i)}))]$ (actual versus linear-model-predicted objective function improvement). The inequalities $-d^{(i)} \le x - x^{(i)} \le d^{(i)}$ in (2.28) are understood component-wise. Due to the fact that the designable variable ranges in metasurface architectures may be drastically different for various parameters (e.g., fractions of millimetre for gaps and tens of millimetres for ground plane width, etc.), the search region is characterized here as a hypercube rather than a ball $\|x - x^{(i)}\| \le \delta^{(i)}$ (Euclidean norm with

scalar TR radius). This—while deciding the initial size vector $\boldsymbol{d}^{(0)}$ proportional to the design space sizes—enables similar treatment of variables with dramatically different ranges. The TR algorithm is the major local optimization approach utilized in this thesis.

In the framework of EM-driven design optimization, utility of gradient-based method is limited, when applied directly on full-wave models. They are relatively expensive due to the need of evaluating the system response gradients through finite differentiation, as well as because of the high EM simulation cost of complex structures. In some instances, it is possible to expedite the procedure by exploiting adjoint sensitivities but these are only accessible—among commercial solvers—through CST [71] and HFSS [72], and only for a limited number of practical cases.

2.5.2 Metaheuristics and Global Optimization

Metaheuristics are derivative-free methods that exhibit features beneficial from the perspective of handling various practical optimization problems: (1) global exploration capability; (2) capacity to handle non-differentiable, discontinuous, or noisy cost functions; and (3) capability to handle multimodal (i.e., those featuring multiple local optima) and multi-objective problems. Metaheuristics are developed based on the observation of natural processes such as biological or social systems. They have the capability to avoid getting stuck in local optima and converge towards a globally optimal solution of the problem at hand. Some of the popular methods of this class include genetic algorithms (GAs) [73], evolutionary algorithms (EAs) [74], evolution strategies (ES) [74], particle swarm optimizers (PSO) [75], differential evolution (DE) [76], and firefly algorithm [68].

A typical flow of a population-based metaheuristic algorithm, pertinent to methods such as GAs or EAs, is the following [67]:

1. Initialize the population P (a random process);
2. Evaluate individuals in the population P;
3. Choose parent individuals S from P;
4. Apply recombination operators to create a new population P from parent individuals S;
5. Apply mutation operators to introduce local perturbations in individuals of P;
6. If the termination condition is not satisfied go to 2;
7. END.

Population-based metaheuristics are suitable methods whenever the evaluation time of the objective function is low, or the computational budget is of concern. These technique are preferred for solving multimodal tasks. In the realm of antenna design, their primary application are antenna array optimization problems, specifically pattern synthesis [77], [78], as long as the array is evaluated using the analytical array factor model. At the same time, due to their high computational complexity, population-based metaheuristics are not recommended for direct handling of full-wave electromagnetic simulation models.

2.5.3 Surrogate Modelling/Machine Learning

Traditional numerical optimization techniques are—in their majority—robust methods, yet their utility for handling contemporary design challenges in high-frequency engineering is limited primarily due to the high computational cost of EM simulations. Recently, one of the promising ways to address these issues, in particular, to perform parametric optimization of expensive simulation models in a decent timeframe, has been surrogate-based optimization [79].

The fundamental idea behind surrogate-based optimization is to replace direct handling of the expensive computational model by an iterative process, in which a sequence of intermediate designs approaching the solution to the original optimization problem is generated by means of optimizing a fast yet reasonably accurate representation of the high fidelity model, referred to as a surrogate [79]. Therein, data-driven surrogates represent the major and arguably the most popular class of surrogates. Their popularity stems from the following appealing features:

- Data-driven models can be constructed without a prior knowledge about the physical system at hand;
- They are generally based on algebraic models;
- They are universal and, therefore, easily transferrable between various problem domains;
- They are cheap to evaluate.

At the same time, data-driven models usually require substantial amounts of training data to ensure the accuracy. Further, the number of training samples grows rapidly with the dimensionality of the parameter space (so-called curse of dimensionality) [79]. This is a serious limiting factor, especially when the model is to be constructed over broad ranges of the system parameters, and the system outputs are highly nonlinear.
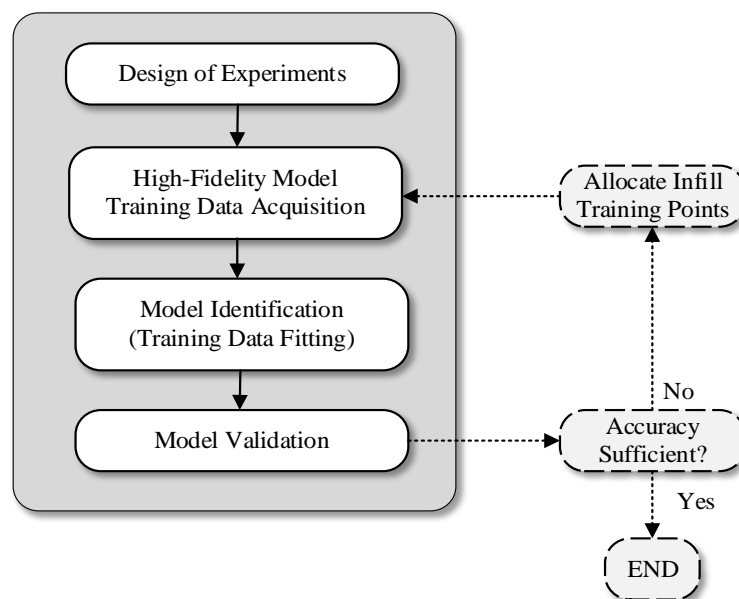

Figure 2.10: A generic procedure of constructing data-driven surrogate models [79].

A generic flowchart of the data-driven surrogate modeling process is shown in Fig. 2.10.

One of the most popular modeling methods of this class, utilized in this work, is kriging. Kriging is a method for interpolating deterministic noise-free data [80]. It is a Gaussian process-based modeling technique, extensively used for building interpolating surrogates in a wide range of applications [80], [81]. For the convenience of the reader, a brief summary of the method is provided below assuming the scalar output of the system at hand. Generalization for vector-valued functions is straightforward. In its fundamental formulation, kriging assumes that the function, denoted as $f(\boldsymbol{x})$, is of the form

$$f(\boldsymbol{x}) = \boldsymbol{g}(\boldsymbol{x})^T \boldsymbol{\beta} + Z(\boldsymbol{x}) \tag{2.29}$$

where $\boldsymbol{g}(\boldsymbol{x}) = [g_1(\boldsymbol{x})\ g_2(\boldsymbol{x})\ \dots\ g_N(\boldsymbol{x})]^T$ are known (e.g., constant) system responses, $\boldsymbol{\beta} = [\beta_1\ \beta_2\ \dots\ \beta_N]^T$ are the unknown hyperparameters, and $Z(\boldsymbol{x})$ is a realization of a normally distributed Gaussian random process with zero mean and variance σ^2. The regression term $\boldsymbol{g}(\boldsymbol{x})^T \boldsymbol{\beta}$ serves as a trend function for f, whereas $Z(\boldsymbol{x})$ handles localized variations. The covariance matrix of $Z(\boldsymbol{x})$ is given as

$$Cov[Z(\boldsymbol{x}^{(i)})Z(\boldsymbol{x}^{(j)})] = \sigma^2 \boldsymbol{R}([R(\boldsymbol{x}^{(i)}, \boldsymbol{x}^{(j)})]) \tag{2.30}$$

where $\boldsymbol{R}$ is a $p \times p$ correlation matrix with $R_{ij} = R(\boldsymbol{x}^{(i)}, \boldsymbol{x}^{(j)})$, and $R(\boldsymbol{x}^{(i)}, \boldsymbol{x}^{(j)})$ is the correlation function between data samples $\boldsymbol{x}^{(i)}$ and $\boldsymbol{x}^{(j)}$. One of the most popular choice is the Gaussian correlation function

$$R(\boldsymbol{x}, \boldsymbol{y}) = \exp\left[-\sum_{k=1}^{n} \theta_k \, | x_k - y_k |^2 \right] \tag{2.31}$$

where θ_k are the unknown correlation parameters, and x_k and y_k are the kth components of the vectors $\boldsymbol{x}$ and $\boldsymbol{y}$, respectively. The kriging predictor is defined as [80]

$$s(\boldsymbol{x}) = \boldsymbol{g}(\boldsymbol{x})^T \boldsymbol{\beta} + \boldsymbol{r}^T(\boldsymbol{x}) \boldsymbol{R}^{-1}(\boldsymbol{h} - \boldsymbol{G}\boldsymbol{\beta}) \tag{2.32}$$

where $\boldsymbol{r}(\boldsymbol{x}) = [R(\boldsymbol{x}, \boldsymbol{x}^{(1)})\ \dots\ R(\boldsymbol{x}, \boldsymbol{x}^{(p)})]^T$, $\boldsymbol{f} = [f(\boldsymbol{x}^{(1)})\ f(\boldsymbol{x}^{(2)})\ \dots\ f(\boldsymbol{x}^{(p)})]^T$, and $\boldsymbol{G}$ is a $p \times N$ matrix with $G_{ij} = P_j(\boldsymbol{x}^{(i)})$. The vector of model parameters $\boldsymbol{\beta}$ can be determined as

$$\boldsymbol{\beta} = (\boldsymbol{G}^T \boldsymbol{R}^{-1} \boldsymbol{G})^{-1} \boldsymbol{G}^T \boldsymbol{R}^{-1} \boldsymbol{f} \tag{2.33}$$

Towards the end, model fitting is realized by maximum likelihood scheme for θ_k

$$-[p \ln(\sigma^2) + \ln | \boldsymbol{R} |] / 2 \tag{2.34}$$

Here, both σ^2 and $\boldsymbol{R}$ are functions of θ_k.

2.6   Optimization Methods Utilized in this Work

The problem considered in this work is to find optimal AMC unit-cell designs as well as corresponding metasurface architecture featuring RCS reduction in a broad frequency range. The design task is principally handled through two independent stages of the optimization process. The initial stage involves global surrogate-assisted optimization of the AMC-based unit cells, followed by their local refinement. The final stage is the direct EM-driven maximization of the RCS reduction bandwidth at the level of the entire metasurface, enabled by problem specific formulation of the objective function involving regularization terms. Below, we give a brief overview of the developed approaches, the details can be found in the remaining chapters of this thesis.

The aim of the initial optimization stage, i.e., machine-learning-based approach, is to find a pair of unit cell designs featuring the phase difference within the range of $180° \pm \alpha_{max}$ over a possibly broad frequency range F. In order to achieve that, the surrogate model representing the unit cell phase characteristics is constructed using kriging interpolation [80]. The surrogate is identified using the training data samples $\{x^{(k)}, R(x^{(k)})\}_{k=1,...,N}$, where $x^{(k)}$ and $R(x)$ represent the vector of designable variables and their corresponding EM-simulated response, whereas N denotes the total number of samples. Rectangular grid-based design of experiments strategy is employed to sample the training data, which is a suitable arrangement for the cases where the parameter space is low-dimensional. Having cheap surrogate at hand, global optimization is performed in an exhaustive manner, based on a structured grid. In plain words, the optimal cell designs are determined by exploring all possible combinations of unit cell geometries, and finding the one that minimizes the objective function (here, maximizing the frequency range for which the phase difference between the two cells remains within $180° \pm \alpha_{max}$). After identifying the optimal pair of cells, the local refinement is executed using gradient-based search[82].

In the final optimization stage, i.e., to extend RCS reduction bandwidth at the level of the entire metasurface, we utilize a trust-region (TR) [70] gradient search algorithm (cf. (2.27), (2.28)). Therein, the construction of the Taylor expansion model requires the knowledge of the Jacobian matrix, which is estimated using finite differentiation in the first iteration, then updated by the adaptive application of the rank-one Broyden formula [82]. Additionally, a regularization approach is also implemented to efficiently manage frequency-localized violations of the RCS reduction threshold that occur while extending the overall reduction bandwidth. The overall procedure is fast due to the availability of a good initial design obtained at the initial optimization stage.

In some cases, a binary coded genetic algorithm [77] is used at the last stage of the metasurface design process in order to find the optimal composition of the unit-cells by globally optimizing array factor-based approximation model [58], [83].

Chapter 3

3   Paper # 1

Muhammad Abdullah and Slawomir Koziel

Surrogate-Assisted Design of Checkerboard Metasurface for Broadband Radar Cross-Section Reduction

Surrogate-Assisted Design of Checkerboard Metasurface for Broadband Radar Cross-Section Reduction

MUHAMMAD ABDULLAH[ID][1] **AND SLAWOMIR KOZIEL**[ID][1,2], **(Senior Member, IEEE)**

[1]Engineering Optimization and Modeling Center, Reykjavik University, 101 Reykjavik, Iceland
[2]Faculty of Electronics, Telecommunications and Informatics, Gdańsk University of Technology, 80-233 Gdańsk, Poland

Corresponding author: Slawomir Koziel (koziel@ru.is)

ABSTRACT Metasurfaces have been extensively exploited in stealth applications to reduce radar cross section (RCS). They rely on the manipulation of backward scattering of electromagnetic (EM) waves into various oblique angles. However, arbitrary control of the scattering properties poses a significant challenge as a design task. Yet it is a principal requirement for making RCS reduction possible. This article introduces a surrogate-based approach for rapid design optimization of checkerboard metasurfaces. Our methodology involves fast metamodels, and a combination of surrogate-assisted global optimization with local, gradient-based tuning. It permits an efficient control of the EM wave reflection characteristics, and ensures arriving at that the globally optimum solution within the assumed parameter space. The design procedure is fully automated. The framework is employed to develop a novel broadband checkerboard metasurface, where the RCS reduction is fundamentally based on the backward scattering manipulation carefully controlled by simultaneous adjustment of the unit cell dimensions. The properties of the structure are demonstrated using simulated monostatic and bistatic RCSs. The proposed metasurface exhibits 6 dB RCS reduction within the frequency range from 16 to 37 GHz. The numerical results are validated using physical measurements of the fabricated prototype. Experimental data indicates that the relative RCS reduction bandwidth is 83 percent, which makes the proposed structure outperforming the designs reported in the literature.

INDEX TERMS Metasurfaces, surrogate modeling, scattering manipulation, checkerboard configuration, radar cross-section (RCS), broadband.

I. INTRODUCTION

The advancements in the field of metamaterial technology have opened the new paths to numerous applications, such as invisibility cloaks, gradient index lenses, polarization converters, holograms, unique antenna designs, and many others [1]–[4]. Metasurfaces, two-dimensional equivalents of metamaterials, are planar patterned surfaces composed of subwavelength periodic arrays of unit cells [5]. Owing to their extraordinary capability of manipulating the scattering behavior of the electromagnetic (EM) waves, the popularity of metasurfaces has been steadily increasing in the field of stealth technology [6]. Therein, the primary concern is to reduce the radar cross-section (RCS) to evade from the enemy's radar, which can be achieved by diminishing

The associate editor coordinating the review of this manuscript and approving it for publication was Jenny Mahoney.

back-scattered EM waves from the metallic objects [7]. The four leading practical approaches extensively used in the literature to achieve RCS reduction include [8], [9]: (i) utilization of radar absorbing materials (RAM), which transforms the incident EM wave into heat; (ii) reshaping the geometry of a target to redirect the incident EM energy away from the source; (iii) redirecting (or deflecting) the incident EM wave around the object (invisibility cloaking); (iv) phase cancellation, both active and passive. However, all of the aforementioned approaches predominantly exhibit narrow RCS reduction bandwidth, suffer from design complexity, and extreme losses.

Quite recently, considerable interest emerged in utilizing metamaterials for wideband RCS reduction. On a generic level, there are two strategies for reducing RCS by means of metamaterials. The first one is the usage of a perfect metamaterial absorber [10]–[14]. Such materials can absorb

EM waves and convert the energy into heat. Nevertheless, the RCS reduction band remains limited. The second strategy is to exploit the reflection phase controlling property of metasurfaces. Two types of surfaces have been presented that capitalize on this concept, i.e., electromagnetic gradient surface (EGS) [15], and checkerboard metasurface [6]. In EGS, the metal part of the surface is replaced by the unit cells of artificial magnetic conductors (AMC), and perfect electric conductors (PEC). The primary requirement in EGS is to maintain equal phase difference between the unit cells [16]. When the plane wave is incident from the normal direction, the EGS reflects back the tilted beam pattern, hence reducing the RCS. Due to non-linear relationship between the reflection phase curves and frequency, it is difficult to meet the equal phase difference condition over a wide frequency range. In a checkerboard metasurface, AMCs and PECs are arranged in an alternate fashion. The idea is to keep 180° phase difference between the AMC and PEC unit cells. Such a combination successfully diffuses the scattering energy at four lobes in the diagonal plane [17]. The EGS and checkerboard metasurfaces are low profile, robust and simple to manufacture [18]. Their major drawback is the narrowband performance of the AMC structure. Outside the working bandwidth, the AMC properties are similar to those of PEC, and the condition for 180° phase difference no longer holds. To overcome this drawback, PEC unit cell is substituted by another AMC unit cell operating at a different resonant frequency. Consequently, a dual-band design can be obtained [19], [20]. The idea of employing two AMCs in a checkerboard configuration was originally presented and developed by de Cos *et al.* [21], [22]. To achieve RCS reduction over a broad frequency band using this configuration, the phase difference between the two AMC unit cells should be 180° when their reflection amplitudes are the same and equal to one [18], [23]. In terms of electrical characteristics, the phase reflection curves of the two unit cells should remain parallel (i.e., equidistant) over the frequency band of interest. Notwithstanding, the reflection amplitudes of the combined unit cells are not always the same due to losses. On the other hand, it has been shown that −10 dB RCS reduction can be maintained over a frequency band if the phase difference between the two unit cells remains within 180° ± 37° range [25]. In a related vein, the concepts of coding metasurfaces [26], [27], diffusion metasurfaces [28], [29], programmable metasurfaces [30], Huygens' metasurfaces [31], as well as cloaking structures [32], have been proposed, which offer a control over the wavefront in a more sophisticated manner. The primary advantage of coding and diffusion metasurfaces over the checkerboard type surfaces is that it scatters the incident EM waves into all directions. In addition to that, coding metasurfaces are also exploited as an absorptive surface to realize essential RCS reduction [33].

Until now, numerous novel designs have been proposed for attaining wideband RCS reduction using metasurfaces [18], [21]–[29]. In the absence of reliable analytical methods,

the design process in the above-mentioned works typically relies on iterative full-wave EM simulations. Although such methods ensure accurate evaluation of the system response, they are time consuming and laborious due to a considerable amount of designer's interaction involved in the process. Furthermore, the design procedure relies mostly on empirical reasoning, physical intuition, or trial-and-error, which raises questions about the reliability and efficacy of such methods, as well as their capability of identifying truly optimum designs. From the perspective of hands-on design procedures, the problem is additionally aggravated by highly nonlinear input-output relationships. New and more sophisticated methods should be conceived to make the design process of metasurfaces computationally efficient, robust, and automated. In the recent years, data-driven techniques have emerged as promising tools, applicable to solving problems in many areas of science and engineering. Their advantages include the ability to yield acceptable solutions under time constraints and limited computational resources [34]–[41]. Some of the recent alternative approaches include phylogram analysis-based optimization method [42], island-based cuckoo search with polynomial mutation [43], hybrid swarm algorithm (a combination of the strengths in self-assembly and the particle swarm optimization) [44], and grey wolf optimizer-based method to tune pi-fuzzy controllers [45]. However, this work adopts some specific methods such as surrogate modeling frameworks and global optimization routines as the components of the developed metasurface design procedure.

The main objective of this paper is to enhance the RCS reduction bandwidth along with addressing the key challenges at the design level of a metasurface. The considered metasurface architectures are periodic arrays of two different AMC unit cells on the same ground plane in a checkerboard configuration. A surrogate-based framework proposed in this work involves fast kriging metamodels as well as a surrogate-assisted global search algorithm. The metamodels are trained using sampled EM simulation data, and used as the unit cell phase characteristic predictors at the optimization stage. Our procedure allows for identifying the optimum geometries of the individual unit cells (concurrently for the cell pairs) in a given parameter space. Optimality is understood in the sense of ensuring the maximum possible RCS bandwidth. The cell optimization is implemented as a grid-confined exhaustive search followed by local tuning. This approach is computationally feasible due to low dimensionality of the unit cell parameter space. It guarantees global optimality, and eliminates the need for the employment of stochastic search routines. At the same time, excellent accuracy of the metamodel ensures good agreement with EM simulation data over broad frequency range.

The presented approach allows for fully automated and globally optimum metasurface design within the assumed unit cell topology and the parameter space. It has been used to develop a novel checkerboard metasurface featuring 6 dB RCS reduction in a frequency range from 16 to 37 GHz.

The design is validated both numerically and experimentally, and shown to outperform the state-of-the-art benchmark structures with respect to the RCS reduction bandwidth. The technical novelty and the major contributions of this paper can be summarized as follows: (i) the development of a surrogate-assisted framework for reliable and efficient design optimization of checkerboard metasurfaces; (ii) the numerical verification of the framework as well as demonstration of its utility in the context of metasurface design, and (iii) the development of a novel high-performance checkerboard metasurface for broadband RCS reduction. It should be emphasized that the presented framework is—to the authors knowledge—the first comprehensive approach proposed in the literature for globally-optimum design of the unit cell geometries by means of fast metamodels.

The remaining part of the article is organized as follows. In Section II, the motivation for the proposed design framework is discussed, followed by the design and modeling of the unit cell, later used to illustrate the operation of the procedure, and the development of the broadband RCS reduction metasurface. In Section III, the description of the proposed surrogate-based approach and surrogate-assisted global optimization algorithm is provided. In Section V, a novel checkerboard metasurface is implemented and its scattering performance is investigated using full-wave EM simulations and physical measurements of the fabricated prototype. Section VI concludes the paper.

II. PROPOSED DESIGN APPROACH

This section briefly discusses the challenges of EM-driven metasuface design, and provides a motivation for the development of novel techniques that are not only more efficient than the traditional methods in computational terms, but also more reliable. Furthermore, a specific example of a unit cell (metasurface building block) is introduced to be used for the purpose of explaining the proposed machine-learning-based design methodology, and to develop a new high-performance metasurface featuring broadband RCS reduction.

A. MOTIVATION

Metasurface development necessarily involves full-wave EM analysis as the only tool capable of accurate evaluation of scattering properties of geometrically complex structures. Needless to say, the critical stage of the process, i.e., tuning of the unit cell geometry parameters to obtain desired phase characteristics has to be carried out at the level of EM simulation models. The fundamental challenges associated with parameter adjustment include:

- High simulation cost of the building blocks and the entire metasurface;
- Potential multi-modality of the optimization task resulting from the necessity of considering broadband responses, as well as mutual relationship between the unit cells of different geometries (zero/one cells);
- The lack of reasonable initial designs.

The last two factors generally lead to a situation where yielding satisfactory design requires the employment of global search routines, which are extremely expensive when executed directly the level of EM simulation models.

Clearly, optimum design of metasurfaces requires the development of novel procedures, capable of addressing the aforementioned difficulties. This work proposes utilization of data-driven modeling techniques to expedite the design process and to improve the optimization reliability. Towards this end, we utilize fast surrogate models (here, kriging interpolation [38]), as well as a combination of global and local optimization algorithms. The details of the framework will be presented in Section III, whereas its performance will be demonstrated in Section IV through the design of a chessboard metasurface featuring broadband RCS reduction.
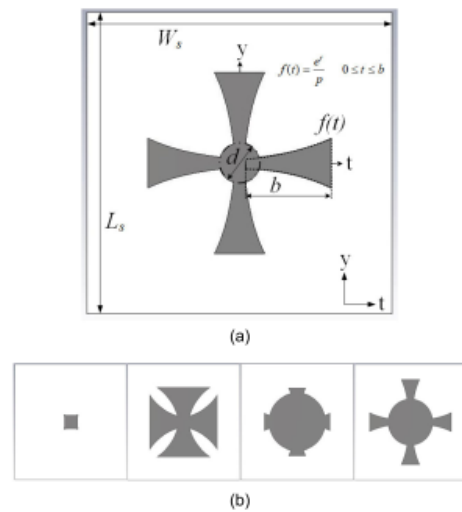

FIGURE 1. Configuration of the unit cell utilized in this work: (a) crusader cross topology, (b) four representative geometries within the parameter space.

B. UNIT CELL GEOMETRY

Figure 1(a) illustrates the geometry of the unit cell design utilized in this work. As shown, the topology resembles the crusader cross. The function $f(t)$ parameterizing the cross arm has the following analytical form

$$f(t) = \frac{e^t}{p} \quad 0 \leq t \leq b \tag{1}$$

where p, b, and d, are the adjustable parameters of the cell that determine its overall shape and size.

The specific data concerning the parameter space (lower/upper bounds) will be provided in Section III. This particular geometry has been chosen in order to ensure sufficient flexibility of the unit cell (cf. Fig. 1(b)) while limiting the number of adjustable parameters (here, three).

The latter facilitates the metamodeling-based optimization process, especially the construction of fast surrogate model.

A ground-backed Arlon AD250 lossy substrate ($\varepsilon_r = 2.5$, $h = 1.5$ mm, $\tan\delta = 0.0018$) is used in the unit cell design. During the simulations, metallization is represented as perfect electrical conductor (PEC). The overall size of the unit cell is $W_s \times L_s = 6 \times 6$ mm^2.

It should be noted that the geometries in Fig. 1(b) are for illustration purposes only, and they do not correspond to the final design. Notwithstanding, they are selected to illustrate the unit cell topologies in the assumed parameter space, and, thereby, to demonstrate the topological flexibility of the cell design.

It should be emphasized that the conventional design approaches are not reliable when optimizing such a topology where a small change in the design parameters drastically changes the cell geometry, and, consequently, the reflection phase. This applies to both interactive methods relying on parameter sweeping, but also direct EM-driven optimization techniques, the application of which is hindered by the entailed computational expenses.

III. OPTIMUM UNIT CELL DESIGN BY SURROGATE MODELING

In this section provides a description of the proposed data-driven approach to design optimization of the unit cell. We start by outlining the complete methodology, followed by a detailed explanation of the important components of the procedure. Utility of the proposed framework in the design process of unit cells is also considered. Demonstration of the novel metasurface based on the optimized cell geometries will be provided in Section IV.

The optimization procedure proposed in this paper accounts for geometrical flexibility of the unit cells, which makes global search necessary. At the same time, it capitalizes on the fact that the considered parameter spaces are of low dimensionality, which allows for a construction of fast metamodels, and realization of the global search process in a deterministic manner. As a result, it guarantees identification of a globally optimum design within a reasonable timeframe and it is fully deterministic. The latter alleviates the difficulties pertinent to poor repeatability of solutions, featured by nature-inspired algorithms (the latter currently being the methods of choice for solving this type of problems). At the same time, utilization of surrogates speeds up the search process when compared to direct EM-driven optimization using, e.g., population-based methods.

A. DESIGN METHODOLOGY

The goal of the proposed metamodeling-based design approach is to find a pair of unit cell geometries featuring the phase difference within the range of $180° \pm \alpha_{max}$ over a possibly broad frequency range F. Here, α_{max} is set to $37°$, which is the value recommended in the literature (e.g., [24]). The operation of the optimization framework is outlined below, whereas the details concerning its major components

are provided in Sections III.B through III.E. The vector of adjustable variables of the unit cell, and the response of its EM simulation model will be denoted as $x = [x_1 \dots x_n]^T \in X$, and $P(x)$, respectively. The latter represents the phase reflection characteristics. The parameter space X is determined by the user-defined lower and upper bounds $l = [l_1 \dots l_n]^T$ and $u = [u_1 \dots u_n]^T$ such that $l_l \leq x_l \leq u_l$, $l = 1, \dots, n$.

The unit cell optimization is carried out over the Cartesian product $X \times X$ and aims at finding the vector $x_p^* = [(x^{(1)*})^T (x^{(3)*})^T]^T$ that represents a pair of cell geometries corresponding to the maximum (continuous) range of frequencies for which the condition mentioned at the beginning of the section, i.e., $180° - \alpha_{max} \leq \Delta P(x^{(1)*}, x^{(3)*}) \leq 180° + \alpha_{max}$, is satisfied. In plain words, we strive to determine the dimensions of both unit cells so that the aforementioned phase condition is satisfied for as broad frequency range as possible. The cells have to be optimized concurrently, because the phase difference simultaneously depends on both parameter vectors. Consequently, all dimensions are aggregated into a single vector x_p. Formally, the design problem can be stated as follows:

$$x_p^* = \arg \min_{x_p \in X \times X} U(\Delta P(x_p)) \qquad (2)$$

The analytical form of the objective function U has been given in Section III.C.

The algorithmic flow of the optimization process is as follows:

1. Uniformly allocate N samples $x^{(k)}$, $k = 1, \dots, N$, within X and acquire the responses $P(x^{(k)})$ from the EM simulation model;
2. Construct a Kriging surrogate $S(x)$ in X using $\{x^{(k)}, P(x^{(k)})\}_{k=1,\dots,N}$, as the training dataset (cf. Section III.B);
3. Find the initial approximation $x_p^{(0)}$ of the global optimum of the surrogate S (in an exhaustive manner) on the structured grid (cf. Section III.D);
4. Find the refined design x_p^* by solving (1) using $x_p^{(0)}$ as a starting point. The refinement process is realized using local search routines (cf. Section III.E).

In Step 1, the algorithm starts by uniformly allocating samples within the parameter space and acquiring the training data through EM simulation of the unit cells. The purpose of the training data acquisition is to gather information about the properties of the unit cells in terms of their phase characteristics across the parameter space. This knowledge will be then encoded for further use in the form of a fast surrogate model, which will replace expensive EM simulation in the design optimization process.

In Step 2, a kriging metamodel is constructed to be used as a predictor of the cell phase characteristics over the space X. The metamodel makes predictions about the unit cell phase characteristics as functions of the geometry parameters of the cell. Because it is essentially an analytical model (kriging surrogates are combinations of low-order polynomial-based regression models and linear combinations of kernel

functions, e.g. Gaussian), it is fast to evaluate. Furthermore, it is interpolative, i.e., it agrees perfectly with the EM simulation data at the training locations.

In Step 3 of the procedure, the metamodel is employed in the global search. This step, described in detail in Sections III.C and III.D, employs the objective function (3) and carried out exhaustive search over a dense rectangular grid defined over the parameter space. This way of implementing the search process is justified by low dimensionality of the problem, the availability of fast metamodel. It has significant advantages over, e.g., nature-inspired population-based procedures for the considered case because it is fully deterministic and guarantees identification of the optimum design when coupled with the local refinement.

In Step 4, the resolution of the design found through grid-constrained search is refined through conventional local (gradient-based) optimization. The details are provided in Section III.E. At this stage, the objective function (3) is used as well.
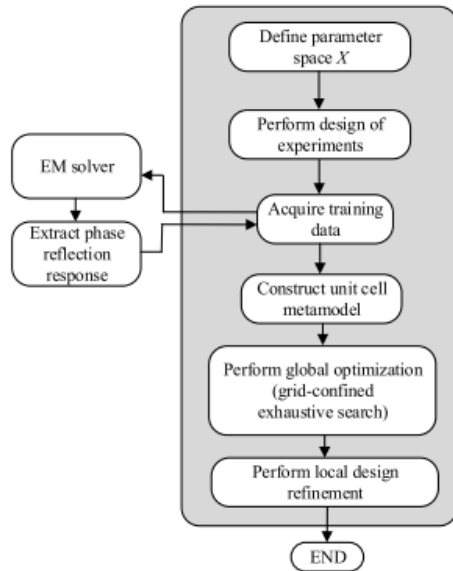
FIGURE 2. Flow diagram of the proposed surrogate modeling-based framework for design optimization of metasurface unit cells.

As mentioned before, the utilization of the surrogate allows for expediting the optimization procedure to a great extent as compared to direct EM-driven optimization. The flow diagram of the proposed surrogate-based design framework has been shown in Fig. 2.

An alternative approach in this venture could be the utilization of physics-based surrogate models [47], which have become popular in high-frequency design over the last years. Physics-based methods exploit the problem-specific knowledge, typically, in the form of low-fidelity EM or equivalent network models. Some of popular techniques of this class

include space mapping [48], and response correction methods (e.g., shape preserving response correction [49], adaptive response scaling [50]). However, in the considered case of unit cell optimization, the employment of data-driven surrogates seems more appropriate having in mind low dimensionality of the parameter space as well as the fact that global exploration is needed. These, along with the lack of convenient candidates for fast low-fidelity representation makes physics-based surrogates impractical.

B. SURROGATE MODELING

The surrogate model S is constructed within $x \in X$ using kriging interpolation [38]. The surrogate is identified using the training data samples $\{x^{(k)}, P(x^{(k)})\}_{k=1,...,N}$, where $P(x)$ represents the response of the EM-simulation model, whereas N denotes the total number of samples. The design of experiments strategy is a rectangular grid $7 \times 12 \times 7$ (thus, $N = 588$), which is a suitable arrangement due to low-dimensionality of the parameter space.

The number of grid nodes in each direction is determined based on the large-scale sensitivity analysis with a larger number of nodes set up for the second variable, which has been found to affect the unit cell phase characteristics in a more significant manner than the remaining variables. The kriging model is set up with the first-order polynomial regression model used as a trend function, and a Gaussian correlation function.

C. OBJECTIVE FUNCTION DEFINITION

The design task has been formulated in Section III.A (cf. (1)) as identification of a pair of unit cell geometries $x_p^* = [(x^{(1)*})^T \ (x^{(3)*})^T]^T$ that maximize the frequency range for which the phase difference satisfies the condition $180° - \alpha_{max} \leq \Delta P(x^{(1)*}, x^{(3)*}) \leq 180° + \alpha_{max}$. The analytical form of the objective function U is defined as

$$U(\Delta P(x_p)) = -[f_R(x_p) - f_L(x_p)] \qquad (3)$$

where f_L and f_R are the frequencies determining the largest frequency interval for which the phase difference condition is satisfied for all frequencies $f \in [f_L, f_R]$. The minus sign in (3) allows for turning the maximization task into the minimization one according to (1). It should be noted that both frequencies are extracted from the phase characteristics of the unit cells using a postprocessing routine implemented in Matlab.

D. GLOBAL OPTIMIZATION

Step 3 of the optimization procedure (cf. Section III.A) is a grid-confined global search. Let $M_{m1...mn}$ be a rectangular grid of the form $x \in M_{m1...mn}$ if and only if $x = [x_1 ... x_n]^T$ is of the form $x_k = l_k + j_k[(u_k - l_k)/m_k]$, $k = 1, ..., n$, where m_k is and grid-defining integer for the kth variable, and $j_k \in \{0, 1, ..., m_k\}$. The initial approximation $x_p^{(0)}$ of the global optimum of S is found as

$$x_p^{(0)} = \arg \min_{x^{(1)}, x^{(3)} \in M_{m1...mn}} U(\Delta P([(x^{(1)})^T \ (x^{(3)})^T]^T)) \qquad (4)$$

In other words, $x_p^{(0)}$ is obtained by searching through all possible pairs of unit cell geometries $x^{(1)} \in M_{m1...mn}$ and $x^{(2)} \in M_{m1...mn}$ and determining the one that minimizes U. Note that this is an exhaustive search but its computational cost is negligible because the surrogate model S is fast, and the number of parameters is low. Additionally, the entire process is vectorized to further speed-up the operation. In this work, we use $m_k = 9$ for $k = 1, \ldots, n$.

The optimization procedure is governed by the following control parameters:

- The number N of the training data points to construct the surrogate model. This number is adjusted to ensure that the surrogate model accuracy in terms of the relative RMS error is at the level of one percent (which gives almost perfect visual agreement between the EM simulated data and the metamodel outputs;

- Density of the search grid m_k, $k = 1, \ldots, n$. This parameter is of secondary importance because the objective of global search is only to provide a starting point for design refinement (cf. Section III.E), i.e., to ensure that the grid-constrained optimum is sufficiently close to the global optimum. The value used in this work ($m_k = 9$) by far exceeds this requirement.

It can be observed that the optimization procedure has only two control parameters, both of which can be easily adjusted to ensure the reliability of the process. This is one of important advantages of the method. The local design refinement uses off-the-shelf algorithm (cf. Section III.E) with default setup, i.e., no control parameters have to be adjusted.

E. DESIGN REFINEMENT
The last stage of the optimization process (Step 4) is local refinement, using $x_p^{(0)}$ found in Step 3, as a starting point. The refinement is executed using Matlab's *fmincon* procedure [46], which is a variation of the sequential quadratic programming (SQP) method [46]. Again, the computational cost of this stage is negligible because it is executed at the level of the kriging metamodel.

F. OPTIMIZATION RESULTS
Figure 1(b) provides a general idea about the type of structures under consideration. For the unit cell of Fig. 1(b), there are three parameters, p, b, and d, that determine the shape of the unit cell. Hence, the vector of designable variables is $x = [p \; b \; d]^T$; L_s and W_s are fixed. The parameter space X is defined by the lower and upper bounds $l = [3.5 \; 0.3 \; 0.2]^T$, and $u = [10 \; 1.6 \; 2.4]^T$; all dimensions are in mm. To achieve the best predictive power of a metamodel, the training points are arranged in a uniform grid $M_{7.12.7}$ (cf. Section III.B) with a total of 588 samples. The acquired data is divided into the training (85 percent) and the test data (15 percent) to be used for split-sample error estimation. The frequency-domain solver of the CST Microwave Studio is utilized to evaluate the phase reflection responses of the unit cell.

The absolute error of the surrogate model is as low as 0.86 degrees (averaged over the testing set) with the standard
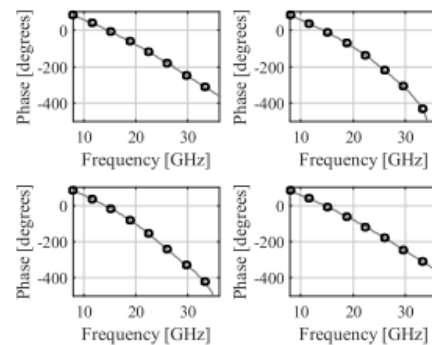

FIGURE 3. Performance of the unit cell metamodel: EM model (–) and surrogate responses (o) at the selected test locations.

deviation of 1.7 degrees. This means that the metamodel is very reliable, especially when considering the typical range of the unit cell phase response (>400 degrees). Figure 3 shows the surrogate and EM-simulated cell responses at the selected test locations. The visual agreement between the two data sets is excellent, which corroborates the design utility of the metamodel.

FIGURE 4. Geometries of the globally optimized unit cell designs: Cell 1 (left), and Cell 0 (right).

The trained metamodel has been optimized according to Steps 3 and 4 of the procedure of Section III.A. The optimal cells obtained in the process are $x^{(1)*} = [4.9444 \; 0.8778 \; 0.9302]^T$ and $x^{(3)*} = [4.2222 \; 1.6 \; 2.4]^T$. Figure 4 shows the cell geometries, for convenience, labeled as Cell 0 and Cell 1. Verification of these designs has been conducted by comparing their phase characteristics with the EM simulation data. As demonstrated in Fig. 5, the agreement between the surrogate and EM-simulated responses is excellent. This confirms the efficacy of the proposed machine-learning-based design framework.

The reflection phase and amplitude of the unit cells along with the reflection phase difference between the two cells are shown in Fig. 6. It can be observed that the condition $180° - 37° \leq \Delta P(x^{(1)*}, x^{(3)*}) \leq 180° + 37°$ is satisfied for the frequencies from 16 GHz to 35 GHz. Hence, more than 19 GHz RCS reduction bandwidth can be anticipated [25]. It should be reiterated that the objective of the optimization procedure is to find a globally-optimum design of the unit cells that maximizes the RCS reduction bandwidth, i.e., a pair of designs featuring the phase difference of 180 ± 37 degrees over possibly a broad frequency range. The outcome of the optimization procedure (pair of unit cells) serve as a building
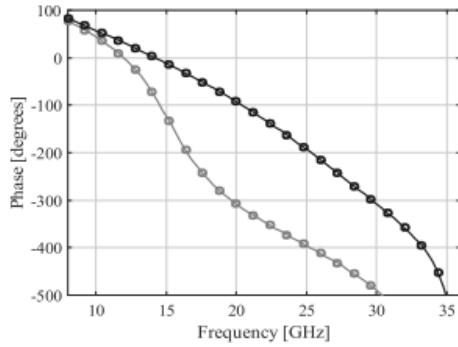
FIGURE 5. Phase reflection response for the optimized unit cell designs: EM model (–) metamodel responses (o). The Cell 0 and Cell 1 responses are marked black and grey, respectively.
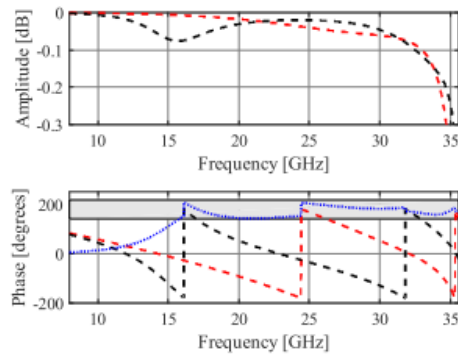

FIGURE 6. Reflection performance of the optimized unit cells: reflection amplitude (top) and reflection phase (bottom). The responses of Cell 0 and Cell 1 are marked black and red, respectively, whereas the blue curve indicates the reflection phase difference. The gray-shaded area in the bottom plot indicates the range of acceptable phase differences.

block of a high-performance RCS reduction metasurface as described in Section IV.

IV. NOVEL METASURFACE CONFIGURATION. NUMERICAL AND EXPERIMENTAL VALIDATION

This section introduces the configuration of a novel metasurface design. The monostatic and bistatic RCS performance of the proposed structure is discussed in detail. The experimental setup is also illustrated, along with the comparison of simulation and measurement results of the checkerboard measurface. Finally, benchmarking against the state-of-the-art designs is discussed.

A. CHECKERBOARD METASURFACE PERFORMANCE

The operating principle of a checkerboard metasurfaces is to interleave the two structures featuring 180° phase difference so that the backscattered fields are cancelled out, and a distinct scattering patterns are produced. Theoretically, monostatic and bistatic RCS reduction can be approximated by the

array theory [51]. The concept of the RCS reduction can be understood by recalling a planar array having a progressive phase shift of 180° among elements within a particular frequency band. In other words, the checkerboard measurface exploits the anti-phase reflection property of periodic arrays to manipulate the scattering behavior.
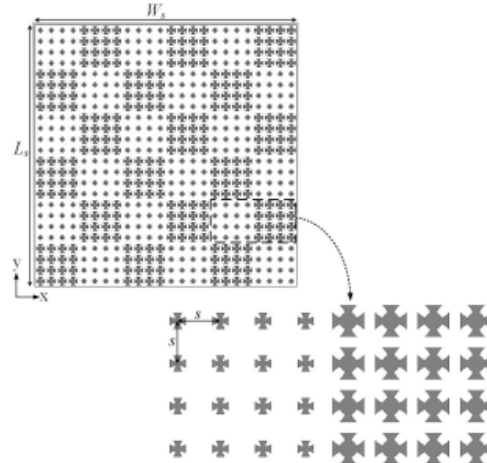
FIGURE 7. Geometry configuration of the proposed metasurface.

In order to enable the aforementioned property, in the first step, the optimum unit cell designs, i.e., Cell 0 and Cell 1, featuring a phase difference of 180° ± 37° are obtained (cf. Section III). Hereafter, the periodic arrays containing multiple copies of Cell 0 and Cell 1 as the building blocks are employed in an alternate manner to realize a checkerboard metasurface. Figure 7 illustrates the proposed checkerboard metasurface comprising thirty-six elements: eighteen 4 × 4 periodic arrays of Cell 0 and eighteen 4 × 4 periodic arrays of Cell 1. Subsequently, the resulting 6 × 6 checkerboard surface is characterized. Note that the size of the periodic arrays is decided by considering the fact that diffractions due to discontinuities among the neighboring arrays do not significantly contribute when the overall size of a single array is greater than half wavelength [52]. The total size of the surface is $W_s \times L_s = 144 \times 144$ mm^2. The inter-element spacing of individual unit cells in an array is $s = 6$ mm.

The surface is implemented on a ground-backed Arlon AD250 lossy substrate ($\varepsilon_r = 2.5$, $h = 1.5$ mm, tan$\delta = 0.0018$). To test the RCS performance of a proposed metasurface, a PEC surface of a similar size is also implemented to be utilized as a reference surface. The time-domain solver of CST Microwave Studio is used for both the monostatic and bistatic RCS analysis.

In order to validate the anticipated broadband RCS reduction of the proposed metasurface, its monostatic RCS performance for normal incidence has been determined. Figure 8 shows the reflection characteristics of the PEC surface along
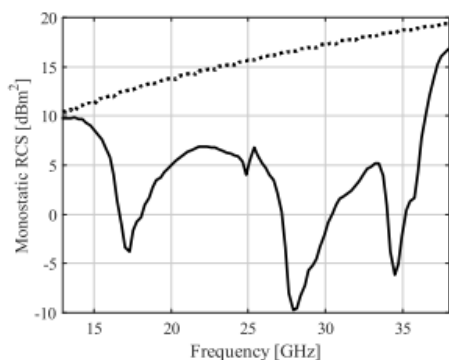
FIGURE 8. Monostatic RCS of a metallic surface (. . .) and the proposed checkerboard metasurface (—).
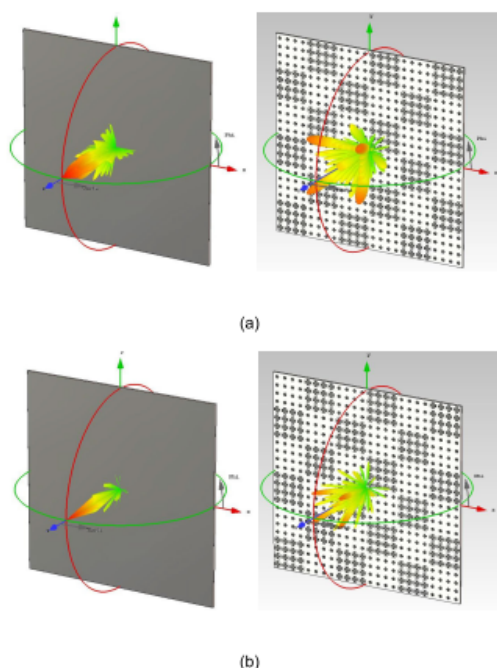

(a)

(b)

FIGURE 9. 3D scattering performance of the PEC surface (left) and the proposed checkerboard metasurface (right): (a) at 17 GHz, and (b) at 32 GHz.

with the proposed metasurface. It is apparent that the RCS reduction occurs in a broad frequency range, i.e., from 15.7 GHz to 38 GHz, which confirms the low observable property of the metasurface.

The 3-D bistatic RCS patterns of the proposed metasurface and the metallic surface of same size has been presented in Fig. 9. It can be observed that the reflected waves from the proposed surface, under normal incidence, scatter into four diagonal planes. It corroborates minimum reflections from

the metasurface in the boresight direction, as the incident waves are reflected into different directions. On the contrary, the metallic surface features strong reflections in the boresight direction, in a single lobe, when the plane wave impinges on it from the normal direction.
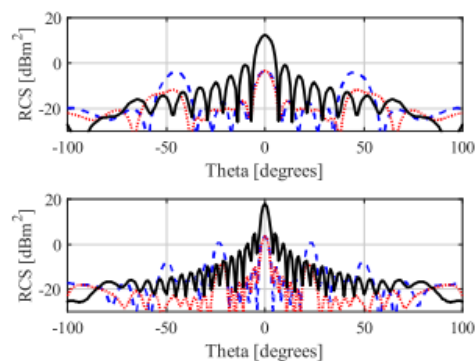
FIGURE 10. Bistatic RCS performance at 17 GHz (top) and at 32 GHz (bottom) along the principle planes. The two planes $\phi = 0$ and $\phi = 90$ are marked blue and red, respectively, whereas the black curve indicates the scattered field form the PEC surface.
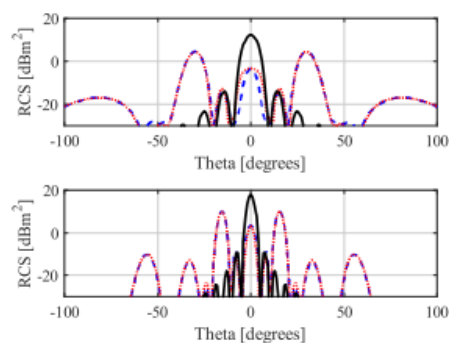
FIGURE 11. Bistatic RCS performance at 17 GHz (top) and at 32 GHz (bottom) along the diagonal planes. The two planes $\phi = 45$ and $\phi = 135$ are marked blue and red, respectively, whereas the black curve indicates the scattered field form the PEC surface.

The scattered field versus the elevation angle theta θ along the principal and the diagonal planes are demonstrated in Figs. 10 and 11, respectively. The bistatic RCS performance of the proposed metasurface is compared with the PEC surface. The results indicate that the maximum RCS in the principal planes is 16.0 dB lower than the maximum RCS for the PEC ground plane, at both considered frequencies. Subsequently, in the diagonal planes, the maximum RCS of the proposed surface is 15.2 dB lower than a PEC ground plane. Hence, a significant RCS reduction has been observed for the proposed metasurface in the principal as well as the diagonal planes. This reduction occurs because the reflected fields are redirected into four main lobes, instead of the single main lobe of the PEC surface, (cf. Fig. 9).
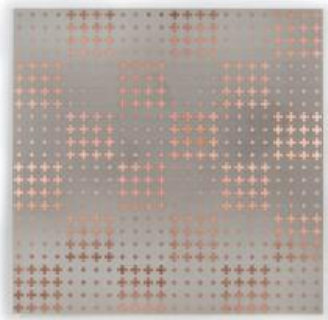
FIGURE 12. Photograph of the prototyped checkerboard metasurface.

B. MEASUREMENT SETUP AND EXPERIMENTAL VALIDATION

Following the EM-simulation-based verification, the prototype metasurface has been fabricated and measured. Figure 12 show a photograph of the structure. The RCS has been measured in terms of reflectivity, owing to limited amenities. The same size PEC surface has been used as a reference to determine the RCS reduction of our metasurface.
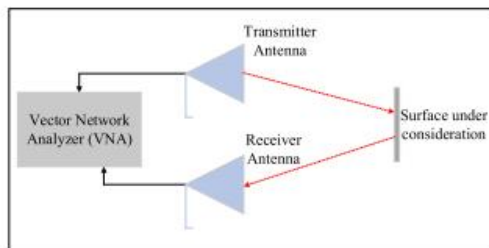

FIGURE 13. Block diagram of the physical measurement environment.

For the sake of measurements, two PE9850/2F-15 horn antennas, operating from 26.5 GHz to 40.0 GHz, have been utilized as a transmitter and a receiver. The monostatic RCS characteristics of a checkerboard and a PEC surface has been evaluated by measuring the antenna transmission coefficients. The block diagram of the measurement setup has been provided in Fig. 13. The measurements have been carried out using the anechoic chamber of Reykjavik University (cf. Fig. 14). The comparison between the simulated and measured RCS reduction is depicted in Fig. 15. The agreement between the datasets is very good. A certain discrepancy can be attributed to the fabrication tolerances, as well as the misalignment of the transmitter/receiver antenna with respect to metasurface during measurements. The latter is essential considering that the experimental setup is for capturing reflections. A slight misalignment could
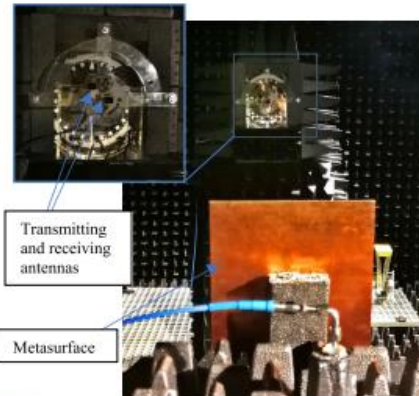

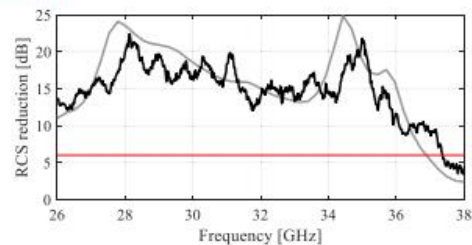**FIGURE 14.** Measurement setup at Reykjavik University.

FIGURE 15. Measured (black) and simulated (gray) RCS reduction performance comparison. The red curve indicates 6-dB RCS reduction threshold.

lead to relatively high inaccuracies. Nevertheless, the measurements corroborate 6-dB RCS reduction within the frequency range of 26.5 GHz and 38 GHz. As mentioned before, the lower edge is limited by the available hardware. The measured RCS reduction bandwidth of the proposed checkerboard metasurface and the expected bandwidth anticipated from the phase difference curves (cf. Fig. 6) are similar.

The above findings allow us to conclude that the proposed checkerboard metasurface features low scattering property in a broadband frequency range, and, therefore, it has the potential to replace the metallic surfaces in the applications where high stealthiness is essential.

C. BENCHMARKING

For the sake of benchmarking, the performance of the proposed checkerboard metasurface has been compared with the recent metasurfaces from the literature, see Table 1. The comparison is carried out in terms of the RCS reduction bandwidth. It can be observed that the proposed metasurface outperforms other designs with respect to fractional/relative RCS reduction bandwidth. It should be emphasized that apart from proposing a novel metasurface, an efficient surrogate-assisted design framework is also provided—for the first time—to facilitate the design procedure of such surfaces. As a matter of fact, it is rigorous optimization that provides

TABLE 1. Proposed metasurface versus state-of-art designs.

Ref	Total thickness (mm)	Period (mm)	6-dB RCS reduction bandwidth (GHz)	Fractional bandwidth (%)
[17]	3	10	5.0–7.2	36
[25]	3.175	15	7.7–16.5	72
[26]	6.35	15	4.0–8.6	73
[27]	3	5.2	9.0–19.8	75
[28]	3	5	5.1–7.9	43
[29]	2.35	6	8.0–12.1	40
[30]	3.18	6	5.7–13	78
[53]	4.81	10	5.5–12.9	80
Proposed	1.52	6	15.7–38	83

a competitive edge over less formal design approaches, and manifests itself through better properties of the resulting metasurface. As mentioned before, the crucial components of the procedure are those that take into account the specifics of the problem: the parameter space dimensionality, expensive (EM-based) evaluation of the unit cell characteristics, and the need for global search.

V. CONCLUSION

This article proposed a surrogate-assisted framework for rapid design of high-performance metasurfaces featuring broadband RCS reduction. Low RCS of a surface translates to its low observable nature, which is highly desirable for the stealth technology. Our procedure involves a construction of a fast metamodel that replaces the CPU-intensive EM simulations in both stages of the design process, i.e., the global search, and local (gradient-based) refinement. The optimization is executed to identify the optimum until cell geometries within the user-defined bounds. By employing the proposed methodology, a computational burden of the design process can be significantly reduced. Finally, a novel checkerboard metasurface, enabling broadband RCS reduction, has been developed using our framework. The monostatic and bistatic performance of the proposed checkerboard metasurface has been validated both numerically and experimentally. The numerical results indicate that the metasurface features low scattering property in a broadband frequency range, i.e., from 15.7–38 GHz. The experimental data confirms these findings starting from 26.5 GHz, which is due to the limitations of the available hardware. The proposed metasurface has been benchmarked against state-of-the-art designs demonstrated to be superior in terms of the RCS reduction bandwidth. This also validates the design utility of the presented metamodeling-based procedure in the context of metasurface development. As a matter of fact, the design of the above structure provides a link between the theory (here, a simulation-based design optimization procedure), and application, which is the development of high-performance metasurface with the intended use in stealth technology.

The authors believe that this study is a step toward exploring the data-driven techniques in the design of high-performance metasurfaces for RCS reduction, where intuition-inspired methods are still widespread although generally lack the ability to yield truly optimum results. Application of surrogate-based methods, including fast metamodels, improves reliability, enables global optimization in reasonable timeframe, eventually leading to the improvement of metasurface performance figures, as demonstrated through the specific design proposed in this work.

REFERENCES

[1] T. J. Cui, D. R. Smith, and R. Liu, *Metamaterials Theory, Design, and Applications*. New York, NY, USA: Springer, 2010.

[2] F. Aieta, P. Genevet, M. A. Kats, N. Yu, R. Blanchard, Z. Gaburro, and F. Capasso, "Aberration-free ultrathin flat lenses and axicons at telecom wavelengths based on plasmonic metasurfaces," *Nano Lett.*, vol. 12, no. 9, pp. 4932–4936, Sep. 2012.

[3] X. Gao, X. Han, W.-P. Cao, H. O. Li, H. F. Ma, and T. J. Cui, "Ultrawideband and high-efficiency linear polarization converter based on double V-shaped metasurface," *IEEE Trans. Antennas Propag.*, vol. 63, no. 8, pp. 3522–3530, Aug. 2015.

[4] F.-C. Huang, C.-N. Chiu, T.-L. Wu, and Y.-P. Chiou, "A circular-ring miniaturized-element metasurface with many good features for frequency selective shielding applications," *IEEE Trans. Electromagn. Compat.*, vol. 57, no. 3, pp. 365–374, Jun. 2015.

[5] S. Sun, Q. He, S. Hao, S. Xiao, and L. Zhou, "Electromagnetic metasurfaces: Physics and applications," *Adv. Opt. Photon.*, vol. 11, no. 2, pp. 380–479, 2019.

[6] M. Paquay, J.-C. Iriarte, I. Ederra, R. Gonzalo, and P. de Maagt, "Thin AMC structure for radar cross-section reduction," *IEEE Trans. Antennas Propag.*, vol. 55, no. 12, pp. 3630–3638, Dec. 2007.

[7] G. A. Rao and S. P. Mahulikar, "Integrated review of stealth technology and its role in airpower," *Aeronaut. J.*, vol. 106, no. 1066, pp. 629–642, Dec. 2002.

[8] E. F. Knott, J. F. Schaeffer, and M. T. Michael, *Radar Cross Section*. Rijeka, Croatia: SciTech, 2004.

[9] T. A. Khan, J. X. Li, Z. Li, M. Abdullah, J. Chen, and A. X. Zhang, "Design of Vivaldi antenna with wideband reduced radar cross section," *AEU Int. J. Electron. Commun.*, vol. 95, pp. 47–51, Oct. 2018.

[10] N. I. Landy, S. Sajuyigbe, J. J. Mock, D. R. Smith, and W. J. Padilla, "Perfect metamaterial absorber," *Phys. Rev. Lett.*, vol. 100, no. 20, pp. 207–402, 2008.

[11] Y. Cheng and H. Yang, "Design simulation and measurement of metamaterial absorber," *J. Appl. Phys.*, vol. 108, no. 8, Art. no. 34906, 2010.

[12] F. Costa, A. Monorchio, and G. Manara, "Analysis and design of ultra thin electromagnetic absorbers comprising resistively loaded high impedance surfaces," *IEEE Trans. Antennas Propag.*, vol. 58, no. 5, pp. 1551–1558, May 2010.

[13] Y. Ma, "A terahertz polarization insensitive dual band metamaterial absorber," *Opt. Lett.*, vol. 36, no. 6, pp. 945–947, 2011.

[14] Y. Liu and X. Zhao, "Perfect absorber metamaterial for designing low-RCS patch antenna," *IEEE Antennas Wireless Propag. Lett.*, vol. 13, pp. 1473–1476, 2014.

[15] K. Chang, "Electromagnetic gradient surface and its application to flat reflector antennas," Ph.D. dissertation, Dept. Elect. Electron. Eng., Dept. Elect. Comput. Eng., Yonsei Univ., Seoul, South Korea, 2009.

[16] H. P. Seo, Y. S. Kim, Y. Lim, and Y. J. Yoon, "Improving phase continuity in electromagnetic gradient surface for large reflecting structures," in *Proc. IEEE Int. Symp. Antennas Propag.*, Jul. 2012, pp. 1–2.

[17] Y. Zhao, X. Cao, J. Gao, Y. Sun, H. Yang, X. Liu, Y. Zhou, T. Han, and W. Chen, "Broadband diffusion metasurface based on a single anisotropic element and optimized by the simulated annealing algorithm," *Sci. Rep.*, vol. 6, no. 1, Jul. 2016, Art.no. 23896.

[18] J. C. I. Galarregui, A. T. Pereda, J. L. M. de Falcón, I. Ederra, R. Gonzalo, and P. de Maagt, "Broadband radar cross-section reduction using AMC technology," *IEEE Trans. Antennas Propag.*, vol. 61, no. 12, pp. 6136–6143, Dec. 2013.

[19] J. C. Iriarte, I. Ederra, R. Gonzalo, and P. de Maagt, "Dual band RCS reduction using planar technology by combining AMC structures," in *Proc. 3rd Eur. Conf. Antennas Propag.*, Mar. 2009, pp. 3708–3709.

[20] J. C. Iriarte, J. L. M. de Falcón, I. Maestrojuan, I. Liberal, A. Rebollo, I. Ederra, R. Gonzao, and P. de Maagt, "Broadband RCS reduction using AMC technology," in *Proc. 5th Eur. Conf. Antennas Propag.*, Apr. 2011, pp. 1322–1323.

[21] M. E. de Cos, Y. Álvarez, and F. Las-Heras, "On the influence of coupling AMC resonances for RCS reduction in the SHF band," *Prog. Electromagn. Res.*, vol. 117, pp. 103–119, May 2011.

[22] M. E. de Cos, Y. Álvarez, and F. Las-Heras, "RCS reduction using a combination of artificial magnetic conductors," in *Proc. 5th Eur. Conf. Antennas Propag.*, Apr. 2011, pp. 1336–1340.

[23] Y. Fu, Y. Li, and N. Yuan, "Wideband composite AMC surfaces for RCS reduction," *Microw. Opt. Technol. Lett.*, vol. 53, no. 4, pp. 712–715, Apr. 2011.

[24] S. H. Kim and Y. J. Yoon, "Wideband radar cross-section reduction on checkerboard metasurfaces with surface wave suppression," *IEEE Antennas Wireless Propag. Lett.*, vol. 18, no. 5, pp. 896–900, May 2019.

[25] W. Chen, C. A. Balanis, and C. R. Birtcher, "Checkerboard EBG surfaces for wideband radar cross section reduction," *IEEE Trans. Antennas Propag.*, vol. 63, no. 6, pp. 2636–2645, Jun. 2015.

[26] Q. Zheng, Y. Li, J. Zhang, H. Ma, J. Wang, Y. Pang, Y. Han, S. Sui, Y. Shen, H. Chen, and S. Qu, "Wideband, wide-angle coding phase gradient metasurfaces based on pancharatnam-berry phase," *Sci. Rep.*, vol. 7, no. 1, Apr. 2017, Art. no. 43543.

[27] X. Liu, J. Gao, L. Xu, X. Cao, Y. Zhao, and S. Li, "A coding diffusive metasurface for RCS reduction," *IEEE Antennas Wireless Propag. Lett.*, vol. 16, pp. 724–727, 2017.

[28] Y. Zhuang, G. Wang, J. Liang, T. Cai, W. Guo, and Q. Zhang, "Flexible and polarization-controllable diffusion metasurface with optical transparency," *J. Phys. D, Appl. Phys.*, vol. 50, no. 46, Nov. 2017, Art. no. 465102.

[29] T. A. Khan, J. Li, J. Chen, M. U. Raza, and A. Zhang, "Design of a low scattering metasurface for stealth applications," *Materials*, vol. 12, no. 18, p. 3031, Sep. 2019.

[30] H. Yang, X. Cao, F. Yang, J. Gao, S. Xu, M. Li, X. Chen, Y. Zhao, Y. Zheng, and S. Li, "A programmable metasurface with dynamic polarization, scattering and focusing control," *Sci. Rep.*, vol. 6, no. 1, Dec. 2016, Art. no. 35692.

[31] M. Chen, M. Kim, A. M. H. Wong, and G. V. Eleftheriades, "Huygens' metasurfaces from microwaves to optics: A review," *Nanophotonics*, vol. 7, no. 6, pp. 1207–1231, Jun. 2018.

[32] J. Ji, J. Jiang, G. Chen, F. Liu, and Y. Ma, "Research on monostatic and bistatic RCS of cloaking based on coordinate transformation," *Optik*, vol. 165, pp. 117–123, Jul. 2018.

[33] S. Sui, H. Ma, J. Wang, Y. Pang, M. Feng, Z. Xu, and S. Qu, "Absorptive coding metasurface for further radar cross section reduction," *J. Phys. D, Appl. Phys.*, vol. 51, no. 6, Feb. 2018, Art. no. 065603.

[34] B. Lusch, J. N. Kutz, and S. L. Brunton, "Deep learning for universal linear embeddings of nonlinear dynamics," *Nature Commun.*, vol. 9, no. 1, Dec. 2018, Art. no. 4950.

[35] X. Lin, Y. Rivenson, N. T. Yardimci, M. Veli, Y. Luo, M. Jarrahi, and A. Ozcan, "All-optical machine learning using diffractive deep neural networks," *Science*, vol. 361, no. 6406, pp. 1004–1008, Sep. 2018.

[36] A. D. Tranter, H. J. Slatyer, M. R. Hush, A. C. Leung, J. L. Everett, K. V. Paul, P. Vernaz-Gris, P. K. Lam, B. C. Buchler, and G. T. Campbell, "Multiparameter optimisation of a magneto-optical trap using deep learning," *Nature Commun.*, vol. 9, no. 1, Dec. 2018, Art. no. 4360.

[37] J. Peurifoy, Y. Shen, L. Jing, Y. Yang, F. Cano-Renteria, B. G. DeLacy, J. D. Joannopoulos, M. Tegmark, and M. Soljačić, "Nanophotonic particle simulation and inverse design using artificial neural networks," *Sci. Adv.*, vol. 4, no. 6, Jun. 2018, Art. no. eaar4206.

[38] T. W. Simpson, J. D. Poplinski, P. N. Koch, and J. K. Allen, "Metamodels for computer-based engineering design: Survey and recommendations," *Eng. Comput.*, vol. 17, no. 2, pp. 129–150, Jul. 2001.

[39] X. Chen, W. Xue, H. Shi, J. Yi, and W. E. I. Sha, "Orbital angular momentum multiplexing in highly reverberant environments," *IEEE Microw. Wireless Compon. Lett.*, vol. 30, no. 1, pp. 112–115, Jan. 2020.

[40] X. Chen, W. Xue, H. Shi, L. Wang, S. Zhu, and A. Zhang, "Improving field uniformity using source stirring with orbital angular momentum modes in a reverberation chamber," *IEEE Microw. Wireless Compon. Lett.*, vol. 29, no. 8, pp. 560–562, Aug. 2019.

[41] S. Koziel and S. Ogurtsov, "Antenna design by simulation-driven optimization," in *Surrogate-Based Approach*. New York, NY, USA: Springer, 2014.

[42] A. Soares, R. Râbelo, and A. Delbem, "Optimization based on phylogram analysis," *Expert Syst. Appl.*, vol. 78, pp. 32–50, Jul. 2017.

[43] B. H. Abed-Alguni, "Island-based cuckoo search with highly disruptive polynomial mutation," *Int. J. Artif. Intell.*, vol. 17, no. 1, pp. 57–82, 2019.

[44] B. H. Abed-Alguni, "A hybrid swarm algorithm for collective construction of 3D structures," *Int. J. Artif. Intell.*, vol. 18, no. 1, pp. 1–18, 2020.

[45] R.-E. Precup, R.-C. David, E. M. Petriu, A.-I. Szedlak-Stinean, and C.-A. Bojan-Dragos, "Grey wolf optimizer-based approach to the tuning of pi-fuzzy controllers with a reduced process parametric sensitivity," *IFAC-PapersOnLine*, vol. 49, no. 5, pp. 55–60, 2016.

[46] M. J. D. Powell, "A fast algorithm for nonlinearly constrained optimization calculations," in *Numerical Analysis* (Lecture Notes in Mathematics), vol. 630. G. A. Watson, Ed. Springer-Verlag, 1978.

[47] S. Koziel and L. Leifsson, *Simulation-Driven Design by Knowledge-Based Response Correction Techniques*. New York, NY, USA: Springer, 2016.

[48] S. Koziel, J. Bandler, A. Mohamed, and K. Madsen, "Enhanced surrogate models for statistical design exploiting space mapping technology," in *IEEE MTTS Int. Microw. Symp. Dig.*, Long Beach, CA, USA, Jun. 2005, pp. 1–4.

[49] S. Koziel and S. Szczepanski, "Accurate modeling of microwave structures using shape-preserving response prediction," *IET Microw. Antennas. Propag.*, vol. 5, no. 9, pp. 1116–1122, Jun. 2011.

[50] S. Koziel and S. D. Unnsteinsson, "Expedited design closure of antennas by means of trust-region-based adaptive response scaling," *IEEE Antennas Wireless Propag. Lett.*, vol. 17, no. 6, pp. 1099–1103, Jun. 2018.

[51] C. A. Balanis, *Antenna Theory: Analysis and Design*, 3rd ed. Hoboken, NJ, USA: Wiley, 2005.

[52] A. Y. Modi, M. A. Alyahya, C. A. Balanis, and C. R. Birtcher, "Metasurface-based method for broadband RCS reduction of dihedral corner reflectors with multiple bounces," *IEEE Trans. Antennas Propag.*, vol. 68, no. 3, pp. 1436–1447, Mar. 2020.

[53] M. Mighani and G. Dadashzadeh, "Broadband RCS reduction using a novel double layer chessboard AMC surface," *Electron. Lett.*, vol. 52, no. 14, pp. 1253–1255, Jul. 2016.
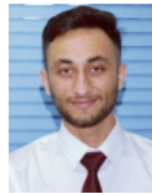
MUHAMMAD ABDULLAH received the B.Sc. degree from the University of Engineering and Technology, Pakistan, in 2016, and the M.Sc. degree from Xi'an Jiaotong University (XJTU), China, in 2019. From 2018 to 2019, he was with the Electromagnetics and Communication Laboratory, XJTU. Since late 2019, he has been associated with the Department of Engineering, Reykjavik University, Iceland, as a Researcher. His broader research interests include surrogate-based modeling and optimization, CAD and modeling of antennas and other high-frequency structures, simulation-driven design, machine-learning techniques, and millimeter-wave communication. On completion of the M.Sc. degree, he received the Excellent Master's Thesis Award.

SLAWOMIR KOZIEL (Senior Member, IEEE) received the M.Sc. and Ph.D. degrees in electronic engineering from the Gdańsk University of Technology, Poland, in 1995 and 2000, respectively, the M.Sc. degrees in theoretical physics and in mathematics, in 2000 and 2002, respectively, and the Ph.D. degree in mathematics from the University of Gdańsk, Poland, in 2003. He is currently a Professor with the Department of Engineering, Reykjavik University, Iceland. His research interests include CAD and modeling of microwave and antenna structures, simulation-driven design, surrogate-based optimization, space mapping, circuit theory, analog signal processing, evolutionary computation, and numerical analysis.

• • •

Chapter 4

4   Paper # 2

Slawomir Koziel and Muhammad Abdullah

Machine-Learning-Powered EM-Based Framework for Efficient and Reliable Design of Low Scattering Metasurfaces

Machine-Learning-Powered EM-Based Framework for Efficient and Reliable Design of Low Scattering Metasurfaces

Slawomir Koziel[ID], *Senior, Member, IEEE*, and Muhammad Abdullah[ID]

Abstract—Popularity of metasurfaces has been continuously growing due to their attractive properties including the ability to effectively manipulate electromagnetic (EM) waves. Metasurfaces comprise optimized geometries of unit cells arranged as a periodic lattice to obtain a desired EM response. One of their emerging application areas is the stealth technology, in particular, realization of radar cross section (RCS) reduction. Despite potential benefits, a practical obstacle hindering widespread metasurface utilization is the lack of systematic design procedures. Conventional approaches are largely intuition-inspired and demand heavy designer's interaction while exploring the parameter space and pursuing optimum unit cell geometries. Not surprisingly, these are unable to identify truly optimum solutions. In this article, we introduce a novel machine-learning-based framework for automated and computationally efficient design of metasurfaces realizing broadband RCS reduction. Our methodology is a three-stage procedure that involves global surrogate-assisted optimization of the unit cells, followed by their local refinement. The last stage is direct EM-driven maximization of the RCS reduction bandwidth, facilitated by appropriate formulation of the objective function involving regularization terms. The appealing feature of the proposed framework is that it optimizes the RCS reduction bandwidth directly at the level of the entire metasurface as opposed to merely optimizing unit cell geometries. Computational feasibility of the optimization process, especially its last stage, is ensured by high-quality initial designs rendered during the first two stages. To corroborate the utility of our procedure, it has been applied to several metasurface designs reported in the literature, leading to the RCS reduction bandwidth improvement by 15%–25% when compared with the original designs. Furthermore, it was used to design a novel metasurface featuring over 100% of relative bandwidth. Although the procedure has been used in the context of RCS design, it can be generalized to handle metasurface development for other application areas.

Index Terms—Metasurface, machine learning, electromagnetic (EM)-driven design optimization, radar cross section (RCS), scattering manipulation.

I. INTRODUCTION

METASURFACES are planar patterned surfaces composed of subwavelength periodic arrays of unit cells [1]. Within the past decade, their unique ability to manipulate the wavefront fostered utilization in many important applications, for example, beam-switching antennas, polarization converters, invisibility cloaks, gradient index lenses, holograms, stealth technology, and many others [2]–[6]. In the stealth technology, the main bottleneck is to reduce the radar cross section (RCS) to avoid detection by the enemy's radar. This can be accomplished by minimizing the backscattered electromagnetic (EM) energy from the metallic objects [7]. Some of the techniques implemented to accomplish RCS reduction include object reshaping method [8], invisibility cloaking [9], using radar absorbing materials (RAMs) [10], and active and passive cancellation [9]. Nevertheless, the downsides of the aforesaid techniques are narrow RCS reduction bandwidth, structural complexity, and severe losses.

An alternative approach to reduce the backscattered EM energy is to replace the conventional metallic surface with artificially engineered materials (metamaterials). The two prominent design strategies in this regard are to use metamaterials as an absorber [11]–[14] or to exploit their distinctive property of manipulating the phase reflection characteristics. In the former case, the incident EM energy transforms into heat; hence, backscattering energy can be diminished. Notwithstanding, the RCS reduction bandwidth still remains limited. The latter involves a periodic combination of artificial magnetic conductors (AMCs), and perfect electric conductors (PECs), arranged to attain the desired phase reflection characteristics. Two types of structures have been proposed that capitalize on this concept, that is, the EM gradient surface (EGS) [15] and the checkerboard metasurface [6]. In EGS, the metallic portion of the surface is substituted by the periodic arrays of AMC and PEC cells. When the plane wave is incident from the normal direction, the backscattered energy is tilted from that direction, thereby reducing the RCS. The fundamental condition in EGS is to maintain equal phase difference between the AMC and PEC unit cells [16]. The nonlinear relationship between the phase reflection characteristics and

frequency poses considerable challenges in satisfying the equal phase difference requirement over a wide frequency band. In the case of a checkerboard metasurface, the AMC and PEC cells are organized in an alternate fashion, and the objective is to maintain 180° phase difference between the AMC and PEC cells. By doing so, the incident EM energy scatters at four lobes in the diagonal plane [17], leading to low scattering property of the surface. The main advantages of the aforementioned surfaces include structural simplicity, robustness, and low profile [18]. However, the AMC structure exhibits relatively narrowband characteristics; outside the operating bandwidth, it starts resembling PEC. Consequently, the 180° phase difference condition no longer holds. To tackle this situation, de Cos *et al.* [19], [20] suggested utilization of two AMC cells instead of one to realize a dual resonance structure [21], [22]. The PEC unit cells are replaced by an additional AMC cell operating at a different resonant frequency. When exploiting such a structure to accomplish RCS reduction over a broad frequency band, the phase difference between the two AMC cells should remain 180° while retaining their reflection amplitudes identical and equal to 1 [17], [23]. In other words, the phase reflection curves of a pair of unit cells should remain equidistant over the frequency band where RCS reduction is to be achieved. Due to the presence of ohmic and tangent losses, the reflection amplitudes of the combined unit cells are not precisely the same. Therefore, it has been established that −10-dB RCS reduction can be maintained over a frequency band if the phase difference between the two AMC cells remains within the 143°–217° range (i.e., 180°± 37°) [24]. More recently, the concepts of coding metasurfaces [25], diffusion metasurfaces [26], [27], programmable metasurfaces [30], Huygens' metasurfaces [31], and cloaking structures [32] have been proposed, which offer a control over the wavefront in a more sophisticated manner. The primary advantage of coding and diffusion metasurfaces over the checkerboard type surfaces is that it scatters the incident EM waves into all directions. In addition, coding metasurfaces are also being exploited as an absorptive surface to realize essential RCS reduction [33].

To date, many metasurface architectures have been proposed to accomplish wideband RCS reduction [17], [19]–[29]. Due to the lack of reliable theoretical models, the conventional design methodologies mostly rely on empirical reasoning, physical intuition, or trial and error. Additionally, a considerable involvement of human interaction makes such methods laborious and time-consuming, also because full-wave EM simulations have to be used to evaluate metasurface characteristics in a reliable manner. Altogether, the aforementioned downsides pose serious questions concerning the efficacy of experience-driven methods, and their capability of finding truly optimum designs. Considering the practical design measures, the problem is additionally exacerbated by highly nonlinear input–output relationships. Efficient development of high-performance metasurfaces requires a new algorithmic framework that goes beyond interactive approaches and permits design automation, reliability, and computational efficiency. At this point, it should be mentioned that unprecedented advancements in computing hardware and software considerably increased the popularity and widespread use of rigorous

EM-driven design methodologies, primarily based on numerical optimization [34]. However, direct EM optimization of metasurface designs when using conventional algorithms may be prohibitively expensive, especially when global search is required. A practical workaround is utilization of machine learning methods [35]–[39], including surrogate modeling techniques [41]–[44]. Shifting the computational burden to a cheaper representation of the structure at hand and the incorporation of other means such as problem decomposition [45] may expedite the parameter tuning process and enable globalized search, otherwise infeasible when operating directly on EM simulation models. At this point, it should be mentioned that more generic approaches are also possible, where parametric optimization of the unit cells (and the metasurface) of a fixed geometry is replaced by topology optimization. In this case, the entire geometry of the metasurface is subject to the optimization process, which brings in additional degrees of freedom. This type of tasks is often handled using inverse modeling methods (see [46], [47]).

This article describes a rigorous machine-learning-based framework for efficient EM-driven design of low scattering metasurfaces. Its basic components include surrogate modeling of AMC cells and their concurrent optimization using a combination of global search and local refinement, as well as direct local tuning of the entire metasurface. Utilization of surrogate models allows for expediting the process of parameter adjustment that aims at broadening the frequency range for which the phase difference between two AMC cells remains within the 143°–217° range. Having optimum unit cell geometries, further EM-driven tuning of the cell parameters is carried out at the level of the entire checkerboard metasurface. The process is fast due to the availability of a good initial design produced at the earlier stages, as well as utilization of trust-region (TR) gradient algorithm with sparse sensitivity updates [45]. Moreover, a regularization approach is used to efficiently handle frequency-localized violations of the RCS reduction threshold that occur while enhancing the overall reduction bandwidth. To calculate the RCS reduction bandwidth of a metasurface, a PEC surface of a similar size is implemented to be used as a reference surface. In this study, we considered checkerboard metasurfaces to demonstrate the utility our framework; nevertheless, the introduced design optimization methodology is not limited to this particular class of structures. The presented procedure is generic and can be applied to any type of metasurface architecture. At the same time, it should be emphasized that the proposed optimization procedure addresses the problem of parameter adjustments of unit cells and metasurfaces of fixed geometry. Topology optimization is outside the scope of this work.

The presented framework addresses the key challenges of metasurface design as elaborated on earlier in this section. It enables fully automated and optimum design within the assumed parameter space. The design methodology is validated both numerically and experimentally. The technical novelty and major contributions of this article can be summarized as follows: 1) the development of machine-learning-powered framework for reliable and efficient EM-based optimization of checkerboard metasurfaces; 2) demonstrating the practical

utility of our approach in the context of broadband meta-surface design using three application examples; and 3) the development of a high-performance checkerboard metasurface featuring over 100% relative RCS reduction bandwidth. To the authors' knowledge, the proposed framework is the first systematic procedure proposed in the literature for globally optimum design of low scattering checkerboard metasurfaces.

The remaining part of the article is organized as follows. In Section II, we formulate the metamodeling-based procedure for concurrent optimization of the pairs of unit cell geometries. Subsequently, a regularization-based formulation of the metasurface design problem is provided for broadband RCS reduction, followed by a complete optimization procedure. In Section III, we demonstrate the performance of the proposed procedure using three benchmark examples. Section IV provides experimental validation of the metasurface design featuring over 100% RCS reduction bandwidth. Section V concludes the article.

II. Machine-Learning-Powered EM-Based Metasurface Design

This section provides a comprehensive description of the proposed machine-learning-powered EM-driven design procedure. We start by presenting the metamodel-based procedure for concurrent optimization of the pairs of unit cells for required reflection phase characteristics. Subsequently, a regularization-based formulation of the metasurface design problem is provided for broadband RCS reduction. The section is concluded with a summary of a complete optimization procedure. Application of the proposed framework to low scattering metasurface design will be provided in Section III.

A. Concurrent Unit Cell Optimization by Machine Learning

The purpose of the machine-learning-based optimization procedure is to find a pair of unit cell designs featuring the phase difference within the range of $180° \pm \alpha_{\max}$ over a possibly broad frequency range F. Here, $\alpha_{\max}$ is set to $37°$, as suggested in [24]. The vectors of designable variables for a pair of unit cells will be denoted as $x_1 = [x_{1.1}...x_{1.n}]^T \in X_1$ and $x_2 = [x_{2.1}...x_{2.n}]^T \in X_2$, and their EM simulated responses will be represented by $P_1(x)$ and $P_2(x)$, respectively. The latter denotes the phase reflection characteristics. The parameter space X_i is determined by the user-defined lower and upper bounds $l_i = [l_{i.1}...l_{i.n}]^T$ and $u_i = [u_{i.1}...u_{i.n}]^T$ so that $l_{i.l} \leq x_{i.l} \leq u_{i.l}$, $l = 1,...,n$ and $i = 1, 2$. Notwithstanding, in many practical cases, the topology and hence the vector of designable variables for the two unit cells is identical.

Initially, the acquisition of the training data is carried out by uniformly allocating N samples within the parameter spaces, X_1 and X_2, and evaluating the EM simulation model to obtain the corresponding responses. Subsequently, the metamodels S_1 and S_2 are constructed within X_1 and X_2 using kriging interpolation [40], [41]. The model is trained using the data samples $\{x_i^{(k)}, P_i(x_i^{(k)})\}_{k=1,...,Ni}$, where $P_i(x_i^{(k)})$ and N_i denotes the EM-simulated response of the kth design and the total number of training samples for the ith unit cell, respectively. The data samples are arranged on a rectangular grid, which is a suitable

design of experiment strategy for a low-dimensional case. The allocation of the grid nodes in each direction is decided based on the large-scale sensitivity analysis.

Kriging is a Gaussian process-based modeling technique [40] widely used for constructing interpolating surrogates in a broad range of applications. For the convenience of the reader, a brief outline of the technique is provided below assuming scalar output. Generalization for vector-valued functions is straightforward. The function of interest is assumed to be of the form

$$f(x) = g(x)^T \beta + Z(x) \qquad (1)$$

where $g(x) = [g_1(x) \ g_2(x)...g_N(x)]^T$ are known (here, EM-simulated) system responses, $\beta = [\beta_1 \beta_2 ... \beta_N]^T$ are the unknown hyperparameters, and $Z(x)$ is a realization of a normally distributed Gaussian random process with zero mean and variance σ^2. The regression component $g(x)^T \beta$ serves as a trend function for f, whereas $Z(x)$ manages localized variations from the trend. The covariance matrix of $Z(x)$ is

$$Cov[Z(x^{(i)})Z(x^{(j)})] = \sigma^2 R([R(x^{(i)}, x^{(j)})]) \qquad (2)$$

where R is a $p \times p$ correlation matrix with $R_{ij} = R(x^{(i)}, x^{(j)})$, and $R(x^{(i)}, x^{(j)})$ is the correlation function between data samples $x^{(i)}$ and $x^{(j)}$. Here, we use a Gaussian correlation function of the form

$$R(x, y) = \exp\left[-\sum_{k=1}^{n} \theta_k |x_k - y_k|^2\right] \qquad (3)$$

where θ_k are the unknown correlation parameters, and x_k and y_k are the kth elements of the vectors x and y, respectively. The kriging model is defined as [40]

$$s(x) = g(x)^T \beta + r^T(x) R^{-1}(h - G\beta) \qquad (4)$$

where

$$r(x) = [R(x, x^{(1)}) \ldots R(x, x^{(p)})] \qquad (5)$$

$$f = [f(x^{(1)}) f(x^{(2)}) \ldots f(x^{(p)})]^T \qquad (6)$$

and G is a $p \times N$ matrix with $G_{ij} = P_j(x^{(i)})$. The vector of model parameters β can be computed as

$$\beta = (G^T R^{-1} G)^{-1} G^T R^{-1} f. \qquad (7)$$

Finally, model fitting is accomplished by maximum likelihood scheme for θ_k

$$-[p \ln(\sigma^2) + \ln|R|]/2. \qquad (8)$$

Here, both σ^2 and R are the functions of θ_k. The components of the vector-valued metamodels S_1 and S_2 of the phase characteristics P_1 and P_2, respectively, are the kriging interpolation surrogates rendered for phase responses at all individual frequencies in the considered frequency sweep.

Having the trained metamodels S_1 and S_2, the concurrent unit cell optimization is carried out over the joint parameter space of the pair of cells, that is, the Cartesian product $X_1 \times X_2$. The goal of the optimization procedure is to find a pair of unit cell designs $x_p^* = [(x_1^*)^T (x_2^*)^T]^T$ maximizing the frequency

range for which the phase difference between the two satisfies the condition

$$180° - a_{max} \leq \Delta P\left(\left[(x_1^*)^T (x_2^*)^T\right]^T\right) \leq 180° + a_{max}. \quad (9)$$

Specifically, the design task can be formulated as follows:

$$x_p^* = \arg \min_{x_p \in X_1 \times X_2} U(\Delta P(x_p)) \quad (10)$$

and the objective function U is defined as

$$U(\Delta P(x_p)) = -\left[f_R(x_p) - f_L(x_p)\right] \quad (11)$$

where f_L and f_R are the frequencies defining the largest continuous frequency range for which condition (9) is satisfied. The minus sign in (11) turns the maximization task into the minimization one.

Global optimization is performed based on a structured grid (in an exhaustive manner). Let $M_{m1...mn}$ be a rectangular grid such that $x_i \in M_{i.m1...mn}$ if and only if $x_i = [x_{i.1}...x_{i.n}]^T$ is of the form $x_{i.k} = l_{i.k} + j_{i.k}[(u_{i.k}-l_{i.k})/m_{i.k}]$, $k = 1,..., n$, and $i = 1, 2$, where $m_{i.k}$ is a grid-defining integer for the kth variable of ith unit cell, and $j_{i.k} \in \{0, 1,..., m_{i.k}\}$. The initial approximation $x_p^{(0)}$ of the global optimum of S_1 and S_2 is found as

$$x_p^{(0)} = \arg \min_{\substack{x_1 \in M_{1.m_1...m_n} \\ x_2 \in M_{2.m_1...m_n}}} U(\Delta P([(x_1)^T (x_2)^T])). \quad (12)$$

In other words, $x_p^{(0)}$ is obtained by exploring all possible combinations of unit cell designs $x_1 \in M_{1.m1...mn}$ and $x_2 \in M_{2.m1...mn}$ and identifying the one that minimizes U. After determining $x_p^{(0)}$, the local refinement is executed using gradient-based search [48]. The computational cost of the global and local optimization process is negligible because it is executed at the level of the fast kriging metamodels S_1 and S_2. Additionally, the complete procedure is implemented in a vectorized manner to further speed-up its operation. Clearly, there is an initial cost associated with the acquisition of the training data for surrogate model construction. The latter is unavoidable to render the aforementioned computational benefits and to enable global search in the first place. The details concerning the acquisition cost are provided in Section III in the context of specific verification examples considered therein.

B. EM-Driven Metasurface Refinement for RCS Reduction Bandwidth Enhancement

Upon adjusting the unit cell parameters as described in Section II-A, EM-driven refinement of the entire metasurface is carried out. This stage is necessary because optimized dimensions of the cells do not translate into optimum design of the entire structure; recall that the unit cells were tuned to satisfy the phase condition (9). To obtain the best possible performance, the enhancement of the RCS bandwidth has to be performed directly.

Let x_A denote the aggregated $(n_1 + n_2) \times 1$ geometrical parameter vector of the pair of the unit cells. Furthermore, let $R_{red}(x_A, f)$ represent the frequency characteristics representing the RCS reduction, that is, the difference between the
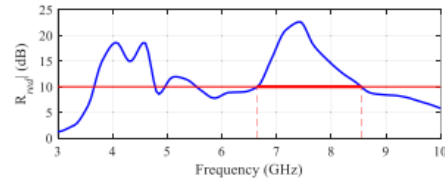

Fig. 1. Exemplary RCS reduction characteristics with the RCS bandwidth marked using the thick horizontal line and representing the largest (continuous) frequency range satisfying the condition $R_{red}(x_A, f) \geq r_{max}$; here, $r_{max} = 10$ dB.
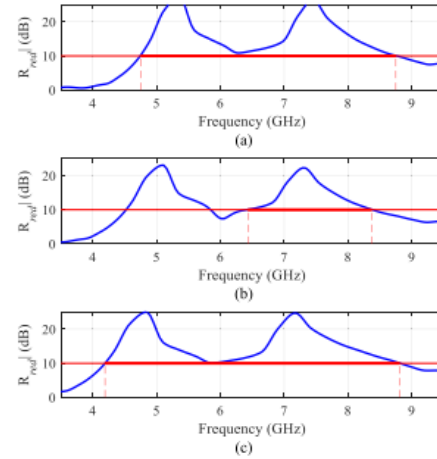

Fig. 2. Practical issues related to conventional RCS bandwidth reduction definition. The sequence of plots from (a) to (c) indicates RCS characteristics at (a) initial design, (b) intermediate design, and (c) optimum design featuring the largest bandwidth. Because the intermediate design exhibits violation of the r_{max} threshold, the bandwidth at this design is significantly smaller than around the initial design and the optimum design. In other words, a discontinuity occurs, which can make the optimum design unattainable from the given initial design when using local optimization routine (the only practical option for direct EM-driven metasurface design).

monostatic RCS of a reference (metallic) surface and that of the considered metasurface, where f stands for the frequency. Conventionally, the RCS reduction bandwidth B_{RCS} to be maximized is defined as the broadest continuous frequency range satisfying the condition $R_{red}(x_A, f) \geq r_{max}$, where r_{max} stands for the acceptance threshold (e.g., 6 or 10 dB).

This is illustrated in Fig. 1. The problem with this definition has been indicated in Fig. 2. If the initial and the optimum design are separated by the designs that violate the acceptance threshold r_{max} [see Fig. 2(b)], a discontinuity of the bandwidth value will be observed along the path connecting the two designs, which essentially prevents local (e.g., gradient-based) optimization algorithm from reaching the optimum.

The latter is the only practical option for direct EM-driven metasurface tuning due to high costs incurred by structure evaluation. On the other hand, a situation as illustrated in Fig. 2
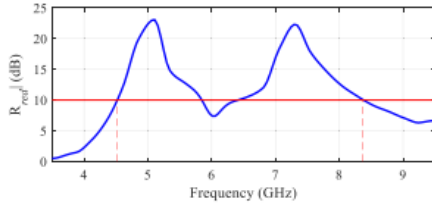
Fig. 3. Exemplary RCS characteristic with the lower frequency f_L, upper frequency f_H, and r_{max} violation d_r marked to indicate the defining quantities of the objective function for RCS reduction bandwidth improvement.

is a commonplace because the optimum design would often correspond to the RCS characteristics almost violating the threshold at certain frequencies [see Fig. 2(c)]. Consequently, an efficient adjustment of metasurface parameters needs a different formulation of the objective function.

Consider Fig. 3, where the frequencies f_L and f_H stand for the minimum and the maximum frequencies (within the considered simulation range) for which the condition $R_{red}(x_A, f) \geq r_{max}$ is satisfied. Let d_r stand for the maximum violation of the above condition within the frequency interval $[f_L \ f_H]$. Using these, the objective function U_{RCS} for metasuface tuning will be defined as

$$U_{RCS}(x_A) = -[f_H(x_A) - f_L(x_A)] + \beta c_r(x_A)^2. \quad (13)$$

The first term in (5) is the negative RCS reduction bandwidth (to turn the task into a minimization problem). The second component is a regularization term with the function c_r defined as $c_r(x_A) = d_r$ if $d_r > 0$ and zero otherwise. Its purpose is to increase the objective function if violation of the acceptance threshold is detected.

The contribution of the regularization term is controlled by coefficient β. Here, it is set to $\beta = 1$, but this value is not critical. Nevertheless, it can be used to control the amount of violation that can be tolerated.

The most important advantage of formulation (13) is that it effectively alleviates the difficulty related to conventional formulation. In particular, the objective function does not exhibit discontinuities related to in-band violation of the acceptance threshold, which makes the optimum design attainable through local search for situations depicted in Fig. 2.

The optimization process is realized using the TR gradient search algorithm [48], [50]. The parameter tuning task is formulated as

$$x_A^* = \arg \min_{x_A \in X_1 \times X_2} U_{RCS}(x_A). \quad (14)$$

The TR algorithm renders a series of approximations $x_A^{(j)}$, $j = 0, 1, \ldots,$ to x_A^* as

$$x_A^{(j+1)} = \arg \min_{\substack{x \in X_1 \times X_2 \\ x_A^{(j)} - d^{(j)} \leq x_A \leq x_A^{(j)} - d^{(j)}}} L_{RCS}^{(j)}(x_A) \quad (15)$$

where $L_{RCS}^{(j)}$ is the objective function of the form of (13) but computed from the first-order Taylor expansion model of $R_{red}(x_A, f)$ established at the current iteration point $x_A^{(j)}$.

The construction of the Taylor model requires the knowledge of the Jacobian matrix of R_{red}, which is estimated using finite differentiation in the first iteration and then updated by the adaptive application of the rank-one Broyden formula [45]. Using this approach, the tuning process can be realized at a low computational cost, typically about $M \cdot n$ of EM simulations of the metasurface, where n is the number of geometrical parameters, and $M = 3$–4. The TR size vector $d^{(j)}$ is adjusted by means of the standard TR rules [48].

C. Optimization Framework

The algorithm starts by defining the lower and upper bounds to determine the parameter spaces X_i and allocating N_i samples. The rectangular grids M_i (see Section II-A) are established by investigating the large-scale sensitivities of the unit cell responses to their geometrical parameters. The training data are obtained by evaluating the EM simulation model at the assigned locations. In the next step, the kriging metamodels S_1 and S_2 are constructed and used as predictors of a unit cell reflection phase characteristics over the spaces X_i. The concurrent unit cell optimization is then carried out to find a pair of cell designs featuring the phase difference within a particular range.

The first stage of this process is a global search (4), followed by local (gradient-based) tuning. Having the optimum pair of unit cells, their periodic arrays are used in an alternate manner to characterize a checkerboard metasurface. Finally, EM-driven fine tuning of the cell parameters is carried out at the level of the entire surface. This stage follows the procedure described in detail in Section II-B.

The proposed framework enables expedited and efficient development of high-performance metasurfaces featuring broadband RCS reduction characteristics. The flow diagram of the machine-learning-powered EM-based design framework has been shown in Fig. 4, whereas Fig. 5 shows the flow diagram of the local tuning procedure.

III. APPLICATION EXAMPLES

This section presents the operation and performance of the machine-learning-powered EM-based design procedure using three application case studies. We start by applying the proposed framework to a geometrically simple structure. This example is also used to explain and emphasize the importance of various components of the algorithmic procedure. Subsequently, two more cases are considered featuring more complex unit cell geometries. The obtained RCS reduction bandwidths are compared with those reported in the source article. A discussion of the results and various aspects of the presented framework is also provided in the last part of this section. The experimental validation of one of the considered metasurfaces will be discussed in Section IV.

A. Case 1: Checkerboard EBG Surface Utilizing Rectangular and Circular Cell Topologies

Our first application example is a checkerboard surface consisting of a rectangular and circular shape unit cells. The
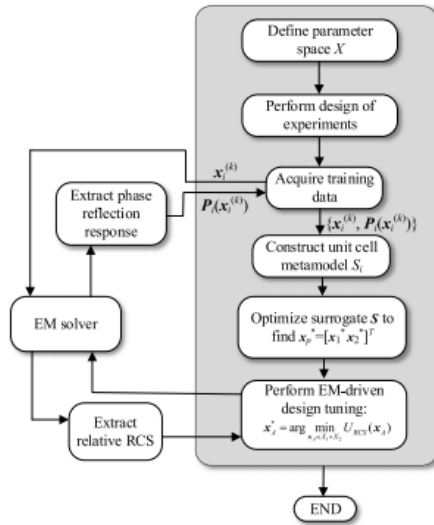
Fig. 4. Flow diagram of the proposed machine-learning-powered EM-based framework for developing low scattering metasurfaces.
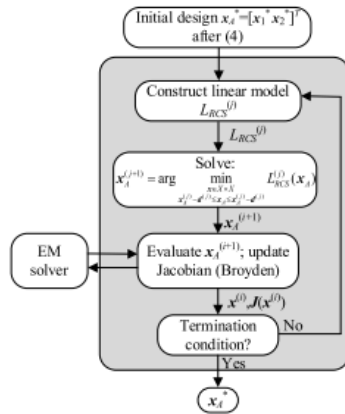

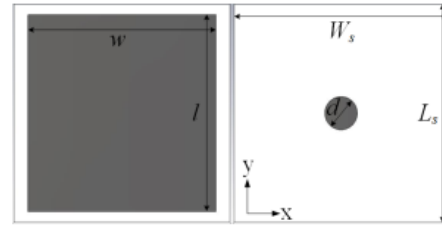Fig. 5. Flow diagram of the EM-based local refinement stage.

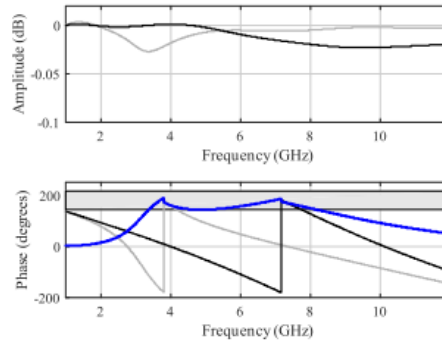Fig. 6. Geometries of the optimized unit cell designs: Cell 1 (left), and Cell 2 (right).

Fig. 7. Reflection performance of the optimized unit cells: reflection amplitude (top) and reflection phase (bottom). The responses of Cell 1 and Cell 2 are marked gray and black, respectively, whereas the blue curve indicates the reflection phase difference. The gray-shaded area in the bottom plot indicates the range of acceptable phase differences.
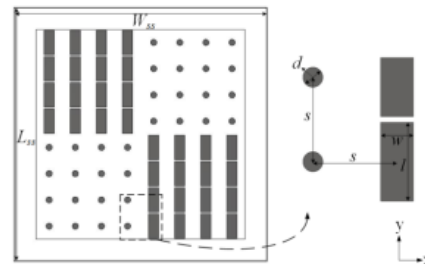

Fig. 8. Geometry configuration of the optimized metasurface (after three-stage optimization procedure).

cell geometries and the entire surface configuration are shown in Figs. 6 and 8, respectively. The structure is based on a design proposed in [23]. It is implemented on a ground-backed Rogers RT/duroid 5880 lossy substrate (ε_r = 2.2, h = 6.35 mm, tanδ = 0.0009). During the simulations, metallization is represented as perfect electrical conductor (PEC). The overall size of a single unit cell is $W_s \times L_s$ = 15 × 15 mm². As shown in Fig. 6, there are two geometrical parameters l and w, for Cell 1, and one parameter d for Cell 2 that control the design topology of a corresponding unit cell.

Hence, the vectors of designable variables are $x_1 = [l w]^T$ and $x_2 = [d]^T$; L_s, W_s, W_{ss}, L_{ss}, and s are all fixed. The sample spaces X_1 and X_2 are defined by the lower and upper bounds as: $l_1 = [12\ 12]^T$, $u_1 = [14.9\ 14.9]^T$, and $l_2 = 1$, $u_2 = 5$; all dimensions are in millimeters.

For constructing metamodels S_1 and S_2, the training points are arranged in a uniform grid $M_{14.14}$ and M_{100} (see Section II-A) with a total of 196 and 100 samples in the sample

spaces X_1 and X_2, respectively. A joint parameter space is the Cartesian product $X_1 \times X_2$. The acquired data are divided into the training (85%) and the test data (15%) to be used for split-sample error estimation. The frequency-domain solver of the CST Microwave Studio is used to evaluate the phase reflection responses of the unit cell.

The trained metamodels have been used at the concurrent unit cell optimization stages (procedure of Section II-A) to find the pair of designs, and the optimal geometries obtained in the process are $x_1^* = [13.5263, 13.0684]^T$ and $x_2^* = 2.2814$. Their topologies are shown in Fig. 6, and the EM-simulated reflection response along with the reflection phase difference between the two cells are presented in Fig. 7. It can be observed that condition (1) is satisfied for the continuous range of frequencies from 3.6 to 8.2 GHz, and hence the latter can be anticipated as the approximate RCS reduction bandwidth of the entire metasurface.

Having the optimal pair of unit cell designs, their periodic arrays are implemented in an alternate manner to characterize a 2 × 2 checkerboard metasurface; see Fig. 8. Each lattice of a periodic surface comprises 16 elements, that is, 4 × 4 planar array of Cell 1 or Cell 2. The total size of the surface is $W_{ss} \times L_{ss} = 120 \times 120$ mm^2. The interelement spacing of individual unit cells in an array is $s = 15$ mm. Again, the surface is implemented on a Rogers RT/duroid 5880 lossy substrate. To characterize the RCS reduction performance, a PEC surface of a similar size is also used. Hereafter, the EM-driven approach (see Section II-B) is adopted to fine-tune the RCS reduction bandwidth in the vicinity of the optimal cell geometries, following their surrogate-assisted global optimization and local refinement. To this end, the time-domain solver of CST Microwave Studio, MATLAB R2018a, and MATLAB-to-CST socket (for communication with the EM solver) is used.

To obtain the best possible performance, the optimization of the RCS reduction bandwidth has to be performed at the level of the entire metasurface. The availability of a good starting point, identified earlier, is critical to ensure reliability of the tuning process. In particular, it makes the utilization of the gradient-based algorithm sufficient to find a global optimum with a high likelihood. This is due to optimizing the unit cells in a global sense and the fact that the properties of the phase difference characteristics are good estimators of the RCS reduction bandwidth at the metasurface level. At the same time, utilization of the local optimization algorithm with its low computational cost is the only practical option when optimizing the EM model of the entire structure.

The optimum design obtained after the completion of the procedure given in Section II-B is $x_A^* = [13.952, 5.824, 3.151]^T$. To corroborate the utility of a proposed design framework in the context of broadband RCS reduction, the monostatic RCS performance for the normal incidence has been determined. For the sake of comparison, the RCS performance reported in [23], the RCS reduction bandwidth obtained after designing the surface based on the optimum geometries identified after the procedure of Section II-A, and the final RCS characteristic upon accomplishing the metasurface optimization are all gathered in Fig. 9. It can be observed that
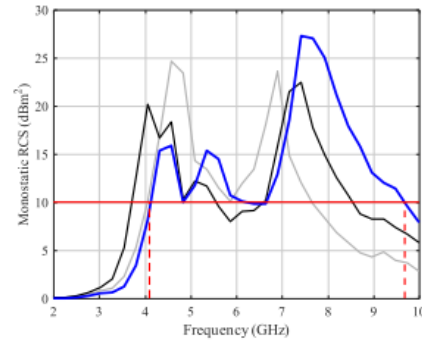

Fig. 9. Monostatic RCS performance of the metasurface design reported in [23] (gray), performance after the first and the second optimization stages (Section II-A) (black), and the performance of the final design (Section II-B) (blue). The horizontal red line represents the 10-dB RCS reduction threshold relative to the PEC surface.

the machine-learning-based concurrent unit cell optimization considerably increases the bandwidth compared with the conventional design approach. The EM-driven optimization of the entire structure further extends the RCS reduction bandwidth. It should be noted that the violation of the 10-dB threshold occurring at certain frequencies upon metamodeling-assisted cell optimization is efficiently handled by the TR algorithm. The 10-dB RCS reduction bandwidth at the final design extends from 4.1 to 9.7 GHz. This result corroborates the importance of EM-driven optimization at the metasurface level and demonstrates the efficacy of the methodology proposed in this work. The computational cost of the first and the second stage (machine-learning-powered unit cell optimization) is negligible, whereas the cost of EM-driven refinement stage is 15 metasurface simulations.

Throughout this work, Intel Xeon E5540 dual-core machine with 18-GB RAM is used. The EM simulation model of the unit cell and the entire surface contains about 19 000 and 563 000 mesh cells, respectively. The simulation time of the unit cell and the metasurface is about 40 s and 2 min, respectively. The CPU time required for training data acquisition is about 3 h, whereas the time required for the refinement stage is 30 min. As mentioned before, the cost of global and local optimization of the unit cells (conducted at the level of the kriging surrogate) is negligible. Consequently, the overall CPU time of the entire design optimization procedure is about 3 h 30 min.

The bistatic RCS performance versus the elevation angle theta θ along the principal and the diagonal planes is shown in Fig. 10. The results demonstrate that the metasurface exhibits more than the 15-dB RCS reduction in the principal and the diagonal planes, compared with the metallic surface. This reduction occurs because the reflected fields are redirected into four main lobes, instead of the single main lobe in the case of the metallic surface.
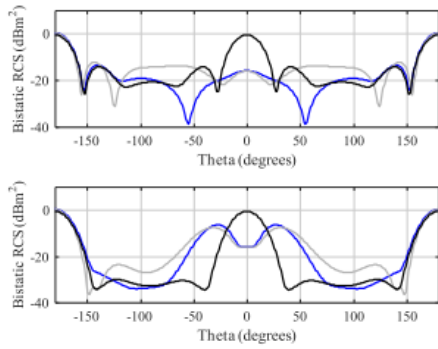
Fig. 10.   Bistatic RCS performance at 5.5 GHz along the principal planes (top) and along the diagonal planes (bottom). The curves corresponding to the two planes $\varphi = 0/45$ and $\varphi = 90/135$ are marked in blue and gray, respectively, whereas the black curve indicates the scattered field from the PEC surface.
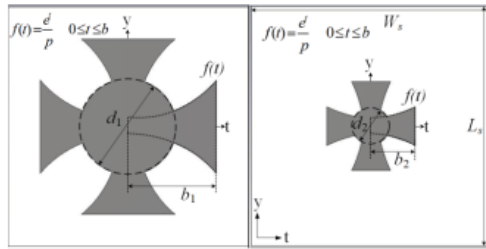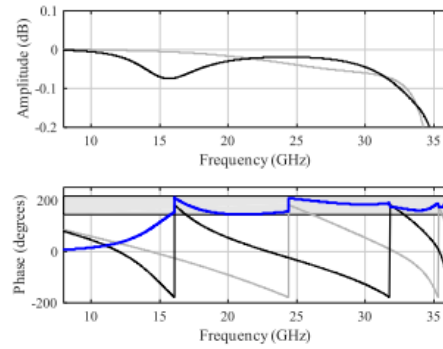

Fig. 12.   Reflection performance of the optimized unit cells: reflection amplitude (top) and reflection phase (bottom). The responses of Cell 1 and Cell 2 are marked in black and gray, respectively, whereas the blue curve indicates the reflection phase difference. The gray-shaded area in the bottom plot indicates the range of acceptable phase differences.
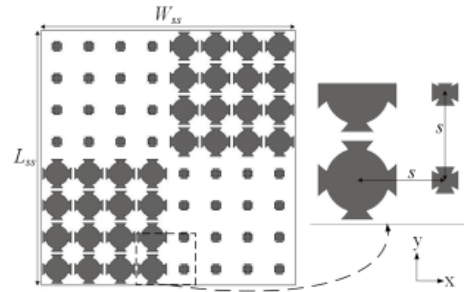

Fig. 11.   Geometries of the optimized unit cell designs (upon applying the procedure of Section II-A): Cell 1 (left) and Cell 2 (right).

Fig. 13.   Geometry configuration of the optimized metasurface (after three-stage optimization procedure).

B. Case 2: Checkerboard Metasurface Applying Mushroom-Like Cell Topologies

The second structure under consideration is more challenging in the sense of being based on more complex unit cell geometries described by a larger number of designable parameters. It is a checkerboard metasurface comprising mushroom-like unit cells; see Figs. 11 and 13. The structure is implemented on a ground-backed Arlon AD250 lossy substrate ($\varepsilon_r = 2.5$, $h = 1.5$ mm, $\tan\delta = 0.0018$). The overall size of a single unit cell is $W_s \times L_s = 6 \times 6$ mm^2. There are three geometrical parameters that determine the shape of each unit cell designs, that is, Cell 1 and Cell 2. Therefore, the two vectors of designable variables are $x_1 = [p_1 b_1 \ d_1]^T$ and $x_2 = [p_2 b_2 d_2]^T$; L_s, W_s, L_{ss}, W_{ss}, and s are all fixed. The parameter space $X_1 = X_2 = X$ is determined by the user-defined lower and upper bounds as: $l = [3.5 \ 0.3 \ 0.2]^T$, $u = [10 \ 1.6 \ 2.4]^T$; all dimensions are in millimeters. In this case study, the underlying topology of the two unit cells is the same, as opposed to the previous case study, where the two unit cells were based on entirely different structures.

For constructing a metamodel S, the training points are arranged in a uniform grid $M_{7.12.7}$ (see Section II-A) with a total of 588 samples in the space X. As mentioned earlier, the underlying topologies of both the cells are identical, and therefore, only a single metamodel is needed. Similarly as for the first example, the accumulated data are divided into the training (85%) and the test data (15%) to be used for split-sample error estimation. The frequency-domain solver of the CST Microwave Studio is used to evaluate the phase reflection responses of the unit cell.

Having a trained metamodel S, the concurrent unit cell adjustment is performed (see the procedure of Section II-A) to find a pair of optimum designs. The geometries obtained after completion of the surrogate-assisted global and local optimization are $x_1^* = [4.222, \ 1.600, \ 2.400]^T$ and $x_2^* = [4.944, \ 0.878, \ 0.930]^T$. The designs are shown in Fig. 11, whereas their EM-simulated reflection performance along with the reflection phase difference are presented in Fig. 12. The expected RCS reduction bandwidth that can be deduced from the phase reflection response is from 17 to above 35 GHz.

After finding the optimized pair of unit cells, the checkerboard metasurface is characterized following a similar proce-
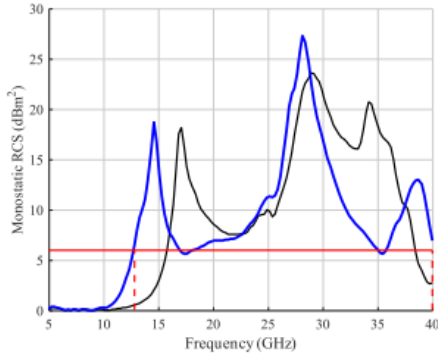
Fig. 14. Monostatic RCS of a metasurface after first and second optimization stages (see Section II-A) (black) and the RCS performance after the final stage (Section II-B) (blue). The horizontal red line represents the 6-dB RCS reduction threshold relative to the PEC surface.
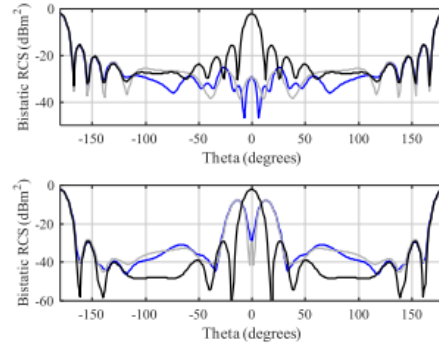

Fig. 15. Bistatic RCS performance at 25 GHz along the principal planes (top) and along the diagonal planes (bottom). The responses at the two planes corresponding to $\varphi = 0/45$ and $\varphi = 90/135$ are marked in blue and gray, respectively, whereas the black curve indicates the scattered field from the PEC surface.

dure as discussed for the first application example. The surface configuration is shown in Fig. 13. The total size of the surface is $W_{ss} \times L_{ss} = 48 \times 48$ mm^2. The interelement spacing of individual unit cells in an array is $s = 6$ mm. The surface is implemented on Arlon AD250 lossy substrate.

Again, the EM-driven local tuning is performed at this stage (see Section II-B). The design obtained at the final optimization stage is $\boldsymbol{x}_A^* = [4.492, 1.601, 4.296, 3.485, 0.795, 0.382]^T$. To quantify the performance of the proposed design framework, the RCS reduction bandwidth obtained when the metasurface is implemented using the cell designs identified by the procedure of Section II-A, and the reduction bandwidth obtained at the final design is demonstrated in Fig. 14.

It can be observed that the machine-learning-based cell optimization procedure already ensures a broadband RCS reduction performance. However, the performance is considerably improved after applying the EM-driven optimization. The 6-dB RCS reduction bandwidth extends from 13 to over 40 GHz. Owing to the implemented acceleration mechanisms, the cost of the final refinement stage is only 32 EM simulations of the metasurface.

In this case, the EM simulation model of the unit cell and the entire surface contains about 22 000, and 2 400 000 mesh cells, respectively. The corresponding simulation times are 70 s and 30 min, respectively. The CPU time required for training data acquisition is about 11 h, whereas the time required for the refinement stage is about 15 h. Consequently, the overall CPU time of the entire design optimization procedure is about 26 h.

Finally, the scattered field as a function of the elevation angle theta θ along the principal and the diagonal planes are presented in Fig. 15. The bistatic RCS performance of the metasurface is compared with the PEC surface of similar size. The results indicate that the metasurface offers nearly 20-dB RCS reduction in both the principal and the diagonal planes.
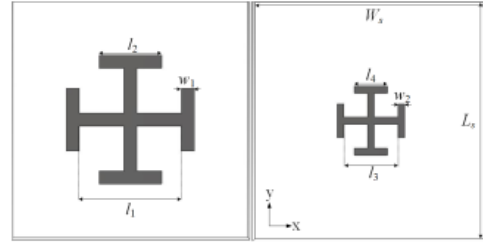

Fig. 16. Geometries of the optimized unit cell designs (as reported in [17]): Cell 1 (left) and Cell 2 (right).
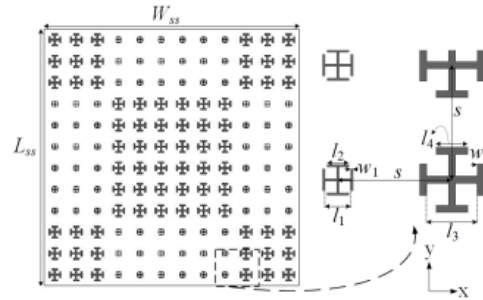

Fig. 17. Geometry configuration of the optimized metasurface (obtained using the optimization procedure of Section II-B).

C. Case 3: Metasurface Using Jerusalem Cross-Shaped Unit Cells

The final application example is based on a surface presented in [17]. It consists of a Jerusalem-cross-shaped unit cell topology. The unit cell geometries and the entire surface configuration are shown in Figs. 16 and 17, respectively. In
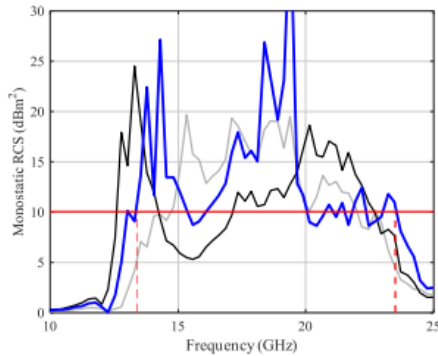
Fig. 18. Monostatic RCS performance of a metasurface design reported in [17] (gray) and after applying the proposed framework of Section II (blue). The horizontal red line represents the 10-dB RCS reduction threshold relative to the PEC surface.
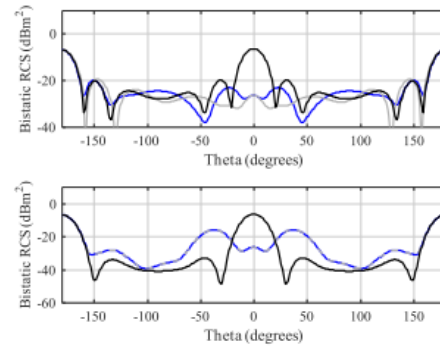

Fig. 19. Bistatic RCS performance at 17 GHz along the principal planes (top) and along the diagonal planes (bottom). The characteristics at the two planes corresponding to $\varphi = 0/45$ and $\varphi = 90/135$ are marked in blue and gray, respectively, whereas the black curve indicates the scattered field from the PEC surface.

this case, a ground-backed Rogers 3010 lossy substrate ($\varepsilon_r = 10.2$, $h = 1.27$ mm, $\tan\delta = 0.0022$) is used to design the individual unit cells and the complete metasurface. The size of a single unit cell is $W_s \times L_s = 4 \times 4$ mm^2. There are three geometrical parameters in both unit cells, and hence the two vectors of designable variables are $x_1 = [l_1 l_2 w_1]^T$ and $x_2 = [l_3 l_4 w_2]^T$; L_s, W_s, L_{ss}, W_{ss}, and s are all fixed. The sample space $X_1 = X_2 = X$ is determined by the lower and upper bounds as: $l = [0.5\ 0.2\ 0.1]^T$, $u = [2\ 1\ 0.3]^T$; all dimensions are in millimeters.

For constructing a surrogate S, the training points are arranged in a uniform grid $M_{9.9.7}$ with a total of 567 samples in the space X. Again, the accumulated data are divided into the training (85%) and the test data (15%) to be used for split-sample error estimation. As in the first and second examples, the concurrent unit cell optimization is performed to find a pair of designs. The optimal geometries obtained after completion of the surrogate-assisted global and local optimization are $x_1^* = [0.5408, 0.2704, 0.1769]^T$ and $x_2^* = [1.9694, 0.9847, 0.3]^T$.

The checkerboard metasurface is implemented using the optimum unit cell geometries; see Figs. 16 and 17. The overall size of the metasurface is $W_{ss} \times L_{ss} = 48 \times 48$ mm^2, and the intercell spacing is $s = 4$ mm. The EM-driven design optimization procedure is subsequently used in the final design $x_A^* = [0.668, 0.716, 0.201, 1.905, 0.902, 0.317]^T$. The cost of the final tuning stage is only 56 EM simulations of the metasurface. The monostatic RCS reduction performance as a function of frequency is presented in Fig. 18. As expected, the considerable threshold violations present after the first and the second optimization stages are greatly reduced at the final design.

In this case, the EM simulation model of the unit cell and the entire surface contains about 25 000 (simulation time 75 s) and 1 700 000 mesh cells (simulation time 33 min), respectively. The simulation time required by the training stage

TABLE I
DESIGN PERFORMANCE AT VARIOUS STAGES OF THE PROPOSED FRAMEWORK

Application Example	Fractional bandwidth (%)		
	Reported in the literature	After two-stage optimization	After EM-driven tuning
Case 1 [23]	61	70	80
Case 2	-	83	>104
Case 3 [17]	39	57*	56

*Fractional bandwidth including level violation at certain frequencies.

is approximately 12 h, and the total time required for entire design optimization procedure to complete is about 42 h.

Notwithstanding, a 10-dB RCS reduction threshold is still slightly violated at certain frequencies. Overall, the RCS bandwidth is extended by about 3 GHz when compared with the design reported in [17].

Fig. 19 shows the bistatic RCS performance versus the elevation angle theta θ along the principal and the diagonal planes. The results imply that the optimized metasurface features more than the 15-dB RCS reduction in the principal and the diagonal planes, compared with the PEC surface.

D. Discussion

The breakdown of the results obtained at different stages of the proposed design optimization framework is provided in Table I. It can be observed that for the first verification case, the machine-learning-assisted unit cell optimization itself yields 9% enhancement of the fractional RCS reduction bandwidth when compared with the previously reported results, based on the traditional design methods. The EM-driven fine-tuning leads to additional 10% improvement. In the second application example, the improvement is as high as over 21% due to EM-based tuning of the metasurface. Note that the

Fig. 20. Photograph of the prototyped checkerboard metasurface.

Fig. 21. Block diagram of the measurement environment.

absence of any prior work for this geometry only allows us to compare the performance of individual components of our framework. A similar trend has been observed for the third example where application of the proposed algorithmic framework improves the fractional RCS reduction bandwidth from 39% to about 56%. Altogether, it can be concluded that our procedure allows for significant fractional bandwidth enhancements at the level of 15%–25%, when compared with the existing methodologies.

In more general terms, it should be emphasized that the presented design procedure offers several advances over the traditional methods. First, a machine-learning-powered unit cell optimization ensures globally optimum solution within the parameter space which was not previously achievable using experience-driven methods. Having a good initial design upon the accomplishment of the first and the second stages of the algorithm, fine-tuning of the RCS reduction bandwidth through EM-driven optimization can be realized efficiently. It is further accelerated by means of sparse sensitivity updates.

It is worth mentioning that the employment of the regularization term allows for efficient handling of frequency-localized violations, which leads to a seamless improvement of the overall RCS reduction bandwidth, which is not achievable using conventional formulation of the design task. Additionally, our methodology is fully automated. Once the design problem is formulated in a requisite manner, the algorithm successfully finds the best possible design within a realistic timespan and computational resources.

IV. EXPERIMENTAL SETUP AND RESULTS

In this section, the experimental validation of the metasurface using mushroom-like unit cell designs (see Section III-B) is presented. The monostatic RCS measurement setup is described, and the simulation results are corroborated with the corresponding measurements. Finally, the metasurface performance is benchmarked against the state-of-the-art structures.

A. Measurement Setup and Experimental Validation

The structure described in Section III-B has been fabricated to verify the EM simulation results. A photograph of the proto-typed metasurface is shown in Fig. 20. The RCS performance of a metasurface has been evaluated in terms of reflectivity, owing to limited amenities. The equivalent PEC surface has been used as a reference to quantify the RCS reduction of a metasurface under consideration.
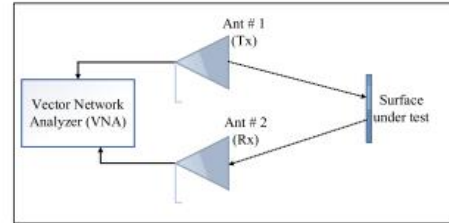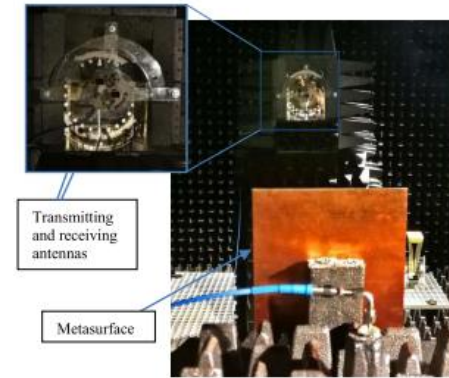

Fig. 22. Measurement setup at Reykjavik University.

The measurement setup consists of a vector network analyzer and the two linearly polarized horn antennas (PE9850/2F-15), used as the transmitter and the receiver, respectively. To certify normal incidence of the impinging waves on a structure, the two antennas are place vertically to the surface under test. The distance between the surface and the antennas is maintained to ensure far-field conditions. The schematic of the measurement setup can be found in Fig. 21. The scattering performance of a surface under test is evaluated by the antenna transmission coefficient, captured by the vector network analyzer. In the same way, the reflection from the equivalent PEC surface has been measured for comparison. The measurements have been carried out using the anechoic chamber of Reykjavik University (see Fig. 22).

Fig. 23 presents the simulation and measurement results in a monostatic environment. There are several factors that contribute to the slight disagreement between the two data sets. The misalignment of the transmitting/receiving antenna with respect to surface under test contributes predominantly. Needless to say, proper orientation of a metasurface (realized manually) is a challenging endeavor. A slight misalignment here may lead to fairly large inconsistencies. However, it is evident that the measured RCS reduction follows a similar trend as its simulated counterpart. Additionally, the measured RCS reduction performance agrees to the 6-dB threshold
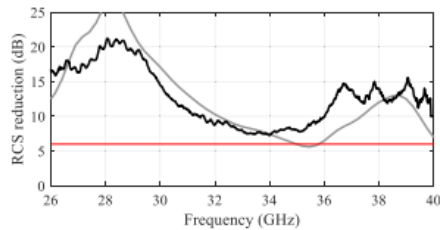
Fig. 23. Measured (black) and simulated (gray) RCS reduction performance comparison. The red curve indicates the 6-dB RCS reduction threshold.
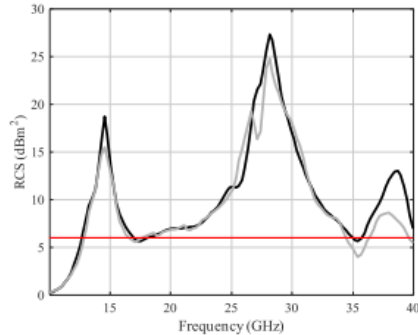

Fig. 24. RCS reduction characteristics of a 2 × 2 (black) and 6 × 6 (gray). The red curve indicates the 6-dB RCS reduction threshold.

TABLE II
DESIGNED METASURFACE VERSUS STATE-OF-THE-ART DESIGNS

Design	Metasurface size (mm³)	Frequency range (>6-dB RCS reduction) (GHz)	Fractional bandwidth (%)
[51]	180×180×3.5	8.6–23.4	92
[52]	328×328×3	5.1–7.9	43
[53]	400×400×3.5	5.9–14.1	82
[54]	264×264×3	8.4–23	93
[55]	112×112×6.35	4–10.8	91
[56]	112×112×6.35	3.75–10	90
[24]	150×150×3.175	7.7–16.5	72
[57]	250×250×3.18	9–19.8	75
This work (Section III.*B*)	48×48×1.5	13–40	>104

in the frequency range of 26.5–40 GHz. The measurement has been limited to over 26.5 GHz due to the available hardware. The above findings allow us to conclude that the designed metasurface features low the scattering property in a broadband frequency range, and therefore, it has the potential to replace the metallic surfaces in applications where high stealthiness is essential.

The primary reason for considering a 2 × 2 metasurface throughout the study is that the RCS reduction performance is always normalized to equivalent size PEC surface, and therefore, the size of the metasurface is a nominal factor. This issue has been discussed in the literature (see [17], [23]). In particular, it has been argued that the RCS reduction performance of a 2 × 2 metasurface with reference to a metallic surface is a decent representative of the corresponding structure of a larger size. This has been numerically corroborated through a comparative study carried out to compare the RCS reduction performance of a 2 × 2 and 6 × 6 metasurface, using the design described in Section III-B. Fig. 24 shows the comparison between these two cases. It can be observed that the RCS reduction responses are well-aligned, which can be viewed as a comparison of the RCS performance invariance with respect to the metasurface size in the considered context.

B. Benchmarking

The main purpose of this article was to propose a systematic framework for computationally efficient and reliable design

optimization of low scattering metasurface. In the course of verification of the presented methodology, it has been demonstrated that it does allow for obtaining higher quality designs than those produced by traditional design approaches.

Here, for the sake of supplementary validation, the metasurface considered in Section III-B is benchmarked against the state-of-the-art designs from the literature to emphasize that our approach is capable of yielding structures that are competitive in terms of relevant performance figures. The latter, for low observable metasurface designs, is primarily the continuous range of frequencies rendering RCS reduction characteristics, when compared with the equivalent metallic surface. For fair assessment, the comparison is carried out in terms of the fractional/relative RCS reduction bandwidth. As indicated in Table II, the presented metasurface design outperforms a number of other reported structures. Additionally, our design covers several radar frequency bands, including Ku, K, and Ka. Consequently, it can be used in a wide selection of applications.

V. CONCLUSION

In this article, we proposed a machine-learning-powered EM-driven design framework to enable the development of high-performance metasurfaces featuring broadband RCS reduction. The latter is particularly desirable in stealth technology, empowering combat aircrafts to potentially evade the enemy's radar to a satisfactory extent. Our framework uses fast metamodels replacing CPU-intensive EM simulations during the initial stages of the design procedure, followed by the expedited EM-driven fine-tuning of the metasurface geometry parameters. Using the surrogate as a fast predictor replacing the EM-simulation model allows us to significantly accelerate the process of determining globally optimal unit cell geometries, that is, maximizing the frequency range for which the required phase difference (here, 180°± 37°) is maintained. The computational cost of the training stage is very much practical (typically, up to a few hours), and it significantly reduces the overall cost of the metasurface design procedure. As a matter of fact, surrogate-assisted approach enables global search, otherwise infeasible when using conventional means.

Subsequently, EM-driven adjustment of the geometry parameters is carried out at the level of the entire metasurface to directly extend the RCS reduction bandwidth. The optimization is realized by applying TR gradient algorithm with sparse sensitivity updates. Furthermore, the objective function for the process is modified by incorporating a regularization term to efficiently handle frequency-localized violations of the RCS reduction threshold. This demonstrably leads to improved reliability and quality of the design process when compared with a conventional formulation of the optimization task.

The design utility of the proposed framework is comprehensively validated using three practical examples, also supported by the experimental validation of a high-performance metasurface involving mushroom-like unit cells. Here, we only considered checkerboard-type metasurfaces; nevertheless, the introduced design optimization methodology is not limited to this particular class of structures. The framework is generic, and it can be applied to any other architecture as long as it is of fixed topology (i.e., the design task can be formulated as the adjustment of geometry/material parameters of the structure). Optimization of the metasurface topology is out of the scope of this work. The overall computational cost of the optimization process typically corresponds to a few dozens of EM simulations of the entire surface at hand, which is remarkably low given that the design process is carried out in a global sense.

The prototyped metasurface has been benchmarked against state-of-the-art designs and demonstrated to be superior in terms of the RCS reduction bandwidth. This further corroborates the efficacy of the proposed algorithmic framework in the development of minimum detectable metasurfaces. The obtained results also reconfirm that optimization of small (2 × 2) surfaces is sufficient in the considered context (i.e., with the reference to a metallic surface).

The authors believe that the algorithmic procedure proposed in this work can be adopted to design of metamaterials and metasurfaces for other application areas so as to address the challenges specific to the respective fields. These include but are not limited to high-gain antennas, optical filters, radomes, and medical devices.

REFERENCES

[1] S. Sun, Q. He, J. Hao, S. Xiao, and L. Zhou, "Electromagnetic metasurfaces: Physics and applications," *Adv. Opt. Photon.*, vol. 11, no. 2, pp. 380–479, 2019.

[2] T. J. Cui, D. R. Smith, and R. Liu, *Metamaterials: Theory, Design, and Applications*. New York, NY, USA: Springer, 2010.

[3] F. Aieta *et al.*, "Aberration-free ultrathin flat lenses and axicons at telecom wavelengths based on plasmonic metasurfaces," *Nano Lett.*, vol. 12, no. 9, pp. 4932–4936, Sep. 2012.

[4] X. Gao, X. Han, W.-P. Cao, H. O. Li, H. F. Ma, and T. J. Cui, "Ultrawideband and high-efficiency linear polarization converter based on double V-shaped metasurface," *IEEE Trans. Antennas Propag.*, vol. 63, no. 8, pp. 3522–3530, Aug. 2015.

[5] F.-C. Huang, C.-N. Chiu, T.-L. Wu, and Y.-P. Chiou, "A circular-ring miniaturized-element metasurface with many good features for frequency selective shielding applications," *IEEE Trans. Electromagn. Compat.*, vol. 57, no. 3, pp. 365–374, Jun. 2015.

[6] M. Paquay, J.-C. Iriarte, I. Ederra, R. Gonzalo, and P. de Maagt, "Thin AMC structure for radar cross-section reduction," *IEEE Trans. Antennas Propag.*, vol. 55, no. 12, pp. 3630–3638, Dec. 2007.

[7] G. A. Rao and S. P. Mahulikar, "Integrated review of stealth technology and its role in airpower," *Aeronaut. J.*, vol. 106, no. 1066, pp. 629–642, Dec. 2002.

[8] T. A. Khan, J. X. Li, Z. Li, M. Abdullah, J. Chen, and A. X. Zhang, "Design of Vivaldi antenna with wideband reduced radar cross section," *AEU Int. J. Electron. Commun.*, vol. 95, pp. 47–51, Oct. 2018.

[9] E. F. Knott, J. F. Schaeffer, and M. T. Michael, *Radar Cross Section*. Rijeka, Croatia: SciTech, 2004.

[10] F. Costa, A. Monorchio, and G. Manara, "Analysis and design of ultra thin electromagnetic absorbers comprising resistively loaded high impedance surfaces," *IEEE Trans. Antennas Propag.*, vol. 58, no. 5, pp. 1551–1558, May 2010.

[11] N. I. Landy, S. Sajuyigbe, J. J. Mock, D. R. Smith, and W. J. Padilla, "Perfect metamaterial absorber," *Phys. Rev. Lett.*, vol. 100, no. 20, pp. 207–402, 2008.

[12] Y. Cheng and H. Yang, "Design simulation and measurement of metamaterial absorber," *J. Appl. Phys.*, vol. 108, 2010, Art. no. 34906.

[13] Y. Ma, Q. Chen, J. Grant, S. C. Saha, A. Khalid, and D. R. S. Cumming, "A terahertz polarization insensitive dual band metamaterial absorber," *Opt. Lett.*, vol. 36, no. 6, pp. 945–947, 2011.

[14] Y. Liu and X. Zhao, "Perfect absorber metamaterial for designing low-RCS patch antenna," *IEEE Antennas Wireless Propag. Lett.*, vol. 13, pp. 1473–1476, 2014.

[15] K. Chang, "Electromagnetic gradient surface and its application to flat reflector antennas," Ph. D. dissertation, Dept. Elect. Electron. Eng., Yonsei Univ., Seoul, South Korea, 2009.

[16] H. P. Seo, Y. S. Kim, Y. Lim, and Y. J. Yoon, "Improving phase continuity in electromagnetic gradient surface for large reflecting structures," in *Proc. IEEE Int. Symp. Antennas Propag.*, Jul. 2012, pp. 1–2.

[17] J. C. Iriarte Galarregui, A. Tellechea Pereda, J. L. M. de Falcon, I. Ederra, R. Gonzalo, and P. de Maagt, "Broadband radar cross-section reduction using AMC technology," *IEEE Trans. Antennas Propag.*, vol. 61, no. 12, pp. 6136–6143, Dec. 2013.

[18] J. C. Iriarte, I. Ederra, R. Gonzalo, and P. de Maagt, "Dual band RCS reduction using planar technology by combining AMC structures," in *Proc. 3rd Eur. Conf. Antennas Propag.*, Mar. 2009, pp. 3708–3709.

[19] M. E. de Cos, Y. Alvarez-Lopez, and F. Las Heras Andres, "On the influence of coupling AMC resonances for RCS reduction in the SHF band," *Prog. Electromagn. Res.*, vol. 117, pp. 103–119, 2011.

[20] M. E. de Cos, Y. Á. Lvarez, and F. Las-Heras, "RCS reduction using a combination of artificial magnetic conductors," in *Proc. 5th Eur. Conf. Antennas Propag. (EUCAP)*, Apr. 2011, pp. 1336–1340.

[21] J. C. Iriarte *et al.*, "Broadband RCS reduction using AMC technology," in *Proc. 5th Eur. Conf. Antennas Propag. (EUCAP)*, Apr. 2011, pp. 1322–1323.

[22] Y. Fu, Y. Li, and N. Yuan, "Wideband composite AMC surfaces for RCS reduction," *Microw. Opt. Technol. Lett.*, vol. 53, no. 4, pp. 712–715, Apr. 2011.

[23] W. Chen, C. A. Balanis, and C. R. Birtcher, "Checkerboard EBG surfaces for wideband radar cross section reduction," *IEEE Trans. Antennas Propag.*, vol. 63, no. 6, pp. 2636–2645, Jun. 2015.

[24] S. H. Kim and Y. J. Yoon, "Wideband radar cross-section reduction on checkerboard metasurfaces with surface wave suppression," *IEEE Antennas Wireless Propag. Lett.*, vol. 18, no. 5, pp. 896–900, May 2019.

[25] T. Han, X.-Y. Cao, J. Gao, Y.-L. Zhao, and Y. Zhao, "A coding metasurface with properties of absorption and diffusion for RCS reduction," *Prog. Electromagn. Res. C*, vol. 75, pp. 181–191, 2017.

[26] F. Costa, A. Monorchio, and G. Manara, "Wideband scattering diffusion by using diffraction of periodic surfaces and optimized unit cell geometries," *Sci. Rep.*, vol. 6, no. 1, Jul. 2016, Art. no. 25458.

[27] Y. Zhao *et al.*, "Broadband diffusion metasurface based on a single anisotropic element and optimized by the simulated annealing algorithm," *Sci. Rep.*, vol. 6, no. 6, Jul. 2016, Art. no. 23896.

[28] A. Edalati and K. Sarabandi, "Wideband, wide angle, polarization independent RCS reduction using nonabsorptive miniaturized-element frequency selective surfaces," *IEEE Trans. Antennas Propag.*, vol. 62, no. 2, pp. 747–754, Feb. 2014.

[29] Y.-C. Hou, W.-J. Liao, C.-C. Tsai, and S.-H. Chen, "Planar multilayer structure for broadband broad-angle RCS reduction," *IEEE Trans. Antennas Propag.*, vol. 64, no. 5, pp. 1859–1867, May 2016.

[30] H. Yang *et al.*, "A programmable metasurface with dynamic polarization, scattering and focusing control," *Sci. Rep.*, vol. 6, no. 1, Dec. 2016, Art. no. 35692.

[31] M. Chen, M. Kim, A. M. H. Wong, and G. V. Eleftheriades, "Huygens' metasurfaces from microwaves to optics: A review," *Nanophotonics*, vol. 7, no. 6, pp. 1207–1231, Jun. 2018.

[32] J. Ji, J. Jiang, G. Chen, F. Liu, and Y. Ma, "Research on monostatic and bistatic RCS of cloaking based on coordinate transformation," *Optik*, vol. 165, pp. 117–123, Jul. 2018.

[33] S. Sui *et al.*, "Absorptive coding metasurface for further radar cross section reduction," *J. Phys. D, Appl. Phys.*, vol. 51, no. 6, Feb. 2018, Art. no. 065603.

[34] S. Koziel and A. Pietrenko-Dabrowska, "Efficient gradient-based algorithm with numerical derivatives for expedited optimization of multi-parameter miniaturized impedance matching transformers," *Radioengineering*, vol. 27, no. 3, pp. 572–578, Sep. 2019.

[35] X. Lin *et al.*, "All-optical machine learning using diffractive deep neural networks," *Science*, vol. 361, no. 6406, pp. 1004–1008, Sep. 2018.

[36] A. D. Tranter *et al.*, "Multiparameter optimisation of a magneto-optical trap using deep learning," *Nature Commun.*, vol. 9, Oct. 2018, Art. no. 4360.

[37] J. Peurifoy *et al.*, "Nanophotonic particle simulation and inverse design using artificial neural networks," *Sci. Adv.*, vol. 4, no. 6, Jun. 2018, Art. no. eaar4206.

[38] X. Chen, W. Xue, H. Shi, L. Wang, S. Zhu, and A. Zhang, "Improving field uniformity using source stirring with orbital angular momentum modes in a reverberation chamber," *IEEE Microw. Wireless Compon. Lett.*, vol. 29, no. 8, pp. 560–562, Aug. 2019.

[39] X. Chen, W. Xue, H. Shi, J. Yi, and W. E. I. Sha, "Orbital angular momentum multiplexing in highly reverberant environments," *IEEE Microw. Wireless Compon. Lett.*, vol. 30, no. 1, pp. 112–115, Jan. 2020.

[40] T. W. Simpson, J. D. Poplinski, P. N. Koch, and J. K. Allen, "Metamodels for computer-based engineering design: Survey and recommendations," *Eng. Comput.*, vol. 17, no. 2, pp. 129–150, Jul. 2001.

[41] S. Koziel, L. Leifsson, and X. S. Yang, "Surrogate-based optimization," in *Simulation-Driven Design Optimization and Modeling for Microwave Engineering*, S. Koziel, X. S. Yang, and Q. J. Zhang, Eds. London, U.K.: Imperial College Press, 2012, pp. 41–80.

[42] S. Koziel and J. W. Bandler, "Reliable microwave modeling by means of variable-fidelity response features," *IEEE Trans. Microw. Theory Techn.*, vol. 63, no. 12, pp. 4247–4254, Dec. 2015.

[43] S. Koziel and A. Pietrenko-Dabrowska, *Performance-Driven Surrogate Modeling of High-Frequency Structures*. New York, NY, USA: Springer, 2020.

[44] F. Feng *et al.*, "Multifeature-assisted neuro-transfer function surrogate-based EM optimization exploiting trust-region algorithms for microwave filter design," *IEEE Trans. Microw. Theory Techn.*, vol. 68, no. 2, pp. 531–542, Feb. 2020.

[45] S. Koziel and A. Pietrenko-Dabrowska, "Expedited optimization of antenna input characteristics with adaptive broyden updates," *Eng. Comput.*, vol. 37, no. 3, pp. 851–862, Sep. 2019.

[46] J. Jiang and J. A. Fan, "Simulator-based training of generative neural networks for the inverse design of metasurfaces," *Nanophotonics*, vol. 9, no. 5, pp. 1059–1069, Nov. 2019.

[47] W. Ma, F. Cheng, Y. Xu, Q. Wen, and Y. Liu, "Probabilistic representation and inverse design of metamaterials based on a deep generative model with semi-supervised learning strategy," *Adv. Mater.*, vol. 31, no. 35, Aug. 2019, Art. no. 1901111.

[48] A. Hoorfar, "Evolutionary programming in electromagnetic optimization: A review," *IEEE Trans. Antennas Propag.*, vol. 55, no. 3, pp. 523–537, Mar. 2007.

[49] A. R. Conn, N. I. M. Gould, and P. L. Toint, *Trust Region Methods* (MPS-SIAM Series on Optimization). Philadelphia, PA, USA: Society for Industrial and Applied Mathematics, 2000.

[50] S. Koziel, J. W. Bandler, and Q. S. Cheng, "Robust trust-region space-mapping algorithms for microwave design optimization," *IEEE Trans. Microw. Theory Techn.*, vol. 58, no. 8, pp. 2166–2174, Aug. 2010.

[51] S. H. Esmaeli and S. H. Sedighy, "Wideband radar cross-section reduction by AMC," *Electron. Lett.*, vol. 52, no. 1, pp. 70–71, Jan. 2016.

[52] X. Liu, J. Gao, L. Xu, X. Cao, Y. Zhao, and S. Li, "A coding diffuse metasurface for RCS reduction," *IEEE Antennas Wireless Propag. Lett.*, vol. 16, pp. 724–727, 2017.

[53] J. Yang, Y. Cheng, C. Ge, and R. Gong, "Broadband polarization conversion metasurface based on metal cut-wire structure for radar cross section reduction," *Materials*, vol. 11, no. 4, p. 626, Apr. 2018.

[54] L. Ali, Q. Li, T. A. Khan, J. Yi, and X. Chen, "Wideband RCS reduction using coding diffusion metasurface," *Materials*, vol. 12, no. 17, p. 2708, 2019.

[55] W. Chen, C. A. Balanis, and C. R. Birtcher, "Dual wide-band checker-board surfaces for radar cross section reduction," *IEEE Trans. Antennas Propag.*, vol. 64, no. 9, pp. 4133–4138, Sep. 2016.

[56] A. Y. Modi, C. A. Balanis, C. R. Birtcher, and H. N. Shaman, "Novel design of ultrabroadband radar cross section reduction surfaces using artificial magnetic conductors," *IEEE Trans. Antennas Propag.*, vol. 65, no. 10, pp. 5406–5417, Oct. 2017.

[57] Q. Zheng *et al.*, "Wideband, wide-angle coding phase gradient metasurfaces based on pancharatnam-berry phase," *Sci. Rep.*, vol. 7, no. 1, Apr. 2017, Art. no. 43543.

[58] Y. Zhuang, G. Wang, J. Liang, T. Cai, W. Guo, and Q. Zhang, "Flexible and polarization-controllable diffusion metasurface with optical transparency," *J. Phys. D, Appl. Phys.*, vol. 50, no. 46, Nov. 2017, Art. no. 465102.

Slawomir Koziel (Senior Member, IEEE) received the M.Sc. and Ph.D. degrees in electronic engineering from the Gdansk University of Technology, Gdansk, Poland, in 1995 and 2000, respectively, and the M.Sc. degrees in theoretical physics and in mathematics and the Ph.D. degree in mathematics from the University of Gdansk, Gdansk.

He is currently a Professor with the Department of Engineering, Reykjavik University, Reykjavik, Iceland. His research interests include CAD and modeling of microwave and antenna structures, simulation-driven design, surrogate-based optimization, space mapping, circuit theory, analog signal processing, evolutionary computation, and numerical analysis.

Muhammad Abdullah received the B.Sc. degree from the University of Engineering and Technology, Lahore, Pakistan, in 2016, and the M.Sc. degree from Xi'an Jiaotong University (XJTU), Xi'an, China, in 2019.

Since late 2019, he has been associated with the Department of Engineering, Reykjavik University, Reykjavik, Iceland, as a Researcher. From 2018 to 2019, he was with the Electromagnetics and Communication Laboratory, XJTU. On completion of M.Sc. degree, he received the excellent master's thesis award. His broader research interests include surrogate-based modeling and optimization, CAD and modeling of antennas and other high-frequency structures, simulation-driven design, machine-learning techniques, and millimeter-wave communication.

Chapter 5

5 Paper # 3

Muhammad Abdullah and Slawomir Koziel

Supervised-Learning-Based Development of Multi-Bit RCS-Reduced Coding Metasurfaces

Supervised-Learning-Based Development of Multibit RCS-Reduced Coding Metasurfaces

Muhammad Abdullah and Slawomir Koziel, *Senior Member, IEEE*

Abstract—Coding metasurfaces have been introduced as efficient tools allowing meticulous control over the electromagnetic (EM) scattering. One of their relevant application areas is radar cross section (RCS) reduction, which principally relies on the diffusion of impinging EM waves. Despite its significance, careful control of the scattering properties poses a serious challenge at the level of practical realization. This article is concerned with (global) design optimization of coding metasurfaces featuring broadband RCS reduction. We adopt a two-stage optimization procedure involving data-driven supervised-learning, sequential-search strategy, and direct EM-based design closure of the entire metasurface oriented toward maximizing the RCS reduction bandwidth. Our framework is then used to develop a two-bit coding metasurface. To handle the combinatorial explosion at the concurrent meta-atom optimization stage, a sequential-search strategy has been developed that enables global search capability at low computational cost. Finally, EM-based optimization is executed to maximize RCS reduction bandwidth at the level of entire metasurface. The properties of the coding metasurface are demonstrated using monostatic and bistatic RCS performance. The 10-dB RCS reduction can be obtained in the frequency range of 14.8–37.2 GHz, in a monostatic configuration. Also, 15-dB RCS reduction can be maintained in the frequency range of 16.7–37 GHz. Simulations are validated using physical measurements of the fabricated prototypes. Finally, the performance of the structure is benchmarked against recently reported designs.

Index Terms—Beam manipulation, coding metasurface, diffusion, multibit coding, radar cross section (RCS), supervised learning.

I. INTRODUCTION

WITH the advancements in radar detection methods, improving stealthiness of aircrafts has become a forefront of research within the stealth technology [1]–[3]. Conventional approaches adopted to accomplish the stealth features commonly involve shape and material stealth [4]. The former impacts the aerodynamic performance and structural integrity of the aircraft. The latter suffers from the increased thickness, weight, and cost. A relatively new class of artificially engineered materials, or metamaterials, has recently become a viable alternative to conventional stealth approaches.

A metasurface is a planar patterned surface composed of subwavelength periodic arrays of meta-atoms (or unit cells), offering extraordinary characteristics [5]. Until now, metasurfaces are developed as either absorbing metasurfaces [6]–[8] or scattering manipulation metasurfaces [9]–[23]. The former ones are designed to convert the electromagnetic (EM) wave energy into heat and dissipate it. These metasurfaces are susceptible to infrared detectors, which increases their detection probability. In 2011, Yu *et al.* [9] proposed a generalized Snell's law, followed by the introduction of the idea of scattering manipulation [10] and, finally, the design of the metasurface composed of V-shaped meta-atoms [10]. Therein, the phase and the amplitude of the EM wave can be effectively manipulated by changing the meta-atom geometry. Also, the weight, thickness, and losses of the structure can be maintained below a certain, practically acceptable level. These attributes make the scattering control metasurfaces a hotspot in the stealth research.

Contemporary metasurfaces can be classified into single-beam [9], [10], multibeam [11]–[13], and the diffusion metasurfaces [14]–[19]. The single-beam scattering metasurfaces offer radar cross section (RCS) reduction in a monostatic configuration; however, they are not effective to reduce bistatic RCS, essential in the context of multibase radar detection technology. To realize RCS reduction in a bistatic regime, it is important to increase the number of scattering beams. One example is a checkerboard metasurface [13], employing two distinct meta-atom designs in a chessboard configuration. The two meta-atoms represents two-phase states (0 and π) to realize essential RCS reduction [13]. However, a limited number of scattering beams and a fixed beam propagation direction limit the widespread utility of a checkerboard metasurface. To further increase the number of scattering beams, the idea of diffusion metasurface (also referred to as a coding metasurface) has been presented [14]–[16], featuring a random arrangement of the meta-atoms. This leads to the increased number of scattered beams and, hence, successful bistatic RCS reduction. In [15] and [16], the coding diffusion metasurfaces are exploited to achieve the required RCS reduction performance. Yet, the RCS reduction performance of such structures is limited up to 50° angle of incidence (as in [15]). In this class of metasurfaces, the major scattering directions remain within

a certain angular range, which might have adverse effects on the RCS performance. The absence of rigorous methods of predicting and controlling the allocation of the scattered beams hinders the widespread use of diffusion metasurfaces. Their backscattering characteristics solely rely on the geometrical structure of meta-atoms. To provide additional degrees of freedom and to facilitate the manipulation of EM waves, four types of meta-atom designs representing four phase states $(0, \pi/2, \pi,$ and $3\pi/2)$ can be utilized as a building block of a two-bit coding metasurface [20], [21]. However, the development of such architectures involves concurrent optimization of the meta-atoms. The lack of efficient techniques to optimize individual meta-atoms and the entire metasurface limits the performance of multibit coding metasurfaces, in particular, their RCS reduction bandwidth.

Conventional metasurface design methodologies employ empirical reasoning and intuition-inspired practices. The two design stages involved in the process are the design and optimization of individual meta-atoms, followed by the optimization of the entire metasurface. Due to the absence of reliable analytical models, the only practical choice is experience-driven design methods. Unfortunately, such approaches exhibit limited efficacy as well as capability to identify truly optimum designs. Efficient development of multibit metasurfaces requires innovative algorithmic solutions, capable of tacking the aforementioned downsides. The developments in high-performance computing have dramatically boosted the utility of rigorous EM-driven design procedures, principally based on numerical optimization [24]. However, direct EM-based optimization of complex structures using conventional algorithms may be prohibitively expensive, especially if global exploration is needed. A practical solution might be the utilization of supervised machine learning [25], involving metamodeling [26]–[29]. Shifting the computational overhead to a cheaper metamodel, implementing a sequential-search strategy, and finally incorporating other means such as problem decomposition [31] may enable efficient development of complex multibit metasurfaces, otherwise impractical.

This work proposes a novel algorithmic framework for global optimization of two-bit coding metasurface featuring broadband RCS reduction performance. The metasurface is composed of lattices featuring four unique geometries of meta-atoms to mimic "00," "01," "10," and "11" binary codes, standing for a phase reflection state of $0, \pi/2, \pi,$ and $3\pi/2$, respectively. The optimization procedure adopted in this work involves a data-driven supervised-learning technique [32], sequential-search strategy to face combinatorial explosion and permit global exploration, as well as EM-based local optimization of the entire structure at hand. It should be noted that the concept of supervised-learning-based optimization procedure has been adopted from [32]; however, the global optimization procedure (the sequential-search algorithm) has been developed specifically to tackle the challenges pertinent to handling four meta-atoms, where the original approach of [32] would not work due to excessive computational costs. Supervised learning involves sampled EM simulation data, with the surrogate model implemented using kriging interpolation [25]. The latter serves as a meta-atom phase characteristic predictor during the global optimization stage. The sequential-search strategy is introduced to decompose the optimization task by gradually increasing the pool of simultaneously considered pairs of meta-atoms, thus effectively administering the computational overhead. This turns instrumental in handling the task, otherwise computationally prohibitive considering the large dimensionality of the parameter space. At the EM-based local optimization stage, a trust-region (TR) gradient algorithm with sparse sensitivity updates [31] and a regularization approach is applied to expedite the optimization procedure and to efficiently handle frequency-localized violations of assumed level of the RCS reduction.

The adopted algorithmic solution addresses the key challenges pertinent to global optimization of meta-atom designs in a fully automated manner. It has been applied to develop a multibit coding metasurface featuring 10-dB RCS reduction in a frequency range from 14.8 to 37.5 GHz. The design is validated both numerically and experimentally and shown to outperform the state-of-the-art benchmark structures with respect to the RCS reduction bandwidth and the level RCS reduction.

The technical novelty and major contributions of this article can be summarized as follows: 1) development of an algorithmic solution to enable systematic and globally optimum meta-atom designs; 2) development of sequential approach for global optimization of meta-atoms to address the issue of combinatorial explosion when handling simultaneous parameter tuning of multiple unit cells; 3) development of alternative objective function formulation for efficient EM-driven design closure of the metasurface, addressing the problem of discontinuities due to localized violations of the acceptance threshold for the RCS reduction; 4) corroborating the efficacy of the design procedure as well as demonstrating its practical utility in the context of complex metasurface design and optimization; and 5) the employment of the proposed algorithmic framework to the development of a high-performance two-bit coding metasurface for broadband RCS reduction. It should be emphasized that the proposed algorithmic solution is—to the authors' best knowledge—the first endeavor in the literature to ensure globally optimum meta-atom designs, indispensable in the development of complex multibit coding metasurfaces. At the same time, it should be reiterated that the primary point of interest and the scope of the article are numerical optimization of multibit coding metasurfaces, in particular introduction of a procedure for identifying globally optimum parameter setup and providing the means that allow us to solve numerical challenges that arise on the way (cf. points (ii) and (iii) mentioned above). Proposing methods for RCS reduction is outside the scope of this work. The considered specific metasurface design is discussed merely as a demonstration example for the algorithmic framework.

This article is organized as follows. In Section II, we introduce the geometry and EM modeling of the exemplary meta-atom, subsequently used to develop the RCS reduction metasurface and to demonstrate the considered algorithmic solution. Section III provides the comprehensive description of the supervised-learning-enabled concurrent meta-atom optimization procedure. Section IV discusses the
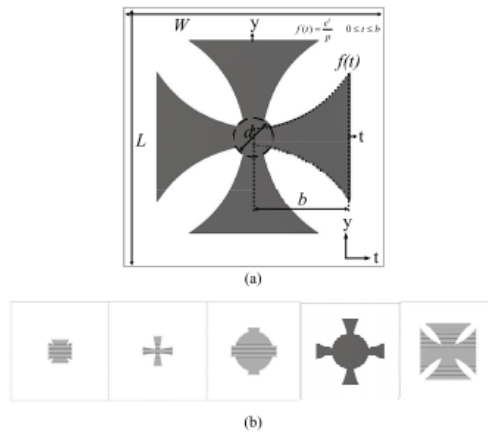
Fig. 1. Configuration of the meta-atom considered in this work. (a) Crusader cross topology. (b) Five exemplary meta-atom geometries within the parameter space.

Fig. 2. Coding sequence applied to develop 4 × 4 diffusion metasurface.

optimization results, followed by a demonstration of a two-bit coding metasurface and its experimental validation. Section V concludes this article.

II. GEOMETRY CONFIGURATION OF META-ATOMS AND CODING METASURFACE

This section describes the topology of a considered meta-atom (metasurface building block). It also contains a brief discussion concerning the coding sequence applied in the development procedure of a two-bit coding metasurface utilized to demonstrate the algorithmic framework proposed in the work.

A. Meta-Atom Geometry

Fig. 1(a) shows the geometry of a meta-atom design considered in this work. The underlying topology is borrowed from [32], and it resembles the crusader cross. The geometry is parameterized as

$$f(t) = \frac{e^t}{p}, \quad 0 \leq t \leq b \tag{1}$$

where p, b, and d, are the designable variables that determine the overall structure of the meta-atom. The considered geometry offers ample flexibility in the meta-atom design [cf. Fig. 1(b)] while using a small number of designable variables. The latter facilitates the supervised-learning-based modeling process and, in particular, ensures the reliability of the replacement model without incurring excessive computational expenses. Fig. 1(b) shows the geometrical flexibility of the considered meta-atom design, i.e., broad ranges of visually distinct topologies that can be generated using the basic geometry of Fig. 1(a).

A ground-backed Arlon AD250 is modeled as a dielectric layer with a relative permittivity of ($\varepsilon_r = 2.5$), a loss tangent

of ($\tan\delta = 0.0018$), and a thickness of ($h = 1.5$ mm). Perfect electrical conductor (PEC) is selected as the metallic material in the computational (EM simulation) model. The overall size of the meta-atom is $W \times L = 6 \times 6$ mm^2.

B. Coding Sequence of a Two-Bit Coding Metasurface

The development of a two-bit coding metasurface requires the utilization of four meta-atom designs. Consequently, the coding sequence encompassing four atoms is sophisticated than that corresponding to the standard chessboard configuration involving only two atoms. Here, the four atoms are represented as "00," "01," "10," and "11," in the arrangement shown in Fig. 2. Each atom represents a phase reflection state of 0, $\pi/2$, π, and $3\pi/2$, respectively. As presented, the entire matrix includes sixteen lattices, arranged in a 4 × 4 configuration.

III. SUPERVISED-LEARNING-ENABLED METASURFACE OPTIMIZATION FRAMEWORK

This section briefly describes the implementation of a supervised-learning-based design procedure. We start by summarizing the complete procedure, followed by a discussion of the major components of the two-stage optimization procedure.

A. Design Approach Summary

The complete metasurface design procedure consists of two independent optimization stages. The first stage involves construction of a fast replacement model (surrogate) of the meta-atom within the parameter space determined by the lower and upper bounds of designable variables. Here, the allocation of the training samples on a rectangular grid is followed by data acquisition through EM simulations of the meta-atom computational model. The surrogate itself is rendered using kriging interpolation. The trained model is utilized as a prediction tool for global exploration of the parameter space. The latter is computationally prohibitive when executed directly at the level of the EM simulation model. Low dimensionality of the parameter space allows sufficient prediction power of the surrogate and thus to eliminate EM analysis from the global exploration stage altogether. Furthermore, the global search is carried out in a sequential manner to efficiently handle combinatorial explosion pertinent to concurrent optimization of four meta-atoms. Finally, EM-driven optimization of the entire metasurface is performed to directly extend the RCS
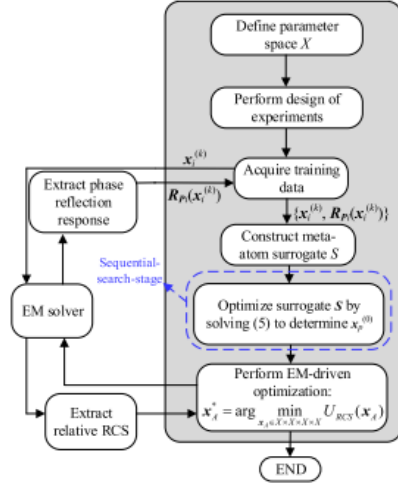
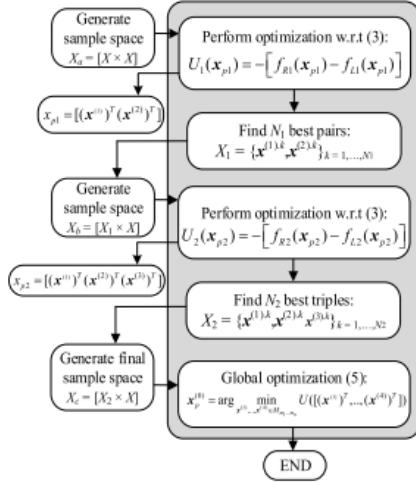Fig. 3. Flow diagram of the supervised-learning-based design procedure.

Fig. 4. Algorithmic flow of a sequential-search stage (cf. Fig. 3).

reduction bandwidth. The flow diagram of the complete design optimization procedure along with a separate illustration of the global search stage is shown in Figs. 3 and 4, respectively. The details concerning individual parts of the process are provided in the remaining part of this section.

B. Data-Driven Modeling and Concurrent Optimization of Meta-Atoms

The initial optimization stage involves data-driven meta-models [32]. It determines four globally optimum meta-atom

designs exhibiting the phase difference within the range of $\{j\pi/2 \pm \alpha_{\max}\}_{j=1,2,3}$ over a possibly broad frequency range F. The threshold $\alpha_{\max}$ is set to 37°, considering practical recommendations in the literature (see [13]). These phases are understood as pertaining to the first and the second meta-atom ($\pi/2 \pm \alpha_{\max}$), the second and the third meta-atom ($2\pi/2 \pm \alpha_{\max}$), and the third and the fourth atom ($3\pi/2 \pm \alpha_{\max}$).

The vector of designable variables and the response of the EM simulation model will be denoted as $x = [x_1, \ldots, x_n]^T \in X$ and $R_P(x)$, respectively. The latter represents the phase reflection characteristics of the corresponding meta-atom design.

The parameter space X is defined by the lower and upper bounds $l = [l_1, \ldots, l_n]^T$ and $u = [u_1, \ldots, u_n]^T$ such that $l_l \leq x_l \leq u_l$, $l = 1, \ldots, n$.

The data acquisition is accomplished by uniformly allocating N samples within the parameter space X and obtaining their corresponding EM simulation responses. Therein, the surrogate model S is trained by means of kriging interpolation [25]. The model is identified using the training samples $\{x^{(k)}, R_P(x^{(k)})\}_{k=1,\ldots,N}$. The samples are allocated on a rectangular grid, with the number of grid nodes along each parameter space axis decided based on a large-scale sensitivity analysis. This design of experiments is suitable for low-dimensional parameter spaces. The kriging model uses the first-order polynomial as a trend function and a Gaussian correlation function.

The surrogate model is employed to carry out global optimization of the four meta-atom designs, aiming at identification of the variable vectors $x^{(j)*}$, $j = 1, 2, 3$, and 4, such that that the phase differences at the level of the surrogate model, i.e., $\Delta P(x^{(j)*}, x^{(j+1)*}) = S(x^{(j)*}) - S(x^{(j+1)*})$, simultaneously conform to

$$\frac{j\pi}{2} - \alpha_{\max} \leq \Delta P\left(x^{(j)*}, x^{(j+1)*}\right) \leq \frac{j\pi}{2} + \alpha_{\max} \quad (2)$$

for $j = 1, 2$, and 3, over a possibly wide range of frequencies. As mentioned before, we set $\alpha_{\max} = 37°$. Using the aggregated variable vector where the objective function U is defined as

$$x_p = \left[(x^{(1)})^T (x^{(2)})^T (x^{(3)})^T (x^{(4)})^T\right]^T \quad (3)$$

the design task can be formulated as follows:

$$x_p^* = \arg \min_{x_p \in X \times X \times X \times X} U(x_p). \quad (4)$$

The objective function U is defined as

$$U(x_p) = -\left[f_R(x_p) - f_L(x_p)\right] \quad (5)$$

where f_L and f_R are the frequencies determining the largest continuous frequency range for which the phase difference condition (2) is satisfied for all frequencies $f \in [f_L, f_R]$.

Having a fast surrogate model, the intention is to perform a global grid-constrained exhaustive search, followed by a local refinement. We denote by $M_{m1,\ldots,mn}$ a rectangular grid defined so that $x \in M_{m1,\ldots,mn}$ if and only if $x = [x_1, \ldots, x_n]^T$ is of the form $x_k = l_k + j_k[(u_k - l_k)/m_k]$, $k = 1, \ldots, n$, where m_k is a grid-defining integer for the kth variable and $j_k \in \{0, 1, \ldots, m_k\}$. Exhaustive search entails solving the problem

$$x_p^{(0)} = \arg \min_{x^{(1)}, \ldots, x^{(4)} \in M_{m_1, \ldots, m_n}} U([(x^{(1)})^T, \ldots, (x^{(4)})^T]). \quad (6)$$

Unfortunately, with four meta-atoms, we face combinatorial explosion: assuming, for the sake of example, that the grid $M_{m1,\ldots,mn}$ has $N_0 = 1000$ nodes, the number of designs to consider is 10^{12}, which is computationally prohibitive even with a fast surrogate. Here, in order to address this issue, a sequential procedure is implemented as follows.

1) Consider the first two meta-atoms. Among all combinations $x^{(1)}$, $x^{(2)} \in M_{m1,\ldots,mn}$, and select N_1 best pairs $X_1 = \{x^{(1).k}, x^{(2).k}\}_{k=1,\ldots,N1}$, with respect to the objective function $U_1(x_{p1}) = U_1([(x^{(1)})^T (x^{(2)})^T]^T)$, where $U_1(x_{p1}) = -[f_{R1}(x_{p1}) - f_{L1}(x_{p1})]$, with f_{L1} and f_{R1} being the frequencies determining the largest continuous frequency range for which the condition (2) is satisfied within $f \in [f_{L1}, f_{R1}]$ for $j = 1$.

2) Consider the first three meta-atoms. Among all combinations $x^{(1)}$, $x^{(2)}$, and $x^{(3)}$ such that $\{x^{(1)}, x^{(2)}\} \in X_1$ and $x^{(3)} \in M_{m1,\ldots,mn}$, select N_2 best triples $X_2 = \{x^{(1).k}, x^{(2).k}, x^{(3).k}\}_{k=1,\ldots,N1}$, with respect to the objective function $U_2(x_{p2}) = U_1([(x^{(1)})^T (x^{(2)})^T (x^{(3)})^T])$, where $U_2(x_{p2}) = -[f_{R2}(x_{p2}) - f_{L2}(x_{p2})]$, with f_{L2} and f_{R2} being the frequencies determining the largest continuous frequency range for which the condition (2) is satisfied within $f \in [f_{L2}, f_{R2}]$ for $j = 1$ and 2 simultaneously.

3) Consider all four meta-atoms. Among all combinations $x^{(1)}$, $x^{(2)}$, $x^{(3)}$, and $x^{(4)}$ such that $\{x^{(1)}, x^{(2)}, x^{(3)}\} \in X_2$ and $x^{(4)} \in M_{m1,\ldots,mn}$, find the best vector $x_p^{(0)}$ according to the objective function (6).

Note that the number of combinations that have to be considered at steps 2 and 3 of the above procedure is only $N_0 N_1$, instead of N_0^3 and N_0^4, respectively. Thus, the overall number of considered grid node combinations is only $N_0(N_0 + 2N_1)$, which would be $3N_0^3$ if $N_1 = N_0$ is selected (as in our actual numerical experiments). Again, assuming $N_0 = 1000$ (in practice, less than that, cf. Section IV-A), the reduction of cost is six orders of magnitude. At the same time, the probability of finding a truly optimum design this way is very high because it is extremely likely that the global optimum of (6) will be among the best N_1 combinations of the first two meta-atoms contained in X_1 and even more so among the best N_1 combinations of the first three meta-atoms contained in X_2.

The design $x_p^{(0)}$ is further refined using standard gradient-based search at the level of the surrogate S. This is to improve the resolution beyond the initial grid $M_{m1,\ldots,mn}$. When using the above-described surrogate-assisted sequential procedure, the computational cost of the global optimization stage is low.

C. EM-Driven Design Optimization of Entire Metasurface

Following global optimization of the meta-atoms, EM-driven refinement of the entire metasurface is needed. The latter is indispensable as the optimized meta-atoms do not directly translate into optimum design of the entire structure; recall that meta-atoms were tuned to satisfy the phase difference condition (2), whereas the ultimate goal is to maximize the RCS reduction bandwidth, and therefore, the enhancement has to be performed directly. Moreover, due
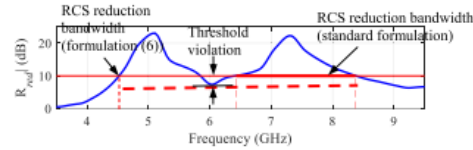

Fig. 5. Exemplary RCS reduction characteristics representing potential practical issues. The thick red horizontal line represents the RCS bandwidth (B_{RCS}) according to the standard formulation, whereas the dashed red horizontal line represents B_{RCS} as defined by (7). If the RCS reduction characteristics changes in the course of the optimization process to create the acceptance threshold violation as shown in the picture, a large discontinuity of the bandwidth will be observed (when evaluated using the standard formulation), which is problematic to the optimization process. As opposed to that, the formulation (7) accommodates the violation without creating any discontinuities.
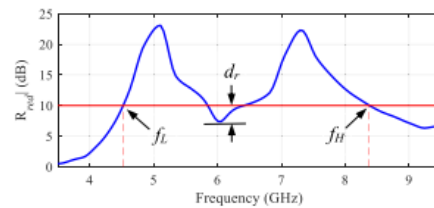

Fig. 6. Exemplary RCS characteristic with the lower frequency f_L, upper frequency f_H, and r_{max} violation d_r marked to indicate the defining quantities of the objective function for RCS reduction bandwidth improvement.

to high computational cost incurred by structure evaluation, TR gradient-based algorithm is the only practical choice. Even in that case, certain acceleration mechanisms should be incorporated to reduce the CPU overhead to acceptable levels.

Let x_A denote the aggregated designable parameter vector of four meta-atoms. Furthermore, let $R_{red}(x_A, f)$ represent the RCS reduction characteristics over frequency f. The RCS reduction bandwidth B_{RCS} is defined as the continuous range of frequencies satisfying the condition $R_{red}(x_A, f) \geq r_{max}$, where r_{max} stands for acceptance threshold (e.g., 10 or 15 dB).

A practical challenge associated with the standard formulation of the optimization task is that local violations of the condition $R_{red}(x_A, f) \geq r_{max}$, unavoidable in the course of the optimization run, lead to discontinuities of the objective function (here, the RCS reduction bandwidth), as shown in Fig. 5. These are problematic to gradient-based optimization algorithms. A workaround is regularization, where violations are incorporated into the objective function without creating discontinuities and large jumps in the (formally defined) bandwidth. A possible formulation is the following, see Fig. 6. Here, f_L and f_H represent the minimum and the maximum frequency for which the condition $R_{red}(x_A, f) \geq r_{max}$ is satisfied. Let d_r denote the maximum allowed violation within the frequency interval $[f_L f_H]$. Using these, the objective function U_{RCS} for metasuface optimization will be defined as

$$U_{RCS}(x_A) = -[f_H(x_A) - f_L(x_A)] + \beta c_r(x_A)^2. \quad (7)$$

The first term in (7) is the RCS reduction bandwidth (the minus sign is to convert the problem into a minimization task).

The second component is a regularization term with the function c_r defined as $c_r(x_A) = d_r$ if $d_r > 0$ and zero otherwise. It is introduced to increase the objective function if violation of the acceptance threshold appears. The contribution of the regularization term is controlled by coefficient β. Here, it is set to $\beta = 1$, but this value is not critical. Nevertheless, it can be used to control the tolerance level of d_r.

The formulation (7) efficiently addresses the issues related to the standard formulation, particularly, the in-band violations of the objective function within the potential bandwidth. The parameter adjustment task is formulated as

$$x_A^* = \arg\min_{x_A \in X \times X \times X \times X} U_{RCS}(x_A). \tag{8}$$

Optimization is performed using the TR gradient search algorithm [33], [34]. To expedite the process, the Jacobian matrix of R_{red} is estimated using finite differentiation in the first iteration and then updated using the rank-one Broyden formula [31] in the subsequent iterations. Typically, the number of EM simulations required to achieve an optimal solution is $M \cdot n$, where n is the number of designable variables, and $M = 3–4$.

IV. RESULTS AND DISCUSSION

A. Numerical and Experimental Validation of the Metasurface

This section presents the modeling and optimization results together with the performance evaluation of the optimum meta-atom designs. The design configuration of the coding metasurface is also demonstrated along with its experimental validation, followed by a discussion of its monostatic and bistatic RCS performance.

B. Modeling and Optimization Results of Meta-Atoms

The meta-atom design under consideration [cf. Fig. 1(a)] has three geometry parameters, i.e., p, b, and d. Hence, the vector of designable variables is $x = [p\ b\ d]^T$; L and W are fixed. The parameter space X is determined by the lower and upper bounds $l = [3.5\ 0.3\ 0.2]^T$ and $u = [10\ 1.6\ 2.4]^T$; all dimensions are in mm. The training samples are distributed on a uniform grid $M_{7.12.7}$ (cf. Section III-B) with a total number of $N = 588$ samples. The acquired EM simulation data have been divided into the training (85 percent) and the test data (15 percent), later utilized for model accuracy evaluation. The frequency-domain solver of the CST Microwave Studio is utilized to evaluate the phase reflection responses of the meta-atoms.

The absolute error of the surrogate model is as low as 0.86° (averaged over the testing set) with the standard deviation of 1.7°. These figures demonstrate good predictive power of the surrogate, especially when considering the typical range of the meta-atom phase response (>400°). Fig. 7 shows the surrogate and EM-simulated meta-atom responses at selected test locations. The agreement between the surrogate and EM-simulated responses is excellent.

Having a trained surrogate model, the optimization is performed according to the procedure of Section III-B. The obtained geometries are $x^{(1)*} = [4.222\ 1.6\ 2.175]^T$,
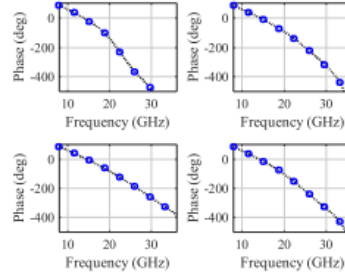

Fig. 7. Performance of the meta-atom surrogate model: EM model (...) and surrogate responses (o) at the selected test locations.
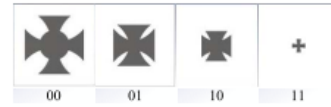

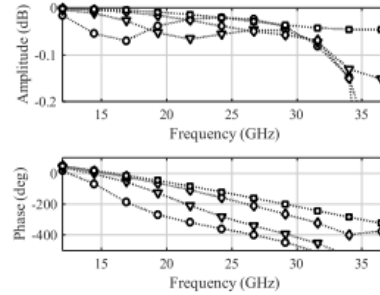Fig. 8. Specific geometries of the globally optimized meta-atoms.

Fig. 9. Reflection performance of the optimized meta-atoms: reflection amplitude (top) and reflection phase (bottom). The responses of "00," "01," "10," and "11" are marked (o), (Δ), (◊), and (□), respectively.

$x^{(2)*} = [3.5\ 1.456\ 0.2]^T$, $x^{(3)*} = [3.5\ 1.022\ 0.2]^T$, and $x^{(4)*} = [10\ 0.422\ 0.2]^T$. Fig. 8 shows the designs, classified as "00," "01," "10," and "11." The reflection amplitude and phase responses of the meta-atoms are shown in Fig. 9. The phase difference characteristics are shown in Fig. 10. Note that the condition (1) is approximately satisfied for the frequencies from 20 to about 35 GHz. Consequently, this frequency range can be anticipated as RCS reduction bandwidth of the entire metasurface.

C. Optimization Results of the Entire Metasurface

Upon finding globally optimum meta-atom designs (cf. Section IV-A), the coding metasurface is characterized. For implementing the entire architecture, the periodic lattices consisting of atoms "00," "01," "10," and "11," are arranged in a uniform manner to realize a diffusive coding metasurface.
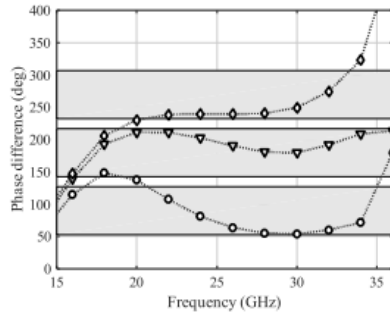
Fig. 10. Reflection phase differences between the optimized meta-atoms. The gray-shaded area indicates the acceptable range according to the condition (1). The differences between atoms "00" and "01," "01" and "10," and "10" and "11" are marked (◯), (△), and (◇), respectively.

Fig. 12. RCS characteristic of the metasurface optimized for 10-dB (top) and 15-dB (bottom) reduction threshold. The simulated responses after the procedure of Section III-B (black) and after final optimization stage (blue) are shown. The red horizontal line represents the target RCS reduction threshold.
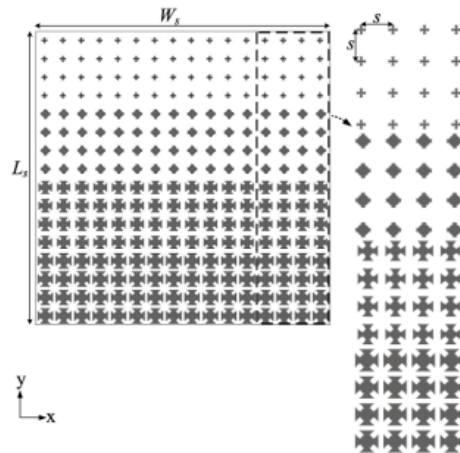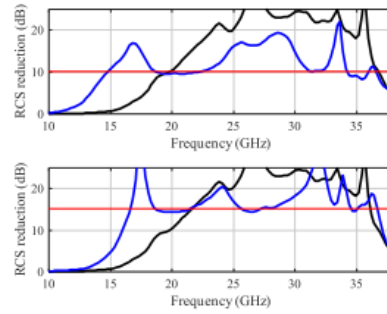

Fig. 11. Configuration of the considered coding metasurface (optimized for 10-dB RCS reduction).

Fig. 11 shows a two-bit coding metasurface comprising sixteen elements: each consisting of four 4×4 periodic lattices of meta-atoms "00," "01," "10," and "11." The overall size of the metasurface is $W_s \times L_s = 96 \times 96$ mm². The interelement spacing of individual meta-atoms in the array is $s = 6$ mm. The structure is implemented on a ground-backed Arlon AD250 lossy substrate ($\varepsilon_r = 2.5$, $h = 1.5$ mm, and $\tan\delta = 0.0018$). To test the RCS performance, an equivalent PEC surface is implemented to be utilized as a reference. The time-domain solver of the CST Microwave Studio is utilized for both the monostatic and bistatic RCS analyses.

At this point, the second optimization stage, i.e., EM-driven local refinement of the entire metasurface, is executed (cf. Section III-C). The availability of a good initial design, determined previously, facilitates gradient-based tuning and allows us to identify globally optimum design at acceptable

computational expenses. Although finding the global optimum is not formally guaranteed by the procedure, it is very likely due to the global optimality of the meta-atom designs, and the fact is that the phase difference properties (2) are reliable estimators of the RCS reduction bandwidth. Furthermore, to demonstrate the utility of adopted two-stage optimization procedure (i.e., efficacy of the initial and versatility of the final stage), we optimized the metasuface design for two levels of RCS reduction, i.e., 10 and 15 dB. This corroborates that following a systematic design procedure (cf. Section III), the structure can be seamlessly optimized as per the designer's needs.

The designs obtained at the final optimization stages for 10- and 15-dB RCS reduction thresholds are $x_A^\star = [3.3978\ 1.6859\ 2.9164\ 3.2022\ 1.4472\ 2.5102\ 5.9794\ 0.8937\ 2.2448\ 8.0707\ 0.7624\ 0.3210]^T$ and $x_B^\star = [4.027\ 1.666\ 1.806\ 2.503\ 1.321\ 3.054\ 7.660\ 0.952\ 2.8401\ 9.504\ 0.810\ 0.240]^T$, respectively.

To quantify the improvement obtained in the final optimization stage, the RCS reduction bandwidth achieved upon EM-based tuning is compared to the performance of the structure implemented using the design identified at the initial optimization stage of Section III-B. As mentioned before, the EM-driven optimization is performed for both 10- and 15-dB RCS reduction levels. The results are shown in Fig. 12. It can be observed that the supervised-learning-based design technique already ensures a broadband RCS reduction performance. Moreover, after executing the final optimization stage, the RCS reduction bandwidth noticeably extends, especially toward the lower frequencies. The bandwidth improvement level in the final optimization stage is in the range of 4–5 GHz. For both design scenarios, the RCS reduction occurs in a broad frequency range, i.e., from 14.8 to 37.2 GHz for 10-dB RCS reduction threshold and from 16.7 to 37 GHz for 15-dB threshold.

For better illustration, the far-field scattering performance of a metallic plate, the metasurface optimized for 10 dB, and the metasurface designed for 15-dB RCS reduction level are presented in Fig. 13. The 3-D scattering field distribution is obtained by far-field simulation of the structure. It can be
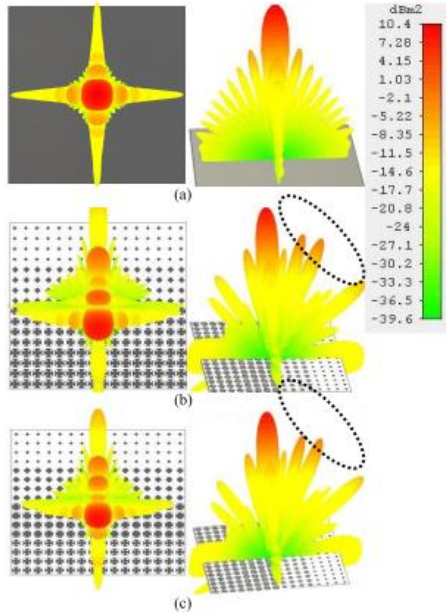
Fig. 13. 3-D scattering performance. (a) PEC surface. Metasurface optimized for (b) 10 dB and (c) 15 dB. The plots correspond to the frequency of 30 GHz.
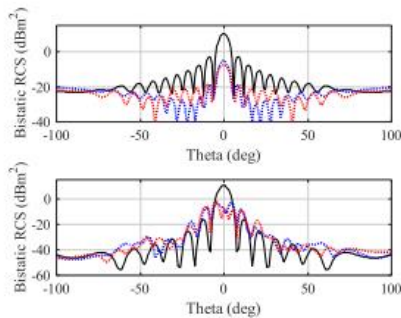

Fig. 14. Bistatic RCS performance at 30 GHz along the principal plane $\phi = 0$ (top) and along the diagonal plane $\phi = 45$ (bottom). The curves corresponding to the design optimized for 10 and 15 dB are marked blue and red, respectively, whereas the black curve indicates the scattered field from the PEC surface.

noticed that the metallic surface causes strong reflections in the boresight direction, in a single lobe, when the plane wave impinges on it. Conversely, the coding metasurface diffuses the incident wave to several directions of the space, which results in a significant reduction of the energy in the vicinity of the scattering peak.

For the sake of supplementary illustration, Fig. 14 shows the bistatic RCS reduction performance of the considered design
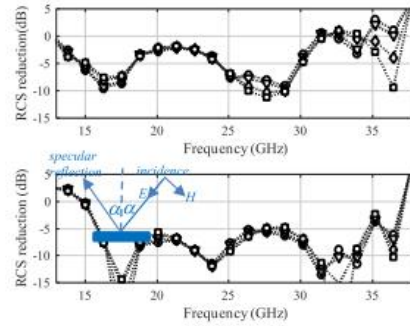

Fig. 15. RCS characteristic in specular directions for 10-dB (top) and 15-dB (bottom) reduction threshold. The responses at $\alpha = 0°$, 30°, 60°, and 90° incident angles are marked ($\bigcirc$), ($\triangle$), ($\Diamond$), and ($\square$), respectively.
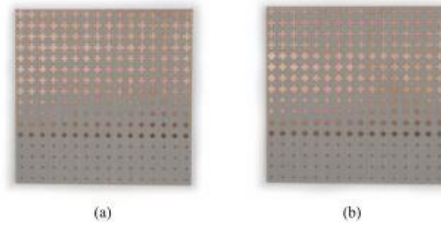

Fig. 16. Photographs of the prototyped metasurfaces: (a) design $x_A^\star$ (optimized for 10-dB RCS reduction level) and (b) design $x_B^\star$ (optimized for 15-dB RCS reduction level).

at two selected planes. As it can be observed, the reduction very much depends on the selection of the plane, i.e., it is increased whenever the plane misses the scattering lobes and deteriorated otherwise. This only indicates that bistatic performance evaluated at a few selected planes is incapable of giving a full account for the metasurface operation, in contrast to what has been fostered in many related works (see [12]).

To further demonstrate the relevance of the considered design, the sensitivity of its RCS performance to oblique incidence angles has been analyzed. Fig. 15 shows the specular reflection performance of a coding metasurface. The monostatic RCS under the oblique plane wave incidence is the RCS in the specular direction [35]. It can be observed from Fig. 15 that when the incident angle α changes from 0°, 30°, 60°, and 90°, the scattering performance remains almost unaltered. This allows us to conclude that the scattering performance of the metasurface is insensitive to the angle of incidence. In other words, the structure exhibits angularly invariant characteristics.

D. Measurement Setup and Experimental Validation

The two designs presented in Section. IV-B have been fabricated and measured to validate the EM simulation results, cf. Fig. 16. Due to limited amenities, the scattering performance of a coding metasurface has only been evaluated in
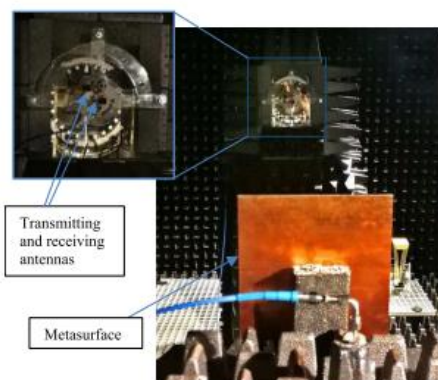
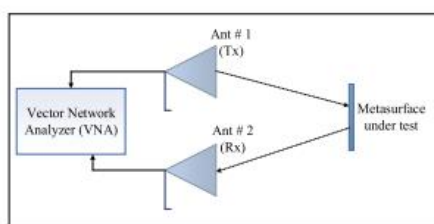Fig. 17. Measurement setup at Reykjavik University.

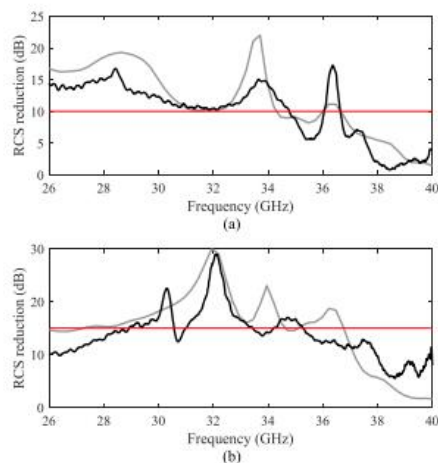Fig. 18. Block diagram of the measurement environment.

Fig. 19. Measured (black) and simulated (gray) RCS reduction performance comparison for (a) 10- and (b) 15-dB optimized design. The red curve indicates 10- and 15-dB RCS reduction threshold.

TABLE I
CONSIDERED METASURFACE VERSUS STATE-OF-THE-ART DESIGNS

Design	Frequency range (>10-dB RCS reduction) (GHz)	Frequency range (>15-dB RCS reduction) (GHz)	Multiple diffuse scattering (multi-bit)	Angle insensitivity
[20]	7.5–15	8.8–9.1	yes	not studied
[23]	11.95–18.36	12.5–18.2	yes	not studied
[36]	3.75–10	6.5–7.5	no	yes
[37]	8.6–10.7	9.1–10.2	no	yes
[38]	9.7–18.12	11.2–17.1	yes	not studied
[39]	8.8–11	none	yes	not studied
[40]	3.88–4.07	3.95–4.0	no	not studied
[41]	7.98–16.32	9.7–14.5	no	yes
[42]	6.94–9.23	7.2–9.1	yes	yes
[15]	17–42	22–28	no	yes
[16]	5.4–7.4	5.6–6.8	no	yes
This work	14.8–37.2	16.7–37	yes	yes

terms of reflectivity using an equivalent metallic surface as a reference to quantify the RCS reduction.

The experimental measurements have been carried out in the anechoic chamber of Reykjavik University and the setup is presented in Fig. 17. The latter consists of a vector network analyzer (VNA) and the two linearly polarized horn antennas (PE9850/2F-15), utilized as the transmitter and the receiver, respectively. The two antennas are positioned perpendicular to the surface under test to realize the normal incidence of the impinging waves and resultant reception of the reflected waves. The distance between the device under test and the antennas is selected to ensure operating in the far-field regime. The schematic of the experimental setup is given in Fig. 18. The scattering performance of the coding metasurface and the corresponding metallic surface is evaluated by measuring the transmission coefficient, captured by the VNA.

The comparison between the measurements and the simulation results is shown in Fig. 19. A decent agreement between the two datasets can be observed. Slight differences can be attributed to several factors. Amidst, the spatial misalignment of the transmitting and receiving antennas with respect to structure under test contributes predominantly. Needless to say, the proper orientation of a surface (realized manually) is a challenging endeavor. A slight misalignment here may lead to considerable discrepancies. However, the measurement data confirm the RCS reduction bandwidth obtained through EM

simulation for both 10- and 15-dB thresholds in the frequency range of 26.5 and 40 GHz. The measurement frequency range is limited by the available hardware. The above findings allow us to conclude that the coding metasurface developed using our algorithmic framework features low observable property in a broad frequency range, and therefore, it has the potential to replace the metallic surfaces in applications where high stealthiness is essential.

E. Benchmarking

The coding metasurface discussed in this work has been benchmarked against the state-of-the-art structures from the

literature. The comparison is carried out in terms of RCS reduction bandwidth, the level of reduction, and the scattering performance in specular directions. The results are given in Table I. As indicated, the design developed using the proposed algorithmic tools clearly outperforms other structures (based upon multiple diffusive scattering) in terms of RCS reduction bandwidth and level of RCS reduction. Furthermore, our design is competitive to similar structures (based upon single-bit coding scheme) in terms of all of the considered performance figures. In addition, our design covers two major radar frequency bands K and Ka, as well as a part of the Ku-band. Therefore, it has the potential to surpass other structures proposed for stealth applications.

V. Conclusion

This article presents the algorithmic approach developed for global optimization of multibit coding metasurfaces. The adopted optimization framework offers new ways of controlling the peak RCS reduction threshold, as well as enable broadband RCS reduction. The metasurface is characterized by a two-bit coding scheme, i.e., it consists of four unique meta-atom geometries denoted as "00," "01," "10," and "11" binary codes, each representing the phase reflection states of 0, $\pi/2$, π, and $3\pi/2$, respectively.

A rigorous design approach, combining global surrogate-assisted optimization of meta-atoms and EM-driven tuning of the entire metasurface, turns out to be critical to achieve the aforementioned level of performance. A supervised-learning-based technique is initially employed to determine globally optimum meta-atom designs, subsequently used as the building blocks of the coding metasurface. The former involves a fast surrogate model that facilitates exploration of the parameter space, otherwise prohibitive due to a massive number of expensive EM-simulations involved. Still, a concurrent optimization of four meta-atoms entails combinatorial explosion, which hinders the utilization of the standard global exploration techniques. A sequential-search strategy has been developed specifically to address this issue. The final stage involves direct EM-driven optimization of the entire structure, oriented toward maximization of the RCS reduction bandwidth. The structure has been optimized for two levels of RCS reduction, i.e., 10 and 15 dB. The performance of the metasurface design considered as an illustration example is investigated using monostatic and bistatic scattering properties, indicating that the RCS reduction is realized in a broad frequency range, i.e., from 14.8 to 37.2 GHz for 10-dB RCS reduction level and from 16.7 to 37 GHz for 15-dB level. The prototypes have been fabricated to corroborate the simulation results. A good agreement between the two datasets has been observed. Both structures have been benchmarked against state-of-the-art designs and demonstrated to be superior in terms of the RCS reduction bandwidth and the level of RCS reduction.

Acknowledgment

References

[1] G. A. Rao and S. P. Mahulikar, "Integrated review of stealth technology and its role in airpower," *Aeronaut. J.*, vol. 106, no. 1066, pp. 629–642, Dec. 2002.

[2] E. F. Knott, *Radar Cross Section Measurements*. Cham, Switzerland: Springer, 2012, pp. 12–36.

[3] P. Westwick, *Stealth: The Secret Contest to Invent Invisible Aircraft*. London, U.K.: Oxford Univ. Press, 2019, pp. 5–42.

[4] T. A. Khan, J. X. Li, Z. Li, M. Abdullah, J. Chen, and A. X. Zhang, "Design of Vivaldi antenna with wideband reduced radar cross section," *AEU Int. J. Electron. Commun.*, vol. 95, pp. 47–51, Oct. 2018.

[5] T. J. Cui, D. R. Smith, and R. Liu, *Metamaterials Theory, Design, and Applications*. New York, NY, USA: Springer, 2010.

[6] N. I. Landy, S. Sajuyigbe, J. J. Mock, D. R. Smith, and W. J. Padilla, "Perfect metamaterial absorber," *Phys. Rev. Lett.*, vol. 100, no. 20, pp. 207–402, 2008.

[7] F. Costa, A. Monorchio, and G. Manara, "Analysis and design of ultra thin electromagnetic absorbers comprising resistively loaded high impedance surfaces," *IEEE Trans. Antennas Propag.*, vol. 58, no. 5, pp. 1551–1558, May 2010.

[8] Y. Liu and X. Zhao, "Perfect absorber metamaterial for designing low-RCS patch antenna," *IEEE Antennas Wireless Propag. Lett.*, vol. 13, pp. 1473–1476, 2014.

[9] N. Yu *et al.*, "Light propagation with phase discontinuities: Generalized laws of reflection and refraction," *Science*, vol. 334, no. 6054, pp. 333–337, Oct. 2011.

[10] X. Gao, X. Han, W.-P. Cao, H. O. Li, H. F. Ma, and T. J. Cui, "Ultrawide-band and high-efficiency linear polarization converter based on double V-shaped metasurface," *IEEE Trans. Antennas Propag.*, vol. 63, no. 8, pp. 3522–3530, Aug. 2015.

[11] M. Paquay, J.-C. Iriarte, I. Ederra, R. Gonzalo, and P. de Maagt, "Thin AMC structure for radar cross-section reduction," *IEEE Trans. Antennas Propag.*, vol. 55, no. 12, pp. 3630–3638, Dec. 2007.

[12] J. C. Iriarte Galarregui, A. Tellechea Pereda, J. L. M. de Falcon, I. Ederra, R. Gonzalo, and P. de Maagt, "Broadband radar cross-section reduction using AMC technology," *IEEE Trans. Antennas Propag.*, vol. 61, no. 12, pp. 6136–6143, Dec. 2013.

[13] W. Chen, C. A. Balanis, and C. R. Birtcher, "Checkerboard EBG surfaces for wideband radar cross section reduction," *IEEE Trans. Antennas Propag.*, vol. 63, no. 6, pp. 2636–2645, Jun. 2015.

[14] K. Wang, J. Zhao, Q. Cheng, D. S. Dong, and T. J. Cui, "Broadband and broad-angle low-scattering metasurface based on hybrid optimization algorithm," *Sci. Rep.*, vol. 4, no. 1, May 2015, Art. no. 5935.

[15] H. Sun *et al.*, "Broadband and broad-angle polarization-independent metasurface for radar cross section reduction," *Sci. Rep.*, vol. 7, no. 1, Jan. 2017, Art. no. 40778.

[16] X. Liu, J. Gao, L. Xu, X. Cao, Y. Zhao, and S. Li, "A coding diffuse metasurface for RCS reduction," *IEEE Antennas Wireless Propag. Lett.*, vol. 16, pp. 724–727, May 2017.

[17] S. Sui *et al.*, "Absorptive coding metasurface for further radar cross section reduction," *J. Phys. D, Appl. Phys.*, vol. 51, no. 6, Feb. 2018, Art. no. 065603.

[18] Y. Zhao *et al.*, "Broadband diffusion metasurface based on a single anisotropic element and optimized by the simulated annealing algorithm," *Sci. Rep.*, vol. 6, no. 1, Jul. 2016, Art. no. 23896.

[19] L. Ali, Q. Li, T. A. Khan, J. Yi, and X. Chen, "Wideband RCS reduction using coding diffusion metasurface," *Materials*, vol. 12, no. 17, p. 2708, Aug. 2019.

[20] T. J. Cui, M. Q. Qi, X. Wan, J. Zhao, and Q. Cheng, "Coding metamaterials, digital metamaterials and programmable metamaterials," *Light, Sci. Appl.*, vol. 3, no. 10, Oct. 2014, Art. no. 218.

[21] L. Liang *et al.*, "Broadband and wide-angle RCS reduction using a 2-bit coding ultrathin metasurface at terahertz frequencies," *Sci. Rep.*, vol. 6, no. 1, Dec. 2016, Art. no. 39252.

[22] C. Huang, B. Sun, W. Pan, J. Cui, X. Wu, and X. Luo, "Dynamical beam manipulation based on 2-bit digitally-controlled coding metasurface," *Sci. Rep.*, vol. 7, no. 1, Sep. 2017, Art. no. 42302.

[23] M. Feng *et al.*, "Two-dimensional coding phase gradient metasurface for RCS reduction," *J. Phys. D, Appl. Phys.*, vol. 51, Aug. 2018, Art. no. 375103.

[24] S. Koziel and A. Pietrenko-Dabrowska, "Efficient gradient-based algorithm with numerical derivatives for expedited optimization of multi-parameter miniaturized impedance matching transformers," *Radioengineering*, vol. 27, no. 3, pp. 572–578, Sep. 2019.

[25] T. W. Simpson, J. D. Poplinski, P. N. Koch, and J. K. Allen, "Meta-models for computer-based engineering design: Survey and recommendations," *Eng. Comput.*, vol. 17, no. 2, pp. 129–150, Jul. 2001.

[26] S. Koziel, L. Leifsson, and X. S. Yang, "Surrogate-based optimization," in *Simulation-Driven Design Optimization and Modeling for Microwave Engineering*, S. Koziel, X. S. Yang, and Q. J. Zhang, Eds. London, U.K.: Imperial College Press, 2012, pp. 41–80.

[27] S. Koziel and J. W. Bandler, "Reliable microwave modeling by means of variable-fidelity response features," *IEEE Trans. Microw. Theory Techn.*, vol. 63, no. 12, pp. 4247–4254, Dec. 2015.

[28] S. Koziel and A. Pietrenko-Dabrowska, *Performance-Driven Surrogate Modeling of High-Frequency Structures*. New York, NY, USA: Springer, 2020.

[29] F. Feng *et al.*, "Multifeature-assisted neuro-transfer function surrogate-based EM optimization exploiting trust-region algorithms for microwave filter design," *IEEE Trans. Microw. Theory Techn.*, vol. 68, no. 2, pp. 531–542, Feb. 2020.

[30] X. Chen, W. Xue, H. Shi, J. Yi, and W. E. I. Sha, "Orbital angular momentum multiplexing in highly reverberant environments," *IEEE Microw. Wireless Compon. Lett.*, vol. 30, no. 1, pp. 112–115, Jan. 2020.

[31] S. Koziel and A. Pietrenko-Dabrowska, "Expedited optimization of antenna input characteristics with adaptive Broyden updates," *Eng. Comput.*, vol. 37, no. 3, pp. 851–862, Sep. 2019.

[32] S. Koziel and M. Abdullah, "Machine-learning-powered EM-based framework for efficient and reliable design of low scattering metasurfaces," *IEEE Trans. Microw. Theory Techn.*, vol. 69, no. 4, pp. 2028–2041, Apr. 2021.

[33] A. R. Conn, N. I. M. Gould, and P. L. Toint, *Trust Region Methods* (MPS-SIAM Series on Optimization). Philadelphia, PA, USA: Society for Industrial and Applied Mathematics, 2000.

[34] S. Koziel, J. W. Bandler, and Q. S. Cheng, "Robust trust-region space-mapping algorithms for microwave design optimization," *IEEE Trans. Microw. Theory Techn.*, vol. 58, no. 8, pp. 2166–2174, Aug. 2010.

[35] Y. Zhuang *et al.*, "Random combinatorial gradient metasurface for broadband, wide-angle and polarization-independent diffusion scattering," *Sci. Rep.*, vol. 7, no. 1, pp. 1–10, Dec. 2017.

[36] A. Y. Modi, C. A. Balanis, C. R. Birtcher, and H. N. Shaman, "Novel design of ultrabroadband radar cross section reduction surfaces using artificial magnetic conductors," *IEEE Trans. Antennas Propag.*, vol. 65, no. 10, pp. 5406–5417, Oct. 2017.

[37] Y. Zhuang, G. Wang, J. Liang, T. Cai, W. Guo, and Q. Zhang, "Flexible and polarization-controllable diffusion metasurface with optical transparency," *J. Phys. D, Appl. Phys.*, vol. 50, no. 46, Nov. 2017, Art. no. 465102.

[38] Q. Zheng *et al.*, "Wideband, wide-angle coding phase gradient metasurfaces based on pancharatnam-berry phase," *Sci. Rep.*, vol. 7, no. 1, Apr. 2017, Art. no. 43543.

[39] Y. Zhuang, G. Wang, T. Cai, and Q. Zhang, "Design of bifunctional metasurface based on independent control of transmission and reflection," *Opt. Exp.*, vol. 26, no. 3, pp. 3594–3603, Feb. 2018.

[40] L. Shao, M. Premaratne, and W. Zhu, "Dual-functional coding metasurfaces made of anisotropic all-dielectric resonators," *IEEE Access*, vol. 7, pp. 45716–45722, 2019.

[41] S. H. Kim and Y. J. Yoon, "Wideband radar cross-section reduction on checkerboard metasurfaces with surface wave suppression," *IEEE Antennas Wireless Propag. Lett.*, vol. 18, no. 5, pp. 896–900, May 2019.

[42] X. Han *et al.*, "Multiple diffuse coding metasurface of independent polarization for RCS reduction," *IEEE Access*, vol. 8, pp. 162313–162321, 2020.
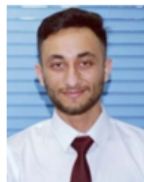
Muhammad Abdullah received the B.Sc. degree from the University of Engineering and Technology, Lahore, Pakistan, in 2016, and the M.Sc. degree from Xi'an Jiaotong University (XJTU), Xi'an, China, in 2019.

Since late 2019, he has been with the Department of Engineering, Reykjavik University, Reykjavik, Iceland, as a Researcher. From 2018 to 2019, he was with the Electromagnetics and Communication Laboratory, XJTU. His broader research interests include surrogate-based modeling and optimization, CAD and modeling of antennas and other high-frequency structures, MIMO antennas, simulation-driven design, and machine-learning techniques.

Mr. Abdullah received the excellent master's thesis award on completion of the M.Sc. degree.

Slawomir Koziel (Senior Member, IEEE) received the M.Sc. and Ph.D. degrees in electronic engineering from the Gdansk University of Technology, Gdansk, Poland, in 1995 and 2000, respectively, and the M.Sc. degrees in theoretical physics and mathematics and the Ph.D. degree in mathematics from the University of Gdansk, Gdansk, in 2000, 2002, and 2003, respectively.

He is currently a Professor with the Department of Engineering, Reykjavik University, Reykjavik, Iceland. His research interests include CAD and modeling of microwave and antenna structures, simulation-driven design, surrogate-based optimization, space mapping, circuit theory, analog signal processing, evolutionary computation, and numerical analysis.

Chapter 6

6 Paper # 4

Slawomir Koziel, Muhammad Abdullah, and Stanislaw Szczepanski

Design of High-Performance Scattering Metasurfaces through Optimization-Based Explicit RCS Reduction

Design of High-Performance Scattering Metasurfaces Through Optimization-Based Explicit RCS Reduction

SLAWOMIR KOZIEL [1,2], (Senior Member, IEEE), **MUHAMMAD ABDULLAH** [1], **AND STANISLAW SZCZEPANSKI** [2]

[1]Engineering Optimization and Modeling Center, Reykjavik University, 101 Reykjavik, Iceland
[2]Faculty of Electronics, Telecommunications and Informatics, Gdańsk University of Technology, 80-233 Gdańsk, Poland

Corresponding author: Slawomir Koziel (koziel@ru.is)

ABSTRACT The recent advances in the development of coding metasurfaces created new opportunities in realization of radar cross section (RCS) reduction. Metasurfaces, composed of optimized geometries of meta-atoms arranged as periodic lattices, are devised to obtain desired electromagnetic (EM) scattering characteristics. Despite potential benefits, their rigorous design methodologies are still lacking, especially in the context of controlling the EM wavefront through parameter tuning of meta-atoms. One of the practical obstacles hindering efficient design of metasurfaces is implicit handling of RCS performance. To achieve essential RCS reduction, the design task is normally formulated in terms of phase reflection characteristics of the meta-atoms, whereas their reflection amplitudes—although contributing to the overall performance of the structure—is largely ignored. As a result, the conventional approaches are unable to determine truly optimum solutions. This article proposes a novel formulation of the metasurface design task with explicit handling of RCS reduction at the level of meta-atoms. Our methodology accounts for both the phase and reflection amplitudes of the unit cells. The design objective is defined to directly optimize the RCS reduction bandwidth at the specified level (e.g., 10 dB) w.r.t. the metallic surface. The benefits of the presented scheme are twofold: (i) it provides a reliable insight into the metasurface properties even though the design process is carried out at the level of meta-atoms, (ii) the obtained design requires minimum amount of tuning at the level of the entire metasurface. None of these is possible for phase-response-based approach fostered in the literature. For practical purposes, the design is conducted using a surrogate-assisted procedure involving kriging metamodels, which enables global optimization at a low computational cost. To corroborate the utility of our formulation, a high-performance metasurface incorporating crusader-cross-shaped meta-atoms has been developed. The obtained results indicate that the system characteristics predicted at the design stage are well aligned with those of the EM-simulated structure (which is not the case for the traditional design approach). The metasurface features 10-dB RCS reduction in the frequency range of 16.5 GHz to 34.6 GHz, as validated both numerically and experimentally.

INDEX TERMS Radar cross section (RCS), periodic structures, design task, optimization, scattering.

I. INTRODUCTION

With the rapid advances in the field of radar detection technology, maintaining low observability of the aircraft has become a primary concern of research within the stealth

The associate editor coordinating the review of this manuscript and approving it for publication was Guido Valerio.

technology [1], [2]. The standard radar cross section (RCS) reduction methods are based on the shape and material stealth [3], [4]. The former has a critical impact on the aerodynamic operation and structural integrity of the aircraft, whereas the latter is affected by the supplemented weight, thickness, and cost, resulting in the inability of the method to meet a variety of stealth needs. To circumvent the aforesaid

limitations, artificially engineered materials, or metamaterials, are being incorporated as alternatives to the conventional stealth methods.

Metasurfaces, two-dimensional equivalents of metamaterials, are planar patterned structures composed of periodic lattices of meta-atoms (also referred to as unit cells) [5]. Owing to their unique abilities to control the electromagnetic (EM) wavefront, the utilization of metasurfaces in the field of stealth technology has been steadily growing [6]. Traditionally, metasurfaces capitalize on two EM mechanisms to realize RCS reduction, i.e., absorbing the incident energy [7]–[9], and scattering the energy into other directions (i.e., away from the direction of incidence) [10]–[13]. The operation of the absorbing metasurfaces is based on the concept of converting the EM energy into heat and dissipating it. On the other hand, the scattering metasurfaces adjust the spatial distribution of the backscattered EM energy by adjusting the unit cell geometry, and, therefore, control the scattering properties of the structure. Therein, the aim is to scatter the incident EM wave into a single abnormal direction. At the same time, the weight, thickness and losses of the metasurfaces can be maintained below a practically acceptable level. Nevertheless, absorbing metasurfaces are susceptible to infrared detectors, which predominantly increases their detection probability. Likewise, the single-beam scattering metasurfaces only ensure RCS reduction in a monostatic configuration; however, they are not effective to reduce bistatic RCS.

Recently, the idea of scattering manipulation has been extended to implement checkerboard metasurfaces [14], [15], which offer a control over the wavefront in a more sophisticated manner. In a checkerboard-type surfaces, the two distinct meta-atom designs are employed in an alternate arrangement, where two atoms represent two phase states (0 and π) to obtain RCS reduction [14]. Notwithstanding, such architectures allow for scattering a limited number of beams towards fixed propagation directions, which limits their widespread utility. Another effort in this endeavor is the introduction of coding metasurfaces [16], [17], and diffusion metasurfaces [18], [19]. The primary advantage of coding and diffusion metasurfaces over the checkerboard type surfaces is in their capability of scattering the incident EM waves into all directions, as opposed to a few fixed propagation directions. In addition to that, coding metasurfaces are also being exploited as an absorptive surface to realize essential RCS reduction [20]. In a related vein, the concept of programmable metasurfaces [21], Huygens' metasurfaces [22], and cloaking structures [23], have also been proposed to accomplish RCS reduction.

The development of scattering metasurfaces involves handling of individual meta-atom designs, and their concurrent geometry parameters adjustment. However, the lack of efficient (presumably global) techniques to optimize individual meta-atoms under relevant constraints, as well as the entire structure, limits the performance of metasurfaces, in particular, their RCS reduction bandwidth, and the level

of the reduction peak. Therein, the primary obstacle hindering efficient design of metasurfaces is implicit handling of RCS performance. To achieve essential RCS reduction, the design task is typically formulated in terms of phase reflection characteristics of the meta-atoms. More specifically, it has been argued in the literature that 10 dB RCS reduction can be maintained over a frequency band if the phase difference between the two meta-atoms remains within the 180° ± 37° range [14], [15]. On the other hand, their reflection amplitudes—although contributing to the overall performance of the structure—is predominantly ignored. The work [24] presents an optimization framework for metasurfaces based on surrogate models, where the optimization formulation accounts for both the amplitude and phase of the field, however, it is silent on the RCS reduction properties of metasurfaces. As a result, the conventional approaches are unable to determine truly optimum solutions, nor to account for the relationship between the meta-atom geometry and the RCS characteristics of the metasurface. In pursuit of these, a novel formulation of the metasurface design task with explicit handling of RCS reduction at the level of meta-atoms is required. At this point, it should be emphasized that highly non-linear input-output relationships between design variables and the system responses hinders utilization of conventional optimization methods. On the one hand, the advancements in high-performance computing, both in terms of hardware and software, have resulted in more widespread use of simulation-based design procedures, principally based on rigorous numerical optimization [25]. On the other hand, direct optimization of complex structures using conventional algorithms may be prohibitively expensive, especially whenever global exploration is needed. A practical solution might be a utilization of data-driven surrogates [26], involving metamodeling [27]–[29]. Recently, data-driven techniques have been applied in many areas of science and engineering [31]–[33]. Furthermore, topology optimization has been considered as generalization of parametric optimization of the meta-atoms (and, consequently, the metasurface). Therein, the entire geometry of the structure is subject to the optimization process, which brings in additional degrees of freedom. This type of tasks is often handled using inverse modeling methods (e.g., [34], [35]).

To circumvent the implicit handling of RCS characteristics in the development of scattering metasurfaces, this article proposes a novel formulation of the metasurface design task with explicit handling of RCS reduction at the level of meta-atoms. According to our approach, both phase and reflection amplitudes of the unit cells are accounted for. The design objective is defined to directly optimize the RCS reduction bandwidth at the specified level (e.g., 10 dB) with the reference to the metallic surface. Our approach offers a reliable insight into the metasurface properties even though the design process is implemented at the level of meta-atoms. Moreover, the RCS characteristics rendered through optimization of the meta-atoms is in close resemblance to that of the entire metasurface. Hence, the latter only requires slight adjustment,

which reduces the overall computational cost of the design process. To ensure globally optimum metasurface design, the design is executed using surrogate-assisted procedure involving kriging metamodels. The practical utility of our formulation is corroborated by developing a high-performance coding metasurface including crusader-cross-shaped meta-atoms. The obtained results indicate that the system characteristics predicted at the design stage are well aligned with those of the EM-simulated structure (which is not the case for the traditional design approach). The designed metasurface features 10-dB RCS reduction in the frequency range of 16.5 GHz to 34.6 GHz, as validated both numerically and experimentally.

The technical novelty and major contributions of this article can be summarized as follows: (i) proposing a novel metasurface design task formulation with explicit handling of RCS reduction at the level of meta-atoms; (ii) corroborating the efficacy of the approach, as well as demonstrating its practical utility in the context of scattering metasurface design and optimization, and (iii) designing a high-performance coding metasurface for broadband RCS reduction by applying the proposed formulation. It should be emphasized that the presented design task formulation scheme is—to the authors best knowledge—the first endeavor in the literature to explicitly handle RCS reduction at the level of meta-atoms, which is indispensable in the development of high-quality metasurface designs.

The remaining part of the paper is organized as follows. In Section II, we described the standard metasurface design task formulations, and, subsequently, introduced the proposed approach. This is followed by an exposition of the complete optimization procedure. Section III discusses the modeling and optimization results, as well as the demonstration of the practical utility of the presented formulation through the design of a high-performance coding metasurface. The benefits of the proposed and the standard methodologies are also highlighted. Section IV provides experimental validation of the considered metasurface design, and Section V concludes the paper.

II. DESIGN PROBLEM FORMULATION AND OPTIMIZATION METHODOLOGY

This section provides a description of the standard metasurface design task formulation. Subsequently, a novel formulation is introduced. A surrogate-assisted optimization procedure involving kriging metamodels and simulation-based refinement is also outlined. The procedure is tailored to solve the metasurface optimization problem in a global sense and computationally efficient manner. Application of the proposed approach to a coding metasurface design will be presented in Section III.

A. METASURFACE DESIGN: STANDARD FORMULATION

The design task of a scattering metasurface is typically formulated to find a pair of meta-atom designs providing the phase difference that remains within the range of 180° ±37° over possibly broad frequency range F, as suggested in [14].

The vectors of designable variables for a pair of meta-atoms will be denoted as $x_1 = [x_{1.1} \ldots x_{1.n}]^T \in X_1$ and $x_2 = [x_{2.1} \ldots x_{2.n}]^T \in X_2$, with X_1 and X_2 being the parameter spaces of the meta-atoms. Here, for notational simplicity the dimensionalities of both spaces are assumed to be the same; generalization for different dimensionalities is straightforward. Their phase reflection responses are $R_{P1}(x_1)$ and $R_{P2}(x_2)$, respectively. The objective is to find a pair of unit cell designs $x_p^* = [(x_1^*)^T (x_2^*)^T]^T$ maximizing the frequency range for which the phase difference $\Delta R_P(x_p) = R_{P1}(x_1) - R_{P2}(x_2)$ satisfies the condition

$$180° - -37° \leq \Delta R_P([(x_1^*)^T (x_2^*)^T]^T) \leq 180° + 37° \quad (1)$$

Analytically, the design task can be formulated as follows:

$$x_p^* = \arg \min_{x_p \in X_1 \times X_2} U(\Delta R_P(x_p)) \quad (2)$$

and the objective function U is defined as

$$U(\Delta R_P(x_p)) = -[f_U(x_p) - f_L(x_p)] \quad (3)$$

where f_U and f_L are the upper and lower frequencies, respectively, defining the largest continuous range of frequencies for which the condition (1) is satisfied.

It should be emphasized that the standard design task of a scattering metasufrace is merely formulated in terms of the phase reflection characteristics of the meta-atoms. The reflection amplitudes of the two atoms are implicitly assumed to be identical and equal to one. In practical implementations, these neither equal to each other nor equal to unity. Because the reflection amplitudes are contributing to the overall performance of the structure, the standard formulation fails to adequately represent the metasurface properties.

In summary, the three major issues associated with coding metasurface design based on phase reflection responses are:

- The design problem is defined over an intermediate functional space (i.e., phase characteristics rather than RCS responses). Consequently, the design found by solving (1)-(3) cannot be optimum with respect to the ultimate target, which is the RCS reduction bandwidth at the specified level (e.g., 10 dB);
- Neglecting the reflection amplitudes seriously limits the reliability of the design process.
- Handling phase characteristics does not give a proper account for the RCS performance, in particular, the RCS reduction characteristic does not have a direct counterpart at the level of unit cell (meta-atom) performance.

Addressing these issues entails the development of a novel formulation of the metasurface design task with explicit handling of RCS reduction. This will be proposed in the next section below.

B. NOVEL METASURFACE DESIGN TASK FORMULATION

As indicated in Section II. *A*, the implicit handling of RCS characteristics leads to serious issues concerning the reliability of the metasurface design process. To circumvent these,

this work proposes a novel design task formulation with explicit handling of RCS reduction at the level of meta-atoms. Our approach accounts for both the reflection phases and amplitudes of the unit cells.

As indicated in [20], the RCS σ_S of a one-bit coding metasurface at a frequency f can be approximated as

$$\sigma_S(f) = 20 \log \left| \frac{A_1(f)e^{iP_1(f)} + A_2(f)e^{iP_2(f)}}{2} \right| \quad (4)$$

where A_1, A_2 and P_1, P_2 are the reflection amplitude and phase responses of a pair of meta-atom designs, respectively. In the standard formulation, the reflection amplitudes of the two atoms are assumed to be unity. Note that the amplitudes and phases are functions of the respective meta-atom parameter vectors, i.e., we have $A_1(f, x_1)$, $P_1(f, x_1)$, and $A_2(f, x_2)$, $P_2(f, x_2)$; consequently, we get $\sigma_S(f, x_p)$.

In a similar way, the RCS reduction σ_R, of a corresponding metasurface with the reference to the equivalent metallic surface can be obtained as

$$\sigma_R(f, x_p) = \sigma_S(f, x_p) - \sigma_P(f, x_p) \quad (5)$$

where σ_P is the RCS of an metallic surface. Using (4) and (5), in this work, the coding metsurface design task is defined to directly handle the RCS characteristics by solving

$$x_p^* = \arg \min_{x_p \in X_1 \times X_2} U(\sigma_R(f, x_p)) \quad (6)$$

with the objective function U given as

$$U(\sigma_R(f, x_p)) = - \left[f_{\sigma U}(x_p) - f_{\sigma L}(x_p) \right] \quad (7)$$

where $f_{\sigma U}$ and $f_{\sigma L}$ stand for the upper and lower frequencies defining the broadest continuous frequency range of frequencies for which $U(\sigma_R(x_p))$ is above a specified target threshold (e.g., 10 dB). The negative sign in (7) transforms the maximization task into the minimization problem. In our formulation of objective function, reflection response of a given meta-atoms is obtained through EM-simulation of the unit cells. Again, the proposed design task directly optimizes the RCS reduction bandwidth at the specified level (e.g., $\sigma_{Rmax} = 10$ dB) w.r.t. the metallic surface.

C. SURROGATE-ASSISTED OPTIMIZATION PROCEDURE

In practice, the design task formulated in Section II. *B* needs to be solved in a global sense because typical meta-atom geometries offer considerable flexibility. Consequently, identification of the region containing the optimum design is a non-trivial problem, which cannot be solved using local procedures. At the same time, direct handling of (6) at the level of EM simulation models (using, e.g., nature-inspired algorithms [36]) is normally prohibitive. In particular, vast majority of global optimization methods involve population-based nature-inspired algorithms, which process sets of candidate solutions with typical numbers of objective function evaluations from many hundreds to thousands. At the same time, metaheuristic algorithms exhibit limited repeatability of

solutions (due to stochastic components presents therein), and high dependence on the control parameter setup.

Here, in order to solve (6) in a computationally feasible manner, a surrogate-assisted procedure involving kriging metamodels [26] is applied. In this work, the surrogate is understood as a fast replacement model, which is used in place of expensive EM simulations to speed up the optimization procedures. The surrogate is constructed to predict the responses (e.g., frequency characteristics) of the system under design as a function of its designable (here, geometry) parameters so that the predictions are possibly close to those obtained using simulation. At the same time, the evaluation time of the surrogate should be considerably lower than for EM analysis.

In the global optimization process, massive references to EM analysis of the meta-atoms are replaced by the utilization of fast surrogates, here, implemented by means of kriging interpolation [26]. Kriging is a popular data-driven approach combining low-order polynomial regression with stochastic modeling or the residuals between the trend function and the training data in the form of a linear combination of basis functions controlled by a set of scaling factors (hyperparameters) [26]. Due to low-dimensionality of the parameter space (typically meta-atom geometries feature up to three or four parameters), rendering accurate surrogates within the entire parameter space of interest is computationally feasible. The acquisition of the training data is accomplished by allocating samples within X_1 and X_2, both defined by the lower and upper bounds $l_i = [l_{i,1} \ldots l_{i,n}]^T$ and $u_i = [u_{i,1} \ldots u_{i,n}]^T$ such that $l_{i,l} \leq x_{i,l} \leq u_{i,l}$, $l = 1, \ldots, n$ and $i = 1, 2$. The EM model is evaluated to obtain the corresponding reflection amplitude and phase responses. The metamodels representing these responses will be denoted as S_A and S_P, and are constructed using the data samples $\{x^{(k)}, R(x^{(k)})\}_{k=1,\ldots,Ni}$, where $R_i(x_{i(k)})$ denotes the EM-simulated reflection response (both the amplitude and phase) of the kth meta-atom, and N_i denotes the total number of training samples, respectively. Here, the samples are distributed on a rectangular grid and the number of grid nodes along each direction is decided by a large-scale sensitivity analysis. This design of experiments strategy is suitable for low dimensional problems. The kriging model is set up using a first-order polynomial as a trend function, and a Gaussian correlation function. The large-scale sensitivity analysis is understood here as verifying the variability of the meta atom responses when varying individual geometry parameters from their lower to upper bounds (with the remaining parameters set to the center of the domain). This gives a good idea of the sensitivity of the system characteristics with respect to particular variables across the parameter space.

Having the metamodels, the first step of the optimization process is a global, grid-constrained exhaustive search. This is followed by a local refinement, which allows us to determine the parameter vector minimizing the objective function (7), thus maximizing the RCS reduction bandwidth at the specified level σ_{Rmax}.

The grid-confined global exploration is implemented as follows. Let $M_{m1...mn}$ be a rectangular grid defined as $x \in M_{m1...mn}$ if and only if $x = [x_1 ... x_n]^T$ conform to $x_k = l_k + j_k[(u_k - l_k)/m_k]$, where $k = 1, ..., n$, m_k is a grid-defining integer for the kth variable, and $j_k \in \{0, 1, ..., m_k\}$. The exhaustive search solves

$$x_p^{(0)} = \arg \min_{x^{(1)}, x^{(2)} \in M_{m1...mn}} U(\sigma_R(f, [(x^{(1)})^T (x^{(2)})^T])) \quad (8)$$

In the above, to maintain the simplicity of notation, the grids for both meta-atoms are assumed to be identical. The optimum design $x_p^{(0)}$ is further adjusted using the standard gradient-based algorithm [36], again at the level of the metamodels. This is to improve the resolution beyond the initial grid $M_{m1...mn}$. The computational cost of the entire optimization procedure is low, considering the fact that it is executed at the level of fast surrogates. Additionally, the search process is vectorized to further expedite its operation. Although the computational cost is front-loaded with the acquisition of the training data required by metamodel construction, it is inevitable to render the aforementioned computational benefits, and to enable global search in the first place.

The design refinement is subsequently carried out by tuning the geometry parameters of the entire metasurface at the EM level of description. As mentioned before, because the proposed formulation of the design problem offers a reliable insight into the metasurface properties even though the design process is implemented at the level of meta-atoms, the amount of this final tuning is normally minor as compared to what would be necessary in the case of the standard formulation. The last part of this section briefly describes the design closure process.

Let x_A denote the aggregated designable parameter vector identified after surrogate-assisted optimization procedure and $R_{red}(x_A, f)$ denote the resultant RCS reduction over frequency f. Moreover, to efficiently administer possible discontinuities in the objective function values due to localized violations of the condition $R_{red}(x_A, f) \geq \sigma_{Rmax}$ at certain frequency subbands (cf. Fig. 1), a penalty term is introduced. This way, the violations are smoothly accommodated into the objective function, which is defined as

$$U_{RCS}(x_A) = -[f_H(x_A) - f_L(x_A)] + \beta c_r(x_A)^2 \quad (9)$$

The first component in (9) is the primary objective (RCS reduction bandwidth), whereas the second component is a penalty term with the function c_r defined as $c_r(x_A) = d_r$ if $d_r > 0$ and zero elsewhere. It is introduced to handle the detrimental violations of the acceptance threshold within the target band. The contribution of the penalty term is monitored by the factor β. Here, $\beta = 1$, but it is not critical. Nevertheless, it can be used to regulate the tolerance level of d_r.

The design refinement task is formulated as

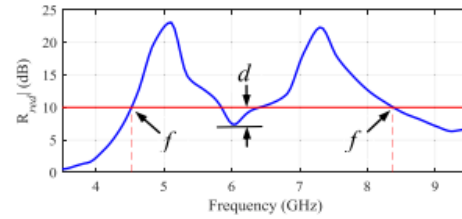$$x_A^* = \arg \min_{x_A \in X_1 \times X_2} U_{RCS}(x_A) \quad (10)$$

FIGURE 1. Exemplary RCS characteristic with f_L and f_U represent the minimum and the maximum frequency for which the condition $R_{red}(x_A, f) \geq \sigma_{Rmax}$, is satisfied, and d_r denote the maximum allowed violation within the frequency interval $[f_L f_U]$.

The problem (10) is a simulation-based optimization stage (i.e., the information about the meta atom characteristics is primarily acquired from EM analysis), in which we seek for the parameter vector x_A^* that maximizes the bandwidth in the sense of (9). Note that this involves independent sizing of both meta atoms (i.e., the search process is conducted over the Cartesian product of the relevant parameter spaces X_1 and X_2).

Here, the trust-region (TR) gradient-based algorithm [37] is utilized to circumnavigate the high computational cost incurred by multiple structure evaluations. Additionally, other acceleration mechanisms, i.e., the adaptive application of the rank-one Broyden formula [25] is adopted to maintain the CPU overhead to practically acceptable levels. Figure 2 shows the flow diagram of the surrogate-assisted design procedure described above.

III. RESULTS AND DISCUSSION

This section presents the topology of the meta-atom (metasurface building block) utilized as a specific demonstration example of the design approach proposed in the work. Subsequently, the modeling and optimization results together with the performance evaluation of the optimum meta-atom designs are discussed. Finally, the practical utility and the advantages of the presented metasurface development task formulation is illustrated through the design of a complete metasurface. The detailed performance evaluation of a high-performance coding metasurface rendered by means of our approach, will be supplied in Section IV.

A. META-ATOM GEOMETRY

Figure 3(a) shows the meta-atom geometry considered in this work as a specific illustration example. The design shape resembles the crusader cross. The parameters p, b, and d determine the overall structure of the meta-atom, and they are adjusted as a vector of designable variables in the optimization process. The overall size of the meta-atom is fixed to $W \times L = 6 \times 6$ mm^2. As indicated in Fig. 3(b), the considered design extends ample flexibility while maintaining low dimensionality of the design space.

The latter eases the data-driven modeling procedure, in particular, ensures sufficient predictive power of the metamodels without incurring excessive computational expenses. It must
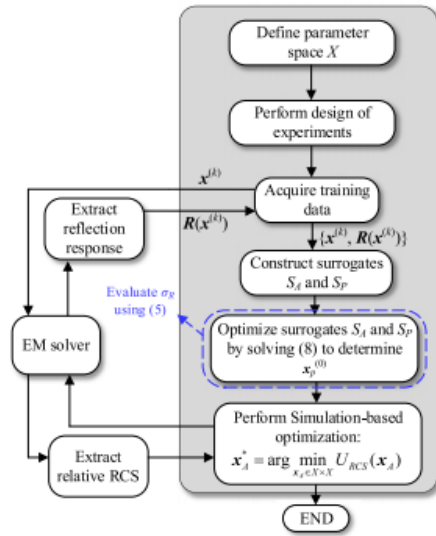
FIGURE 2. Flow diagram of a surrogate-assisted design procedure involving metamodels.
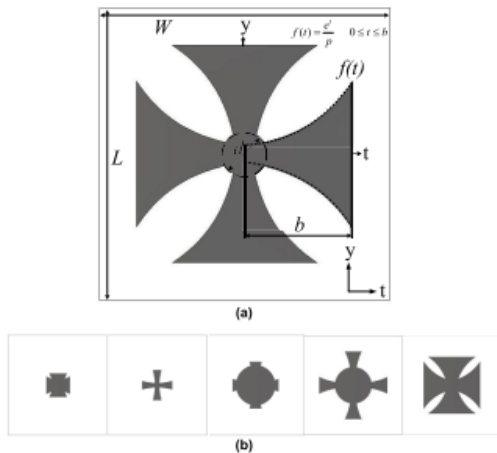

FIGURE 3. Configuration of the meta-atom considered in this work: (a) crusader cross topology, (b) five exemplary meta-atom geometries within the parameter space.

be remembered that the geometries in Fig. 3(a) and (b) visually illustrate the versatility of the considered design topology, and they do not represent the optimum designs utilized in the development of the coding metasurface. The latter will be supplied in the subsequent sub-section.

Throughout this work, a ground-backed Arlon AD250 ($\varepsilon_r = 2.5$, $h = 1.5$ mm, $\tan\delta = 0.0018$) is modeled as a dielectric medium. During the simulations, metallization is represented as perfect electrical conductor (PEC).

B. METAMODEL TRAINING AND VALIDATION

As mentioned in the previous section, the considered meta-atom design (cf. Fig. 1(a)) has three geometry parameters, i.e., p, b, and d. Therefore, the vector of designable variables is $x = [p\,b\,d]^T$. The lower and upper limits are set to $l = [3.5\ 0.3\ 0.2]^T$, and $u = [10\ 1.6\ 2.4]^T$; all dimensions are in mm. The training data is arranged on a uniform grid $M_{7.12.7}$ (cf. Section II. C) with a total number of $N = 588$ samples. The obtained EM-simulation data has been divided into the training (85 percent) and the testing (15 percent) data, later utilized for split-sample error evaluation. The frequency-domain solver of the CST Microwave Studio is employed to obtain the reflection (amplitude and phase) responses of the meta-atoms. It should be noted that the EM simulation model of the meta-atom contains about 22,000 mesh cells. The corresponding simulation time to compute the reflection response of a meta-atom is 70 seconds. Consequently, the overall CPU time required for training data acquisition is about eleven hours.

The absolute error of the metamodels S_A and S_P is 0.0003 0.86 degrees (averaged over the testing data) with the standard deviation of 0.0005 and 1.7 degrees, respectively. These statistics validates excellent predictive capabilities of the surrogates, especially for S_P, where the typical range of the reflection phase response exceeds 400 degrees. Further, Fig. 4 demonstrates the surrogate and the EM-simulated reflection responses for the selected test samples. As can be observed, the surrogate model responses are in excellent agreement with the corresponding EM-simulated outputs. This alignment indicates that the globally-optimum solution obtained at the level of the surrogate is likely to be located in a close vicinity of the true (i.e., EM-level) optimum.

It should be noted that, in this work, the surrogate is constructed directly for the amplitude and phase responses of the unit cell, rather than for real and imaginary parts of the electric field. The latter is typically carried out (e.g., [39]) due to the fact that real and imaginary components are smooth and of well-defined ranges. Nevertheless, here, accurate surrogates of amplitude and phase were obtained using reasonably small number of training data samples, with the reported modeling errors giving direct account of the model predictive power.

C. OPTIMIZATION RESULTS

Following the successful training and validation of the meta-models, the exhaustive search-based global optimization (cf. (8)) has been executed to obtain the optimum meta-atom designs. The optimization procedure delivers a solution as $x_1^* = [3.52\ 0.73\ 2.40]^T$ and $x_2^* = [4.22\ 1.60\ 2.16]^T$. Figure 5(a) illustrates the designs topologies, labeled as Atom 0 and Atom 1.

To test the consistency of the RCS characteristics obtained by means of the proposed design problem formulation against full-wave EM simulations, the corresponding 2×2 coding metasurface is implemented, see Fig. 5(b). The latter
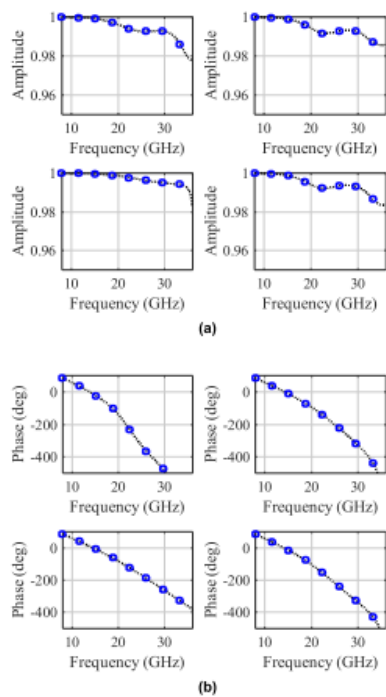
FIGURE 4. Performance of the surrogate models at the selected test locations; (a) amplitude (S_A), and (b) phase reflection response predictor (S_P). EM model (...) and surrogate responses (o).

FIGURE 5. Optimized design solutions (upon applying surrogate-assisted optimization procedure). (a) meta-atom designs: Atom 1 (left), and Atom 0 (right), (b) configuration of a 2 × 2 coding metasurface.

FIGURE 6. RCS reduction characteristic obtained at the level of meta-atoms using the proposed design problem formulation (black), and the corresponding EM-simulation response of the implemented 2 × 2 metasurface (blue). The red horizontal line represents the target RCS reduction threshold, here 10-dB.

consists of four elements: each of them contains four 4 × 4 periodic lattices of Atom 0 and Atom 1. The overall size of the structure is $W_s \times L_s = 48 \times 48$ mm^2. The inter-element spacing among the adjacent meta-atoms is $s = 6$ mm. To evaluate the RCS reduction performance of a coding meta-surface, an equivalent metallic surface is implemented to be utilized as a reference. The time-domain solver of the CST Microwave Studio is utilized for EM analysis. The EM simulation model of the metasurface presented in Fig. 5 contains about 2,400,000 mesh cells and its corresponding simulation time is 30 minutes.

Figure 6 shows the comparison between the RCS reduction performance rendered using our design problem formulation (at the level of meta-atoms), and EM-simulated RCS reduction of the metasurface. It can be observed that the two datasets decently coincide with each other. In particular, the 10-dB RCS reduction bandwidth is identical for both instances. Finally, the simulation-based local tuning is performed (cf. Section II. C) for further refinement. The obtained design is $x_A^* = [3.89\ 1.66\ 2.46\ 3.87\ 0.74\ 2.54]^T$. For the sake of comparison, the RCS performance before and after simulation-based refinement stage is presented in Fig. 7. As expected, the improvement at this stage is minor due to
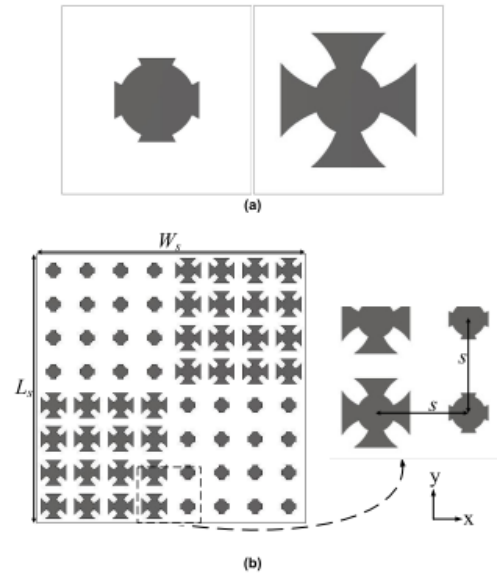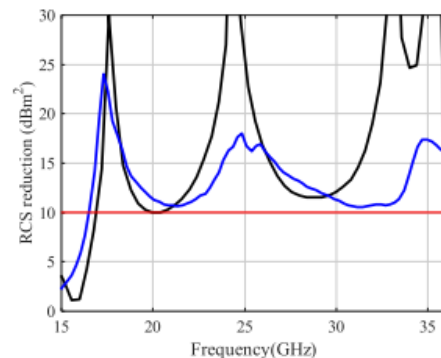
the availability of a good initial design, determined by the proposed design task formulation. It corroborates the design utility of the proposed approach. It should also be noted that certain violation of the 10 dB threshold for RCS reduction can be observed around the frequency of 35 GHz. This is due to setting the penalty coefficient β at relatively low value (here, 100), which makes the objective function tolerant to small violations of the threshold, while promoting bandwidth enhancement.
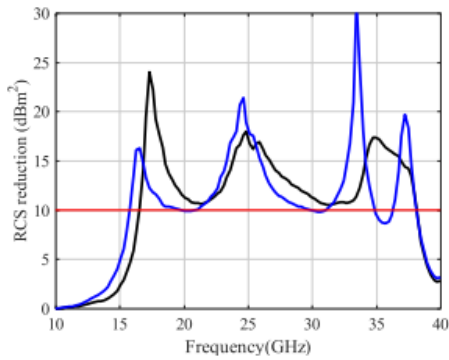
FIGURE 7. RCS reduction characteristic before (black), and after (blue) simulation-based local refinement. The red horizontal line represents the target RCS reduction threshold, here 10-dB.

FIGURE 8. Reflection performance of the optimum meta-atom designs obtained using the standard formulation (cf. Section II. *A*): reflection amplitude (top), and reflection phase (bottom). The responses of Atom 0 and Atom 1 are marked black and red, respectively, whereas the blue curve indicates the reflection phase difference. The gray-shaded area in the bottom plot indicates the range of acceptable phase differences.

D. BENCHMARKING

The metasurface design problem formulation proposed in this work has been benchmarked against the standard formulation outlined in Section II. *A*, where only the phase reflection response of the meta-atoms is considered. The assessment is conducted in terms of a precise account for the anticipated RCS reduction bandwidth at the level of unit cell optimization, as well as the actual RCS reduction bandwidth of the entire metasurface. Figure 8 demonstrates the reflection (amplitude and phase) performance of the optimum design solution obtained after applying global optimization procedure of Section II. *C* to solve the design task (2). It can be noticed that when considering the standard formulation as in (1), the anticipated 10-dB RCS reduction bandwidth extends from 16 GHz to 36 GHz. However, as presented in Fig. 9, the actual RCS reduction bandwidth of a corresponding 2×2 metasurface exhibits violations of the 10-dB target threshold at a significant part of the operating band, specifically from about 13 to 26 GHz, with the maximum violation of almost 3 dB. It should be reiterated that the standard formulation does not explicitly account for the RCS reduction characteristics at the level of meta-atom performance, and it only takes into account the phase reflection performance of the meta-atoms.

In other words, the performance achieved in terms of the phase responses at the level of meta-atoms does not carry over to the RCS reduction of the metasurface. On the contrary, Fig. 6 illustrates that the approximated 10-dB RCS reduction bandwidth obtained using our methodology is nearly identical to that of the actual bandwidth. Hence, it can be concluded that our methodology provides a direct account for RCS reduction performance of the metasurface, and, therefore, it is more reliable in the development of high-quality structures.

IV. NUMERICAL AND EXPERIMENTAL VALIDATIONS

This section presents a comprehensive description of a high-performance coding metasurface developed by applying the
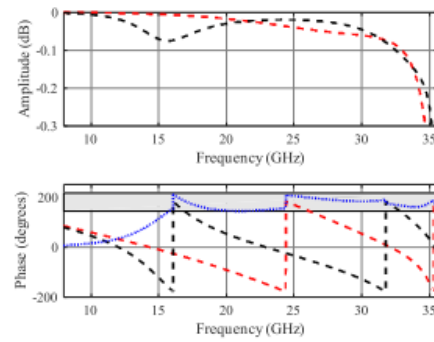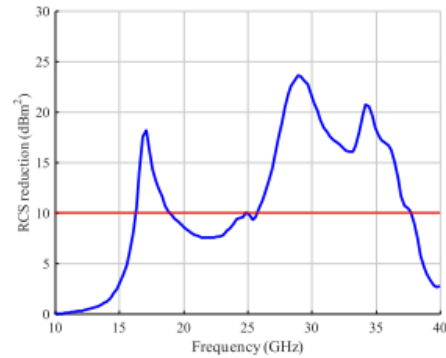

FIGURE 9. RCS reduction characteristics of a metasurface at the optimized meta-atom designs. The red horizontal line represents the 10-dB RCS reduction threshold relative to the PEC surface.

proposed design task formulation. The reason for conducting the optimization process at the level of a smaller, 2×2 metasurface, is explained, followed by a discussion on the monostatic and bistatic RCS performance of a designed 6×6 coding metasurface. The experimental setup is also presented, along with the measurement results of the prototyped measurfaces.

A. CODING METASURFACE PERFORMANCE

So far, we considered a 2×2 metasurface throughout the design optimization procedure. The primary reason is that the RCS reduction performance of a metasurface is always normalized to the equivalent size metallic surface. Consequently, the size of the structure is a nominal factor. The same approach has been adopted in the literature (e.g., [14]). In particular, it has been suggested that the RCS reduction

characteristics of a 2 × 2 metasurface with the reference to a metallic surface provides a decent representation of the corresponding structure of a larger size. This has been numerically corroborated through a comparative study carried out to compare the RCS reduction performance of a 2 × 2 and 6 × 6 metasurface, presented in Fig. 10. It can be noticed that the RCS reduction characteristics for both structures are well aligned.
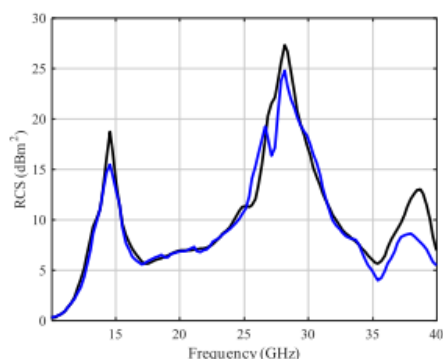

FIGURE 10. RCS reduction characteristics of a 2 × 2 (black) and 6 × 6 (blue) metasurface.

At this point, we employ the globally optimum meta-atom designs obtained in Section III to characterize a high-performance metasurface architecture featuring broadband RCS reduction. As mentioned in Section II. *B*, the RCS of a one-bit coding metasurface can be approximated as in (4). The underlying principle of a corresponding RCS reduction is based on the array theory [38], in particular, the entire metasurface architecture exploits the anti-phase reflection property (recall that meta-atoms are optimized to have 180° out-of-phase reflection) of periodic arrays to tailor the EM wavefront. Furthermore, it has been indicated in the literature that a standard checkerboard configuration disperses the incident EM energy into four pre-defined scattering lobes [15]. In a related vein, by employing lattices of 'Atom 0' and 'Atom 1' in a random configuration, more scattering lobes can be realized [16], resulting in an improved RCS reduction of the overall metasurface.

In this work, the composition of the lattices is determined by globally optimizing array factor-based approximation model (e.g., in [18]) using a binary coded genetic algorithm (GA), as presented in [18]. Figure 11 illustrates the optimized configuration of the coding metasurface comprising thirty six elements: each of them contains four 4 × 4 periodic lattices of Atom 0 and Atom 1. The overall size of the structure is $W_s × L_s = 144 × 144$ mm^2. Again, the inter-element spacing among the adjacent meta-atoms is $s = 6$ mm.

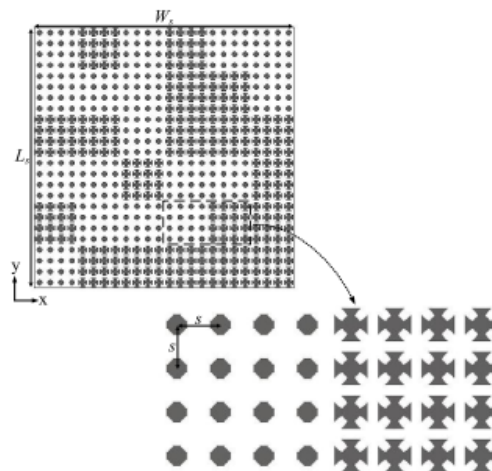To test the RCS reduction properties of a characterized metasurface, its monostatic and bistatic RCS performance

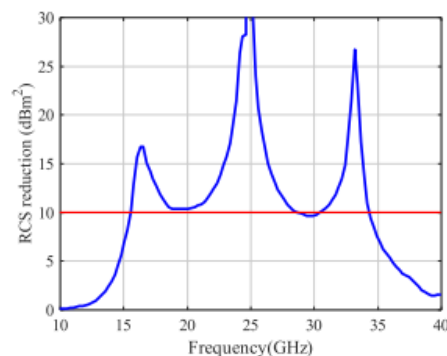**FIGURE 11.** GA-optimized configuration of the coding metasurface.

FIGURE 12. RCS reduction performance of the optimized configuration of a 6 × 6 metasurface. The response shown is obtained through EM simulation of the structure (underlying meta-atom designs are identical to the ones given in Section III. C). The red horizontal line represents the target RCS reduction threshold.

under the plane wave incidence has been evaluated. Figure 12 shows the monostatic RCS reduction performance of a coding metasurface. It can be observed that the structure features RCS reduction in a broad frequency range, i.e., from 15.5 GHz to 34.6 GHz. Furthermore, the 3-D bistatic RCS patterns of the coding metasurface, and the equivalent size metallic surface has been illustrated in Fig. 13. It can be observed that the metallic surface causes strong reflections in the boresight direction, in a single lobe when the plane wave impinges on it. Conversely, the coding metasurface diffuses the incident wave to several directions, which results in a significant reduction of the energy in the vicinity of the scattering peak, i.e., the boresight direction.
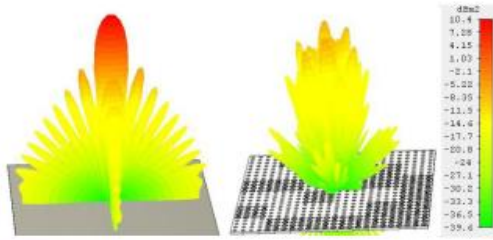
FIGURE 13. 3D scattering performance: PEC surface (left) and the coding metasurface (right). The plots correspond to the frequency of 25 GHz.

B. EXPERIMENTAL VALIDATION

The coding metasurface illustrated in Section. IV. *A* has been prototyped and measured to validate the EM simulation results. A photograph of the fabricated structure is given in Fig. 14, whereas the measurement setup is demonstrated in Fig. 15.
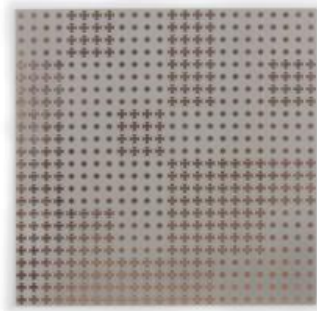

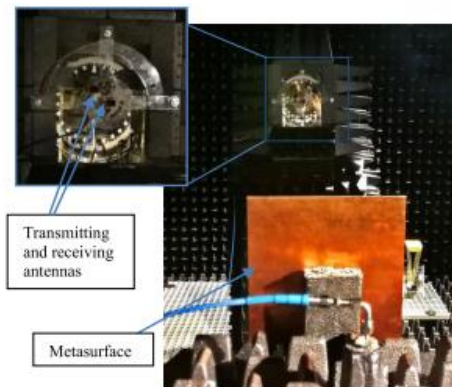**FIGURE 14.** Photographs of the prototyped metasurface.

FIGURE 15. Measurement setup at Reykjavik University.

The setup includes a vector network analyzer (VNA), and a pair of linearly-polarized horn antennas (PE9850/2F-15). The two antennas are positioned perpendicular to the surface under test, among them, one of the antennas is for transmission, whereas the other one for reception of the EM waves. The experimental setup is realized in a farfield environment. The scattering performance of the metasurface under test, and the equivalent metallic surface is evaluated by measuring the transmission coefficient, captured by the VNA.
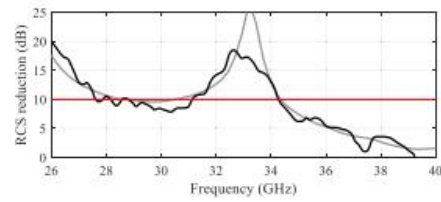

FIGURE 16. Measured (black) and simulated (gray) RCS reduction performance comparison. The red curve indicates 10-dB RCS reduction threshold.

Figure 16 shows a decent agreement between measurements and EM simulations. A slight discrepancy between the two datasets can be attributed to several reasons. Amidst, the principal factor is the spatial misalignment of the transmitting or receiving antenna with respect to surface under test. Needless to say, the precise alignment of the structure with respect to antennas (realized physically) is a challenging endeavor. A small misalignment here may lead to considerable inconsistencies. Still, the measurement results agree to 10-dB RCS reduction bandwidth obtained through EM simulation.

Due to the limited amenities available, the physical experiment is carried out in the frequency range of 26.5 GHz and 40 GHz. The above findings confirm the utility of the proposed metasurface design task formulation scheme in the context of stealth technology applications.

V. CONCLUSION

This article proposes a novel formulation of the metasurface design task, which enables explicit control over the RCS reduction at the level of meta-atoms. The design objective is defined to directly optimize the RCS reduction bandwidth at the specified level (e.g., 10 dB) with reference to the metallic surface. The latter is highly desirable in stealth applications. The introduced formulation account for both the reflection phases and the amplitudes of the individual meta-atoms, with the latter being typically disregarded (assumed to be equal to one) in the conventional formulation. Consequently, our approach offers a deeper insight into the entire metasurface properties even through the design process is executed at the level of unit cells.

The utility of our formulation is demonstrated by developing a high-performance coding metasurface. The final design consists of crusader-cross-shaped meta-atom designs

as a building block of the entire architecture. The design procedure is implemented using two-fold optimization, oriented toward maximization of the RCS reduction bandwidth. The initial stage employs a data-driven strategy to determine globally optimum meta-atom designs, followed by simulation-based optimization of the entire metasurface. The former involves a fast surrogate model that enables global exploration of the parameter space, otherwise unrealistic due to a massive number of EM-simulations involved. Owing to the proposed methodology, only a slight adjustment is required at the level of entire metasurface. Furthermore, the system characteristics predicted at the meta-atom design stage are well aligned with those of the EM-simulated structure, which reduces the overall computational cost of the design process. The proposed formulation has been benchmarked against standard approach demonstrated to be superior in terms of the anticipated RCS reduction bandwidth, and rendering a precise control over the RCS reduction threshold. Finally, the monostatic and bistatic performance of the coding metasurface have been briefly described. The designed metasurface features 10-dB RCS reduction in the frequency range of 16.5 GHz to 34.6 GHz. The structure has been prototyped to validate the simulation results. A good agreement between the two datasets has been observed.

It should be emphasized that the proposed methodology capitalized on a typically small number of geometry parameters describing the meta atoms. Therefore, its scalability for higher dimension will be limited. In particular, application of the approach would require a replacement of design of experiments (from grid sampling to, e.g., space-filling designs, such as Latin Hypercube Sampling, or sequential sampling methods).
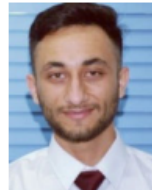
REFERENCES

[1] E. F. Knott, *Radar Cross Section Measurements*. Springer, 2012, pp. 12–36.

[2] P. Westwick, *Stealth: The Secret Contest to Invent Invisible Aircraft*. London, U.K.: Oxford Univ. Press, 2019, pp. 5–42.

[3] T. A. Khan, J. X. Li, Z. Li, M. Abdullah, J. Chen, and A. X. Zhang, "Design of Vivaldi antenna with wideband reduced radar cross section," *AEU Int. J. Electron. Commun.*, vol. 95, pp. 47–51, Oct. 2018.

[4] H. Ahmad, A. Tariq, A. Shehzad, M. S. Faheem, M. Shafiq, I. A. Rashid, A. Afzal, A. Munir, M. T. Riaz, H. T. Haider, A. Afzal, M. B. Qadir, and Z. Khaliq, "Stealth technology: Methods and composite materials—A review," *Polym. Compos.*, vol. 40, no. 12, pp. 4457–4472, 2019.

[5] T. J. Cui, D. R. Smith, and R. Liu, *Metamaterials Theory, Design, and Applications*. New York, NY, USA: Springer, 2010.

[6] A. V. Kildishev, A. Boltasseva, and V. M. Shalaev, "Planar photonics with metasurfaces," *Science*, vol. 339, no. 6125, Mar. 2013, Art. no. 1232009.

[7] N. I. Landy, S. Sajuyigbe, J. J. Mock, D. R. Smith, and W. J. Padilla, "Perfect metamaterial absorber," *Phys. Rev. Lett.*, vol. 100, no. 20, pp. 207–402, 2008.

[8] F. Costa, A. Monorchio, and G. Manara, "Analysis and design of ultra thin electromagnetic absorbers comprising resistively loaded high impedance surfaces," *IEEE Trans. Antennas Propag.*, vol. 58, no. 5, pp. 1551–1558, May 2010.

[9] Y. Liu and X. Zhao, "Perfect absorber metamaterial for designing low-RCS patch antenna," *IEEE Antennas Wireless Propag. Lett.*, vol. 13, pp. 1473–1476, 2014.

[10] X. Gao, X. Han, W.-P. Cao, H. O. Li, H. F. Ma, and T. J. Cui, "Ultra-wideband and high-efficiency linear polarization converter based on double V-shaped metasurface," *IEEE Trans. Antennas Propag.*, vol. 63, no. 8, pp. 3522–3530, Aug. 2015.

[11] M. Paquay, J. C. Iriarte, I. Ederra, R. Gonzalo, and P. D. Maagt, "Thin AMC structure for radar cross-section reduction," *IEEE Trans. Antennas Propag.*, vol. 55, no. 12, pp. 3630–3638, Dec. 2007.

[12] K. Chang, "Electromagnetic gradient surface and its application to flat reflector antennas," Ph. D. dissertation, Dept. Electr. Electron. Eng., Yonsei Univ., Seoul, South Korea, 2009.

[13] J. C. I. Galarregui, A. T. Pereda, J. L. M. de Falcón, I. Ederra, R. Gonzalo, and P. de Maagt, "Broadband radar cross-section reduction using AMC technology," *IEEE Trans. Antennas Propag.*, vol. 61, no. 12, pp. 6136–6143, Dec. 2013.

[14] W. Chen, C. A. Balanis, and C. R. Birtcher, "Checkerboard EBG surfaces for wideband radar cross section reduction," *IEEE Trans. Antennas Propag.*, vol. 63, no. 6, pp. 2636–2645, Jun. 2015.

[15] S. H. Kim and Y. J. Yoon, "Wideband radar cross-section reduction on checkerboard metasurfaces with surface wave suppression," *IEEE Antennas Wireless Propag. Lett.*, vol. 18, no. 5, pp. 896–900, May 2019.

[16] L. Ali, Q. Li, T. A. Khan, J. Yi, and X. Chen, "Wideband RCS reduction using coding diffusion metasurface," *Materials*, vol. 12, no. 17, p. 2708, Aug. 2019.

[17] T. J. Cui, M. Q. Qi, X. Wan, J. Zhao, and Q. Cheng, "Coding metamaterials, digital metamaterials and programmable metamaterials," *Light, Sci. Appl.*, vol. 3, no. 10, p. e218, Oct. 2014.

[18] T. A. Khan, J. Li, J. Chen, M. U. Raza, and A. Zhang, "Design of a low scattering metasurface for stealth applications," *Materials*, vol. 12, no. 18, p. 3031, Sep. 2019.

[19] Y. Zhao, X. Cao, J. Gao, Y. Sun, H. Yang, X. Liu, Y. Zhou, T. Han, and W. Chen, "Broadband diffusion metasurface based on a single anisotropic element and optimized by the simulated annealing algorithm," *Sci. Rep.*, vol. 6, no. 1, pp. 1–9, Jul. 2016.

[20] S. Sui, H. Ma, J. Wang, Y. Pang, M. Feng, Z. Xu, and S. Qu, "Absorptive coding metasurface for further radar cross section reduction," *J. Phys. D, Appl. Phys.*, vol. 51, no. 6, Feb. 2018, Art. no. 065603.

[21] H. Yang, X. Cao, F. Yang, J. Gao, S. Xu, M. Li, X. Chen, Y. Zhao, Y. Zheng, and S. Li, "A programmable metasurface with dynamic polarization, scattering and focusing control," *Sci. Rep.*, vol. 6, no. 1, pp. 1–11, Dec. 2016.

[22] M. Chen, M. Kim, A. M. H. Wong, and G. V. Eleftheriades, "Huygens' metasurfaces from microwaves to optics: A review," *Nanophotonics*, vol. 7, no. 6, pp. 1207–1231, Jun. 2018.

[23] J. Ji, J. Jiang, G. Chen, F. Liu, and Y. Ma, "Research on monostatic and bistatic RCS of cloaking based on coordinate transformation," *Optik*, vol. 165, pp. 117–123, Jul. 2018.

[24] R. Pestourie, C. Pérez-Arancibia, Z. Lin, W. Shin, F. Capasso, and S. G. Johnson, "Inverse design of large-area metasurfaces," *Opt. Exp.*, vol. 26, no. 26, pp. 33732–33747, 2018.

[25] S. Koziel and A. Pietrenko-Dabrowska, "Expedited optimization of antenna input characteristics with adaptive Broyden updates," *Eng. Computations*, vol. 37, no. 3, pp. 851–862, Sep. 2019.

[26] T. W. Simpson, J. D. Poplinski, P. N. Koch, and J. K. Allen, "Metamodels for computer-based engineering design: Survey and recommendations," *Eng. with Comput.*, vol. 17, no. 2, pp. 129–150, Jul. 2001.

[27] S. Koziel, L. Leifsson, and X. S. Yang, "Surrogate-based optimization," in *Simulation-Driven Design Optimization and Modeling for Microwave Engineering*, S. Koziel, X. S. Yang, and Q. J. Zhang, Eds. London, U.K.: Imperial College Press, 2012, pp. 41–80.

[28] S. Koziel and J. W. Bandler, "Reliable microwave modeling by means of variable-fidelity response features," *IEEE Trans. Microw. Theory Techn.*, vol. 63, no. 12, pp. 4247–4254, Dec. 2015.

[29] S. Koziel and A. Pietrenko-Dabrowska, *Performance-Driven Surrogate Modeling of High-Frequency Structures*. New York, NY, USA: Springer, 2020.

[30] F. Feng, W. Na, W. Liu, S. Yan, L. Zhu, J. Ma, and Q.-J. Zhang, "Multifeature-assisted neuro-transfer function surrogate-based EM optimization exploiting trust-region algorithms for microwave filter design," *IEEE Trans. Microw. Theory Techn.*, vol. 68, no. 2, pp. 531–542, Feb. 2020.

[31] J. Peurifoy, Y. Shen, L. Jing, Y. Yang, F. Cano-Renteria, B. G. DeLacy, J. D. Joannopoulos, M. Tegmark, and M. Soljačić, "Nanophotonic particle simulation and inverse design using artificial neural networks," *Sci. Adv.*, vol. 4, no. 6, Jun. 2018, Art. no. eaar4206.

[32] X. Chen, W. Xue, H. Shi, L. Wang, S. Zhu, and A. Zhang, "Improving field uniformity using source stirring with orbital angular momentum modes in a reverberation chamber," *IEEE Microw. Wireless Compon. Lett.*, vol. 29, no. 8, pp. 560–562, Aug. 2019.

[33] X. Chen, W. Xue, H. Shi, J. Yi, and W. E. I. Sha, "Orbital angular momentum multiplexing in highly reverberant environments," *IEEE Microw. Wireless Compon. Lett.*, vol. 30, no. 1, pp. 112–115, Jan. 2020.

[34] J. Jiang and J. A. Fan, "Simulator-based training of generative neural networks for the inverse design of metasurfaces," *Nanophotonics*, vol. 9, no. 5, pp. 1059–1069, Nov. 2019.

[35] W. Ma, F. Cheng, Y. Xu, Q. Wen, and Y. Liu, "Probabilistic representation and inverse design of metamaterials based on a deep generative model with semi-supervised learning strategy," *Adv. Mater.*, vol. 31, no. 35, Aug. 2019, Art. no. 1901111.

[36] A. Hoorfar, "Evolutionary programming in electromagnetic optimization: A review," *IEEE Trans. Antennas Propag.*, vol. 55, no. 3, pp. 523–537, Mar. 2007.

[37] S. Koziel, J. W. Bandler, and Q. S. Cheng, "Robust trust-region space-mapping algorithms for microwave design optimization," *IEEE Trans. Microw. Theory Techn.*, vol. 58, no. 8, pp. 2166–2174, Jul. 2010.

[38] A. Y. Modi, C. A. Balanis, C. R. Birtcher, and H. N. Shaman, "New class of RCS-reduction metasurfaces based on scattering cancellation using array theory," *IEEE Trans. Antennas Propag.*, vol. 67, no. 1, pp. 298–308, Jan. 2019.

[39] S. An, C. Fowler, B. Zheng, M. Y. Shalaginov, H. Tang, H. Li, L. Zhou, J. Ding, A. M. Agarwal, C. Rivero-Baleine, K. A. Richardson, T. Gu, J. Hu, and H. Zhang, "A deep learning approach for objective-driven all-dielectric metasurface design," *ACS Photon.*, vol. 6, no. 12, pp. 3196–3207, 2019.

MUHAMMAD ABDULLAH received the B.Sc. degree from the University of Engineering and Technology, Pakistan, in 2016, and the M.Sc. degree from Xi'an Jiaotong University (XJTU), China, in 2019. Since late 2019, he has been associated with the Department of Engineering, Reykjavik University, Iceland, as a Researcher. From 2018 to 2019, he was with the Electromagnetics and Communication Laboratory, XJTU. On completion of M.Sc. degree, he received the Excellent Master's Thesis Award. His broader research interests include surrogate-based modeling and optimization, CAD and modeling of antennas and other high-frequency structures, simulation-driven design, machine-learning techniques, and millimeter-wave communication.

SLAWOMIR KOZIEL (Senior Member, IEEE) received the M.Sc. degree in electronic engineering from Gdańsk University of Technology, Poland, in 1995, the dual M.Sc. degree in theoretical physics and in mathematics from the University of Gdańsk, Poland, in 2000 and 2002, the Ph.D. degree in electronic engineering from Gdańsk University of Technology, in 2000, and the Ph.D. degree in mathematics from the University of Gdańsk, in 2003. He is currently a Professor with the Department of Engineering, Reykjavik University, Iceland. His research interests include CAD and modeling of microwave and antenna structures, simulation-driven design, surrogate-based optimization, space mapping, circuit theory, analog signal processing, evolutionary computation, and numerical analysis.

STANISLAW SZCZEPANSKI received the M.Sc. and Ph.D. degrees in electronic engineering from Gdańsk University of Technology, Poland, in 1975 and 1986, respectively. In 1986, he was a Visiting Research Associate with the Institute National Polytechnique de Toulouse (INPT), Toulouse, France. From 1990 to 1991, he was with the Department of Electrical Engineering, Portland State University, Portland, OR, USA, on a Kosciuszko Foundation Fellowship. From August to September 1998, he was a Visiting Professor with the Faculty of Engineering and Information Sciences, University of Hertfordshire, Hatfield, U.K. He is currently a Professor with the Department of Microelectronic Systems, Faculty of Electronics, Telecommunications and Informatics, Gdańsk University of Technology. He has published more than 160 articles and holds three patents. His teaching and research interests include circuit theory, fully integrated analog filters, high-frequency transconductance amplifiers, analog integrated circuit design, and analog signal processing.

• • •

Chapter 7

7 Paper # 5

Muhammad Abdullah, Slawomir Koziel, and Stanislaw Szczepanski

Normalized Partial Scattering Cross Section for Performance Evaluation of Low-Observability Scattering Structures

Article

Normalized Partial Scattering Cross Section for Performance Evaluation of Low-Observability Scattering Structures

Muhammad Abdullah [1], Slawomir Koziel [1,2,*] and Stanislaw Szczepanski [2]

1 Engineering Optimization and Modeling Center, Reykjavik University, 101 Reykjavik, Iceland; muhammada19@ru.is
2 Faculty of Electronics, Telecommunications and Informatics, Gdańsk University of Technology, 80-233 Gdańsk, Poland; stanislaw.szczepanski@pg.edu.pl
* Correspondence: koziel@ru.is

Abstract: The development of diffusion metasurfaces created new opportunities to elevate the stealthiness of combat aircraft. Despite the potential significance of metasurfaces, their rigorous design methodologies are still lacking, especially in the context of meticulous control over the scattering of electromagnetic (EM) waves through geometry parameter tuning. Another practical issue is insufficiency of the existing performance metrics, specifically, monostatic and bistatic evaluation of the reflectivity, especially at the design stage of metasurfaces. Both provide limited insight into the RCS reduction properties, with the latter being dependent on the selection of the planes over which the evaluation takes place. This paper introduces a novel performance metric for evaluating scattering characteristics of a metasurface, referred to as Normalized Partial Scattering Cross Section (NPSCS). The metric involves integration of the scattered energy over a specific solid angle, which allows for a comprehensive assessment of the structure performance in a format largely independent of the particular arrangement of the scattering lobes. We demonstrate the utility of the introduced metric using two specific metasurface architectures. In particular, we show that the integral-based metric can be used to discriminate between the various surface configurations (e.g., checkerboard versus random), which cannot be conclusively compared using traditional methods. Consequently, the proposed approach can be a useful tool in benchmarking radar cross section reduction performance of metamaterial-based, and other types of scattering structures.

Keywords: diffusion; metasurfaces; radar cross section (RCS); performance metrics; bistatic scattering

1. Introduction

In recent years, metasurfaces, with their unique ability to shape the electromagnetic (EM) wavefront, have attracted increasing attention from researchers and practitioners [1–3]. Some of the areas where metasurfaces found their applications include radar cross section (RCS) reduction, as well as spatial processing, and polarization conversion techniques [4–6]. The advancements of radar detection technology placed RCS reduction in a forefront of research on stealth technology [7]. To date, metasurfaces have been extensively exploited to accomplish essential RCS reduction of the targets [8,9]. One practical design strategy in this regard is to utilize metamaterials, particularly, exploiting their distinctive property of manipulating the phase reflection characteristics [10]. It entails a periodic combination of artificial magnetic conductors (AMC), and perfect electric conductors (PEC), arranged to attain the desired phase reflection characteristics. To extend the RCS reduction bandwidth of such structures, the concepts of coding metasurfaces [11], diffusion metasurfaces [12,13], programmable metasurfaces [14], Huygens' metasurfaces [15], as well as cloaking structures [16], have been proposed, which offers control over the wavefront in a more sophisticated manner. The primary advantage of coding and diffusion metasurfaces is that it scatters the incident EM waves into all directions. In addition to that, coding metasurfaces are also being exploited as an absorptive surface to realize essential RCS reduction [17].

The design of metasurfaces requires availability of performance metrics that can be applied for their assessment, as well as to discriminate between alternative architectures. The existing metrics developed to measure RCS reduction performance of a diffusion metasurface are based on evaluating the energy scattered from the target with reference to the PEC surface featuring the same physical dimension. The scattering characteristics can be studied in monostatic and bistatic modes of operation [18–23]. The former conforms to a situation where the transmitter and the receiver radars are collocated, and, hence, RCS performance of an aircraft is evaluated with respect to a specified position [24]. This approach provides limited insight into the metasurface properties. In a related vein, a bistatic mode corresponds to a condition when the transmitter and receiver radars are stationed at a certain distance between them [24]. Unfortunately, bistatic RCS performance is highly dependent on the selection of the planes over which the evaluation takes place [25], which makes it inconvenient as an evaluation tool for RCS-reduction-oriented metasurface design. In Reference [26], a figure of merit for bistatic RCS reduction (FMB) has been introduced (based on the maximum RCS), which is a step forward in making RCS evaluation angle-independent. However, this metric boils down to considering the worst-case scenario performance, which may provide an overly pessimistic evaluation because it is related to the maximum reflection lobe of a small angular spread. With the development of multi-base radar detection technology, the accomplishment of bistatic RCS reduction turns out to be a measure of choice, together with the monostatic RCS. Notwithstanding, comprehensive quantification of the scattered energy in a regime that is independent of an arbitrary selection of the specific setup, requires the development of more sophisticated measures of merit. These should be pertinent to both contemporary needs (as the aforementioned multi-base radars), and the various types of metasurfaces featuring distinct scattering patterns.

This paper introduces a novel performance metric for evaluating scattering properties of metasurfaces, which is intended to deliver an effective tool for comprehensive assessment of RCS reduction characteristics. The metric, referred to as Normalized Partial Scattering Cross Section (NPSCR), involves numerical integration of the energy scattered from the target over a solid angle. As a result, a conclusive assessment concerning observability properties of the diffusion metasurface can be obtained in a way independent of the particulars of the setup. Furthermore, the metric evaluates the average performance, which is not biased towards a particular scattering pattern. We demonstrate the significance of the proposed metric through benchmarking of two specific metasurface architectures. In particular, we show that the integral-based metric allows for meaningful discrimination between alternative metasurface setups (e.g., checkerboard versus random) even though traditional metrics remain inconclusive. The results indicate that the proposed metric may be a useful tool in the design of scattering metasurfaces featuring improved RCS-reduction performance.

The remaining part of the article is organized as follows. Section 2 discusses the motivation of the introduced Normalized Partial Scattering Cross Section (NPSCR). In Section 3, the underlying concepts behind RCS of scattering metasurfaces are provided, followed by a brief description of the proposed integral-based metric. In Section 4, we demonstrate the significance and practical utility of the integral-based metric using two benchmark examples. Section 5 concludes this paper.

2. Motivation

The key performance indicator in the design of low scattering metasurface is the RCS reduction characteristics. The design can be evaluated under two types of scattering conditions, i.e., the monostatic or bistatic ones. Therein, a realistic environment can be characterized to assess the practical performance of a surface.

The advent of a multi-base radar detection technology demands contemporary stealth structures to feature nominal RCS. The standard monostatic and bistatic regimes are illustrated in Figure 1. As shown, the transmitter and the receiver radars are separated by a

certain distance. In a bistatic mode, the angle between the receiver radar and reflected EM waves are denoted by β and is referred to as a bistatic angle [27]. It can be observed from Figure 1 that the bistatic RCS solely depends on the selection of the measuring plane, i.e., it is increased whenever the plane misses the scattering lobes and drops otherwise. Therefore, the nature of bistatic characteristics restricts their evaluation to only a single direction (angle) at a specific instance. Consider Figure 2, where the bistatic RCS performance of a considered metasuface is evaluated along the three scattering angles, $\beta = 10°, 35°,$ and $75°$. Expectedly, the results are dependent on the angle of observation. In particular, the best RCS reduction does not endure at all of the tested angles, and similarly, it varies along the plane [27–29].
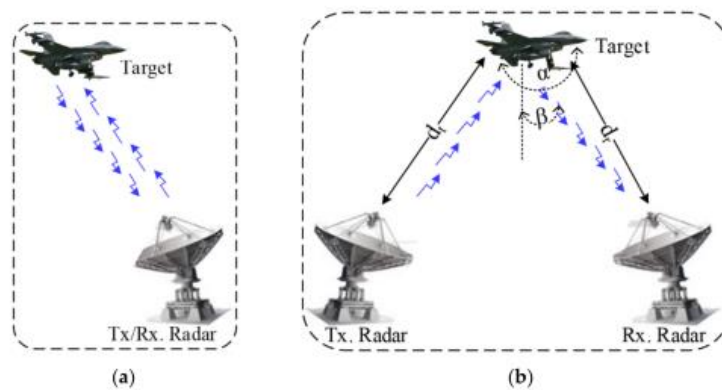
Figure 1. Illustration of (**a**) a monotonic, and (**b**) bistatic mode of operation.
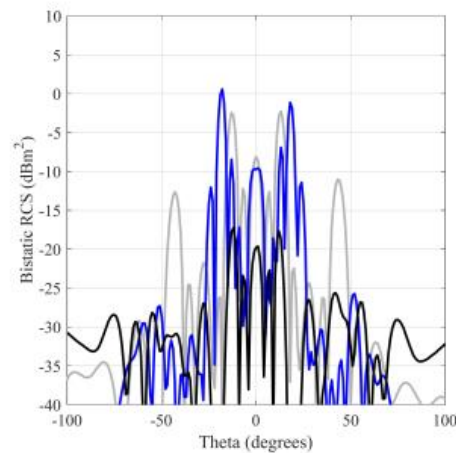
Figure 2. Exemplary bistatic RCS characteristics at an observation angle $\beta = 10°$ (gray), $35°$ (blue) and $75°$ (black).

This implies that bistatic performance evaluated at a few selected angles or planes is insufficient to deliver a comprehensive account for the metasurface properties, which becomes problematic especially in the design process of high-performance RCS-reduction metasurfaces. The bistatic RCS characteristics given in Figure 2 are obtained by evaluating metasurface IV (cf. Section 4). Consequently, a new metric should be developed that

alleviates the difficulties of the existing methods and is more aligned with the contemporary needs, including those pertinent to design procedures. In this regard, evaluating RCS properties along a specified angular spread (e.g., a cone determined by a solid angle α, see Figure 1) may deliver a more conclusive assessment of the bistatic performance of a surface.

3. Proposed Metric

This section briefly describes the underlying concepts behind RCS of scattering metasurfaces, and anchor these to monostatic and bistatic characteristics. Later on, we give a formal definition of a novel performance metric proposed in this work. Its utility in the context of metasurface design and evaluation will be demonstrated in Section 4.

3.1. Background Information

The mechanism of a monostatic and bistatic RCS can be understood by recalling a planar array excited with a progressive phase shift of 180° over a certain frequency band [23, 300]. The metasurface exploits the anti-phase reflection property of periodic arrays to control the scattered energy.

To quantitatively illustrate the physical phenomenon, we consider a generalized configuration of a metasurface (cf. Figure 3) that contains $N \times N$ equally-sized lattices of dimension d. The scattering phase of each lattice is assumed to be $\phi(m,n)$. Under the normal incidence of the plane waves, the far-field array factor corresponding to the energy scattered by a metasurface [23] is given as

$$AF(\theta, \phi, f) = E_e(\theta, \phi, f)$$
$$\sum_{m=1}^{N} \sum_{n=1}^{N} \exp\{-i\{\phi(m,n) + kd \sin\theta[(m - 1/2)\cos\phi + (n - 1/2)\sin\phi]\}\} \tag{1}$$

where θ and φ denote the elevation and the azimuth angles of a scattering direction, respectively, f denotes the specified frequency and $E_e(\theta,\phi,f)$ is the pattern function of a lattice at a frequency f. Subsequently, the overall directivity of the metasurface can be obtained as

$$D(\theta, \phi, f) = \frac{4\pi |AF(\theta, \phi, f)|^2}{\int_0^{180} \int_0^{90} |AF(\theta, \phi, f)|_2 \sin\theta d\theta d\phi} \tag{2}$$

On the other hand, the principle of RCS reduction is based upon redirecting the incident EM energy to all directions in the space. More specifically, the RCS of a corresponding surface at the scattering angles θ and φ at the frequency f can be expressed as

$$\sigma(\theta, \phi, f) = \lambda^2 [4\pi N^2 d^2]^{-1} D(\theta, \phi, f) \tag{3}$$
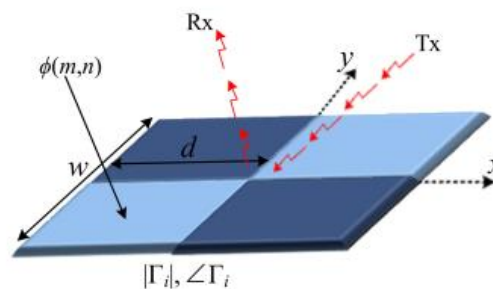
where λ is the free space wavelength.

Figure 3. A simple configuration of a $N \times N$ metasurface.

Note that the monostatic RCS refers to a specific θ and φ (e.g., $\sigma(0,0,f)$, where $\theta = 0°$ and $\varphi = 0°$) at a frequency f. Alternatively, bistatic RCS corresponds to $\sigma(\theta,\varphi,f)$, with $-90° \leq \theta \leq 90°$, whereas φ determines the evaluation plane (e.g., $0°$ or $90°$).

3.2. Novel Integral-Based Performance Metric

As indicated in Section 1, characterization of the RCS reduction using both the monostatic and bistatic approaches is generally insufficient in terms of providing comprehensive assessment of metasurface performance, especially in the light of modern circumstances (e.g., multi-base radars). Furthermore, bistatic RCS may be misleading due to being highly dependent on the choice of the evaluation planes.

In order to mitigate these issues, this work proposes a novel, integral-based, performance metric, referred to as Normalized Partial Scattering Cross Section (NPSCR). It is be defined as the metric involving numerical integration of the energy scattered from the target over a solid angle $\Omega = (\theta,\phi) \in [\theta_{min}, 90°] \times [-180°, 180°]$, where θ_{min} is the angle defining the considered range Ω. Analytically, it is formulated as

$$\sigma_\Omega(f) = \left| \frac{\oiint \sigma(\Omega, f)d\Omega}{\oiint \sigma^P(\Omega, f)d\Omega} \right| \tag{4}$$

where σ^P is the RCS of a perfect electric conductor (PEC) having the same physical dimension. In other words, σ_Ω represents the RCS of the corresponding metasurface averaged over a solid angle Ω normalized to the same of the PEC surface. A scalarized version of the metric, which may be more convenient for, e.g., design optimization purposes, is defined as

$$\sigma = [f_U - f_L]^{-1} \int_{f_L}^{f_U} \sigma_\Omega(f) \, df \tag{5}$$

where f_L and f_U determine the frequency range of interest. Thus, σ is the average RCS performance over the frequency interval $[f_L, f_H]$.

An important advantage of the metrics (4) and (5) is that it is not biased towards a particular scattering pattern. As a result, a conclusive assessment concerning the observable properties of the diffusion metasurface can be obtained in a way independent of the particulars of the setup (e.g., the choice of the evaluation plane for a bistatic mode). It should be noted that NPSCR exhibits certain resemblance to the Scattering Cross Section [30], although it is more specific in terms of being defined over a pre-defined frequency spectrum and the angular spread of the scattering directions.

4. Numerical Results and Discussions

This section demonstrates the significance and practical utility of the integral-based metric introduced in Section 3, using two specific metasurface examples. We start by benchmarking the two architectures of similar underlying designs but with different arrangement of the lattices. Subsequently, we consider performance discrimination between the four alternative metasurface designs.

4.1. Case Study I

Our first verification case is a coding metasurface employing crusader-cross-shaped unit cells. The structure is implemented on a ground-backed Arlon AD250 lossy substrate ($\varepsilon r = 2.5$, $h = 1.5$ mm, $\tan\delta = 0.0018$). The overall size of each surface is $W \times L = 144 \times 144$ mm^2. The topology of the cell, and the two configurations of the metasurface are shown in Figures 4 and 5, respectively. For the sake of brevity, we omit the detailed information about cell parameterization (cf. [31]). The CST Microwave Studio is used to evaluate the field performance of all metasurfaces considered in this work.
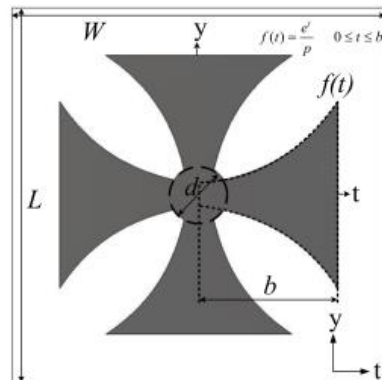
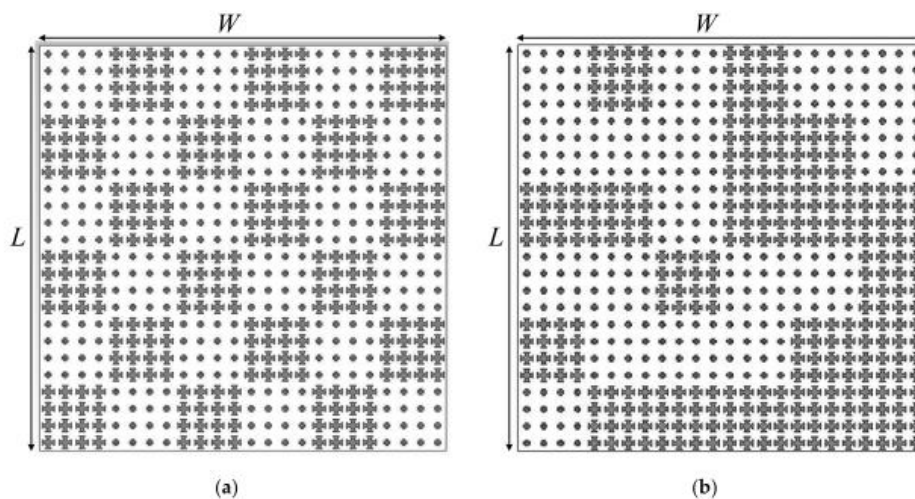**Figure 4.** Topology of the crusader-cross-shaped unit cell.

Figure 5. (a) Configuration of the checkerboard; (b) optimized metasurface architectures.

One of the considered metasurfaces is a standard checkerboard configuration, whereas in the second case, the composition of the lattices is determined by globally optimizing (1) using binary coded genetic algorithm, as presented in [28].

Our target is to assess the RCS reduction performance of the two architectures, thus determining the recommended structure. First, we attempt to discriminate between the two structures by means of the existing measures of merits, i.e., the monostatic and bistatic RCS. Figure 6 shows the monostatic and bistatic RCS performance of the two designs. It can be observed that neither of these metrics allows for conclusive determination of the better-performing structure. On the one hand, considering the monostatic RCS characteristics, the optimized metasurface is superior. On the other hand, the checkerboard architecture features lower bistatic RCS than the optimized surface; however, this is only for a specific plane, and a specific frequency. As mentioned before, bistatic evaluation is ambiguous mainly due to dependence of the plane selection and the particular scattering pattern of the surface.
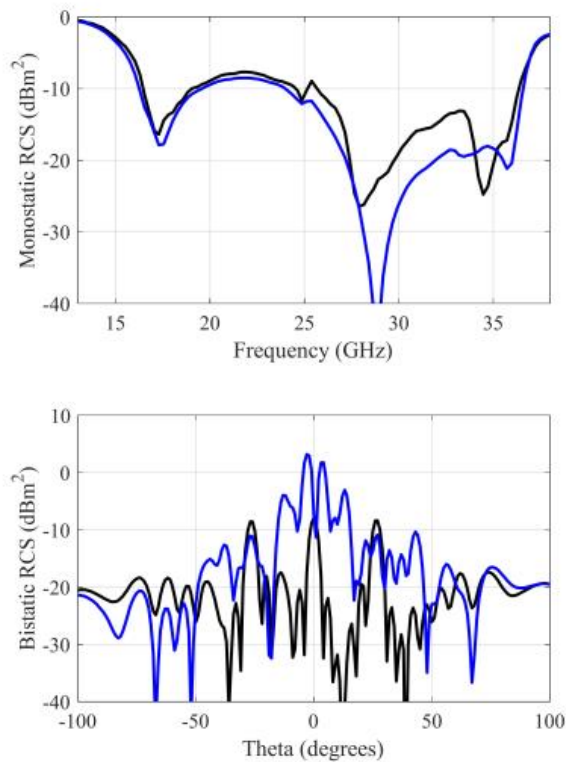
Figure 6. Monostatic (**top**) and bistatic at 28 GHz (**bottom**) RCS characteristics of the two metasurfaces. The bistatic RCS is evaluated at $\theta = 0°$ and $\varphi = 0°$. The monostatic performance is normalized to the reference PEC surface. The black and blue color corresponds to checkerboard and optimized metasurface performance, respectively.

At this point, we apply the proposed integral-based metric to evaluate the considered architectures. Figure 7 shows two cases, parameterized by the solid angle: $\theta_{min} = 30°$ (i.e., $\Omega = [30°, 90°] \times [-180°, 180°]$) and $\theta_{min} = 45°$ (i.e., $\Omega = [45°, 90°] \times [-180°, 180°]$) (cf. Section 3.2). It can be observed that regardless of θ_{min}, the optimized metasurface features better RCS reduction properties than the checkerboard version over a wide range of frequencies. Furthermore, the average RCS performance (cf. (5)) for the checkerboard and the optimized metasurfaces is 11.49 and 20.87 for $\theta_{min} = 30°$; for $\theta_{min} = 45°$ the figures are 11.56 and 20.89, respectively. Please note that the end-result in Figure 7 involves integration of the overall scattering performance of the metasurface, therefore, the response at two solid angles, i.e., at $\theta_{min} = 30°$ and $\theta_{min} = 45°$, seem to be almost the same. Thus, the optimized metasurface is conclusively superior in terms of the integral-based metric.
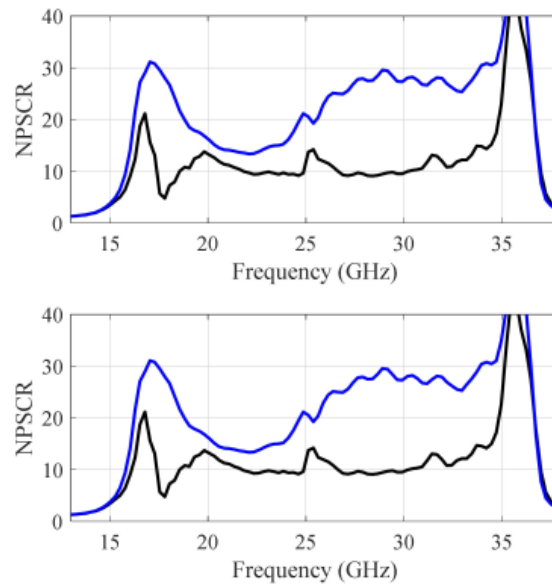
Figure 7. RCS performance evaluated using NPSCS of (4) when $\theta_{min} = 30°$ (**top**) and when $\theta_{min} = 45°$ (**bottom**). The black and blue color corresponds to checkerboard and optimized metasurface performance, respectively.

4.2. Case Study II

The second demonstration example involves four metasurfaces implemented using entirely different unit cell topologies as shown in Figure 8. The first metasurface is based on a design of [25], the second, and the third ones were presented in [28,29], respectively, hereafter referred to as metasurface I, II, and III, respectively. The fourth surface involves the underlying unit cell topology as given in Figure 4, hereafter referred to as metasurface IV. All the designs are further adjusted to obtain the optimal performance in the sense of maximizing monostatic RCS reduction bandwidth.

In this study, the aim is to quantify the RCS reduction performance of these metasurface architectures using the integral-based metric. For fair assessment, the comparison is carried out in terms of the average RCS performance (5) calculated over the frequency intervals corresponding to the 10 dB monostatic RCS reduction bandwidths of the respective surfaces. For each case, five angular spreads are considered, parameterized by the solid angle: $\theta_{min} = 10°, 20°, 30°, 40°, 50°$ (i.e., $\Omega = [\theta_{min}, 90°] \times [-180°, 180°]$), cf. Section 3.2. The results are presented in Table 1. It can be observed that metasurfaces III and IV are superior over metasurfaces I and II for $\theta_{min} \geq 20°$, and their performance is similar to each other. This means that for the vast majority of operating conditions in terms of θ_{min}, the last two structures are conclusively better and the difference is significant (performance improvement by a factor of about 2.5 over the first two structures). Only for the lowest value, $\theta_{min} = 10°$, does metasurface I exhibit the best properties.
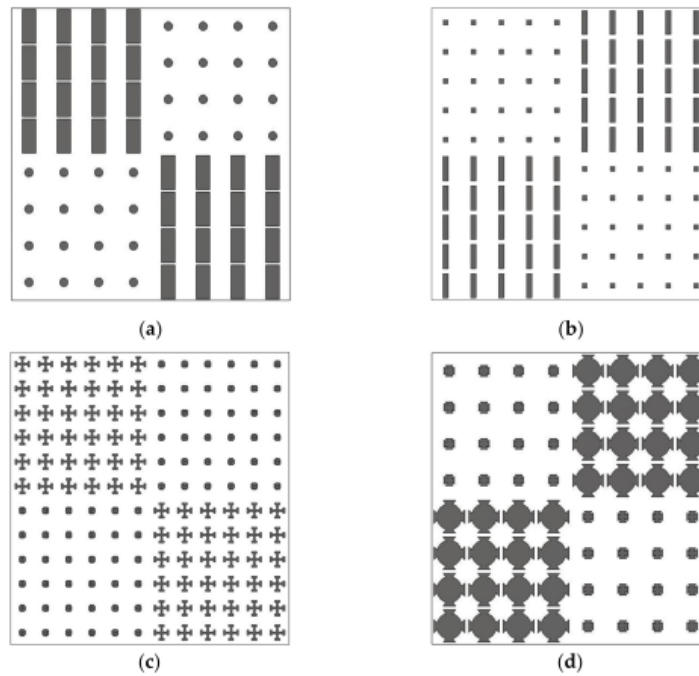
Figure 8. Configuration of the metasurfaces; (**a**) metasurface I [25], (**b**) metasurface II [28], (**c**) metasurface III [29], and (**d**) metasurface IV.

Table 1. Performance Comparison of Different Metasurface Designs.

Design	Polarization Dependent	Average RCS Performance (5)				
		$\theta_{min} = 10°$	$\theta_{min} = 20°$	$\theta_{min} = 30°$	$\theta_{min} = 40°$	$\theta_{min} = 50°$
Metasurface I	Yes	37.0	5.2	4.4	4.3	4.3
Metasurface II	Yes	14.2	5.1	4.2	4.0	3.9
Metasurface III	-	13.9	12.0	10.4	9.9	9.7
Metasurface IV	No	15.6	10.1	9.8	9.2	9.1

It should be reiterated that the proposed metric is independent of the choice of the evaluation plane (as in the case of bistatic performance), which seems to be much more practical having in mind that the specific spatial (and angular) relationship between the target (e.g., an aircraft) and the ground infrastructure (radar) is unknown beforehand.

5. Conclusions

This paper introduces a new performance metric, referred to as Normalized Partial Scattering Cross Section (NPSCS), for quantifying scattering properties of the metasurfaces. It entails evaluating the total energy scattered from the target over a solid angle. NPSCS allows for a conclusive assessment of the observability properties of the diffusion metasurface, which can be obtained in a way independent of the particulars of the setup (e.g., the choice of the evaluation plane for a bistatic mode). Moreover, the metric evaluates the average performance, which is not biased towards a particular scattering pattern. The significance and practical utility of NPSCS has been demonstrated by benchmarking two pertinent metasurface examples. The results indicate that the NPSCS complements the

existing metrics. In particular, it can be considered a potentially attractive evaluation tool in the design of scattering metasurfaces featuring improved RCS-reduction performance. A potential disadvantage of the proposed metric is its slightly more involved formulation, which required numerical integration to evaluate NPSCS; however, when implemented using a specific programming environment, this complexity is hidden from the user.

Author Contributions: Conceptualization, M.A. and S.K.; methodology, M.A.; software, M.A. and S.K.; validation, S.S.; formal analysis, S.K.; investigation, M.A.; writing—original draft preparation, M.A.; writing—review and editing, S.K.; visualization, S.S.; supervision, S.K.; project administration, S.K. and S.S.; funding acquisition, S.K. and S.S. All authors have read and agreed to the published version of the manuscript.

Conflicts of Interest: The authors declare no conflict of interest.

References

1. Sun, S.; He, Q.; Hao, J.; Xiao, S.; Zhou, L. Electromagnetic meta-surfaces: Physics and applications. *Adv. Opt. Photon.* **2019**, *11*, 380–479. [CrossRef]
2. Cui, T.J.; Smith, D.R.; Liu, R. *Metamaterials: Theory, Design and Applications;* Springer: New York, NY, USA, 2010.
3. Huang, F.-C.; Chiu, C.-N.; Wu, T.-L.; Chiou, Y.-P. A Circular-Ring Miniaturized-Element Metasurface With Many Good Features for Frequency Selective Shielding Applications. *IEEE Trans. Electromagn. Compat.* **2015**, *57*, 365–374. [CrossRef]
4. Li, A.; Singh, S.; Sievenpiper, D. Metasurfaces and their applications. *Nanophotonics* **2018**, *7*, 989–1011. [CrossRef]
5. Achouri, K.; Lavigne, G.; Salem, M.; Caloz, C. Metasurface Spatial Processor for Electromagnetic Remote Control. *IEEE Trans. Antennas Propag.* **2016**, *64*, 1759–1767. [CrossRef]
6. Gao, X.; Han, X.; Cao, W.-P.; Li, H.O.; Ma, H.F.; Cui, T.J. Ultrawide-band and high-efficiency linear polarization converter based on double V-shaped metasurface. *IEEE Trans. Antennas Propag.* **2015**, *63*, 3522–3530. [CrossRef]
7. Westwick, P. *Stealth: The Secret Contest to Invent Invisible Aircraft;* Oxford Univ. Press: London, UK, 2019; pp. 5–42.
8. Wang, Y.; Chen, K.; Li, Y.; Cao, Q. Design of nonresonant metasurfaces for broadband RCS reduction. *IEEE Ant. Wireless Propag. Lett.* **2021**, *20*, 346–350.
9. Hou, Y.; Liao, W.; Tsai, C.; Chen, S. Planar multilayer structure for broadband broad-angle RCS reduction. *IEEE Trans. Antennas Propag.* **2016**, *64*, 1859–1867. [CrossRef]
10. Kim, S.H.; Yoon, Y.J. Wideband Radar Cross-Section Reduction on Checkerboard Metasurfaces With Surface Wave Suppression. *IEEE Antennas Wirel. Propag. Lett.* **2019**, *18*, 896–900. [CrossRef]
11. Cao, T.H.X.-Y.; Gao, J.; Zhao, Y.-L.; Zhao, Y. A coding metasurface with properties of absorption and diffusion for RCS reduction. *Prog. Electromagn. Res. C* **2017**, *75*, 181–191.
12. FCosta, F.; Monorchio, A.; Manara, G. Wideband Scattering Diffusion by using Diffraction of Periodic Surfaces and Optimized Unit Cell Geometries. *Sci. Rep.* **2016**, *6*, 25458.
13. Zhao, Y.; Cao, X.; Gao, J.; Sun, Y.; Yang, H.; Liu, X.; Zhou, Y.; Han, T.; Chen, W. Broadband diffusion metasurface based on a single anisotropic element and optimized by the Simulated Annealing algorithm. *Sci. Rep.* **2016**, *6*, 23896. [CrossRef] [PubMed]
14. Yang, H.; Cao, X.; Yang, F.; Gao, J.; Xu, S.; Li, M.; Chen, X.; Zhao, Y.; Zheng, Y.; Li, S. A programmable metasurface with dynamic polarization, scattering and focusing control. *Sci. Rep.* **2016**, *6*, 35692. [CrossRef] [PubMed]
15. Chen, M.; Kim, M.; Wong, A.; Eleftheriades, G.V. Huygens' metasurfaces from microwaves to optics: A review. *Nanophotonics* **2018**, *7*, 1207–1231. [CrossRef]
16. Ji, J.; Jiang, J.; Chen, G.; Liu, F.; Ma, Y. Research on monostatic and bistatic RCS of cloaking based on coordinate transformation. *Opt.* **2018**, *165*, 117–123. [CrossRef]
17. Sui, S.; Ma, H.; Wang, J.; Pang, Y.; Feng, M.; Xu, Z.; Qu, S. Absorptive coding metasurface for further radar cross section reduction. *J. Phys. D Appl. Phys.* **2017**, *50*, 465102. [CrossRef]
18. Al-Nuaimi, M.K.T.; Hong, W.; Whittow, W.G. Aperiodic sunflower-like metasurface for diffusive scattering and RCS reduction. *IEEE Ant. Wireless Propag. Lett.* **2020**, *19*, 1048–1052. [CrossRef]
19. Ali, L.; Li, Q.; Khan, T.A.; Yi, J.; Chen, X. Wideband RCS Reduction Using Coding Diffusion Metasurface. *Materials* **2019**, *12*, 2708. [CrossRef] [PubMed]
20. Liu, X.; Gao, J.; Xu, L.; Cao, X.; Zhao, Y.; Li, S. A Coding Diffuse Metasurface for RCS Reduction. *IEEE Antennas Wirel. Propag. Lett.* **2017**, *16*, 724–727. [CrossRef]
21. Zhuanget, Y.; Wang, G.; Liang, J.; Cai, T.; Guo, W.; Zhang, Q. Flexible and polarization-controllable diffusion meta-surface with optical transparency. *J. Phys. D Appl. Phys.* **2017**, *50*, 465102. [CrossRef]
22. Rao, G.A.; Mahulikar, S.P. Integrated review of stealth technology and its role in airpower. *Aeronaut. J.* **2002**, *106*, 629–642.
23. Cui, T.J.; Qi, M.Q.; Wan, X.; Zhao, J.; Cheng, Q. Coding metamaterials, digital metamaterials and programmable metamaterials. *Light. Sci. Appl.* **2014**, *3*, e218. [CrossRef]

24. Knott, E.F. *Radar Cross Section Measurements*; Springer: Berlin/Heidelberg, Germany, 2012; pp. 12–36.
25. Abdullah, M.; Koziel, S. Surrogate-Assisted Design of Checkerboard Metasurface for Broadband Radar Cross-Section Reduction. *IEEE Access.* **2021**, *9*, 46744–46754. [CrossRef]
26. Edalati, A.; Sarabandi, K. Wideband, wide angle, polarization independent RCS reduction using nonabsorptive miniaturized-element frequency selective surfaces. *IEEE Trans. Antennas Propag.* **2014**, *62*, 747–754. [CrossRef]
27. Lee, S.-J.; Choi, I.-S.; Rothwell, E.J.; Temme, A.K. Determination of optimum bistatic angle for radar target identification. *J. Electromagn. Waves Appl.* **2014**, *28*, 551–562. [CrossRef]
28. Khan, T.A.; Li, J.; Chen, J.; Raza, M.U.; Zhang, A. Design of a Low Scattering Metasurface for Stealth Applications. *Materials* **2019**, *12*, 3031. [CrossRef] [PubMed]
29. Iriarte, J.C.; Perada, A.T.; Martinez, J.L.; Ederra, I.; Gonzalo, R.; de Maagt, P. Broadband radar cross-section reduction using AMC technology. *IEEE Trans. Antennas Propag.* **2013**, *61*, 6136–6143. [CrossRef]
30. Modi, A.Y.; Balanis, C.A.; Birtcher, C.R.; Shaman, H.N. New Class of RCS-Reduction Metasurfaces Based on Scattering Cancellation Using Array Theory. *IEEE Trans. Antennas Propag.* **2018**, *67*, 298–308. [CrossRef]
31. Koziel, S.; Abdullah, M. Machine-learning-powered EM-based framework for efficient and reliable design of low scattering metasurfaces. *IEEE Trans. Microw. Theory Techn.* **2021**, *69*, 2028–2041. [CrossRef]

Chapter 8

8   Conclusion and Future Directions

This chapter provides a brief summary of the thesis and outlines possible future research directions that might originate from the work carried out so far, but also addresses a number of open problems related to the design of scattering metasurfaces for modern stealth systems, as well as other practical applications.

8.1   Conclusion

The main focus of this work was to develop computationally efficient surrogate-modelling-based procedures for design of scattering metasurface architectures, including dedicated algorithmic frameworks for metasurface optimization. The obtained numerical and experimental results indicate that the goals of this dissertation have been accomplished, and results have been positively validated.

As demonstrated, appropriate combination of the design task formulation developed having in mind the problem-specific knowledge (e.g., possible issues related to discontinuities of the objective functions), data-driven strategies, fast-to-evaluate replacement models, surrogate-assisted techniques, and EM-driven fine tuning, allow for efficient design optimization of computationally expensive EM models of scattering metasurface structures. The latter is particularly desirable in the stealth technology, empowering combat aircrafts to potentially evade the enemy's radar to a satisfactory extent. In a similar vein, the cost of obtaining accurate replacement models (pertinent for the considered design frameworks) grows very quickly with dimensionality of the design space. These, and other challenges have been addressed in the course of this work. Furthermore, several metasurface configurations have been considered, employed as verification cases to test the efficacy of our design frameworks, but also optimized to provide high-performance alternatives to the existing metasurface configurations.

It should be emphasized that machine-learning-based algorithmic framework introduced in this study offers several advantages over conventional design methodologies, such as global exploration capability, EM-driven fine tuning facilitated by a decent initial design rendered at global search stage, along with the explicit control over the RCS reduction characteristics at the level of unit-cell design. Furthermore, the considered design optimization approach has led to the development of novel metasurfaces featuring broadband RCS reduction performance. Specific contributions in all aspects of the work have been detailed in the previous chapters.

8.2 Future Directions

The work conducted for the purpose of this dissertation can be extended in many different directions related to the design optimization of scattering metasurfaces for modern stealth systems as well as other applications. Some important topics that might be considered include:

1. The design frameworks developed in this thesis can be adopted to design metamaterials and metasurfaces for other application areas so as to address the challenges specific to the respective fields. These include but are not limited to high-gain antennas, absorbers, frequency selective surfaces (FSS), optical filters, radomes, and medical devices, but also for conducting pertinent studies, among others, on suitability of particular algorithmic solutions/modifications for design optimization in these applications;

2. In this study, we mostly rely on data-driven strategy to obtain optimal unit-cell geometries. However, it is worth mentioning that more generic approaches are also possible, where parametric optimization of the unit-cells (and the metasurface) of a fixed geometry is replaced by topology optimization. In this case, the entire geometry of the metasurface is subject to the optimization process, which brings in additional degrees of freedom. This type of optimization tasks could be realized by means of the inverse modelling methods;

3. Another (quantitatively significant) enhancement would be to completely change the strategy of arranging the arrays unit-cells in a coding metasurface configuration, i.e., to use deterministic procedures rather than metaheuristic. This could be realized by finding the path connecting the optimal designs using methods similar to pattern search and operating directly on surrogate-based replacement models;

4. Although non-planar structures seem to be more widespread in real-life applications, in this dissertation, we focused on planar structures because of the ease of fabrication. Nevertheless, our design optimization frameworks, and proposed designs for RCS reduction are quite feasible for both conformal and curved structures. Specifically, flexible material and direct wave printing or prismatic structures can be used for such purpose, which—however— significantly increases the fabrication cost;

5. Altogether, this study can be considered a step towards exploring potential applications of machine learning techniques in a high-frequency design, specifically, in the realm of low-observability systems, where intuition-inspired methods are still predominantly employed as foundations of the design procedures. With the development of machine learning techniques, an increasing contribution of automated CAD approaches can be fostered, among others, to learn the physical behaviour of the system response to input parameters, under controlled boundary conditions. This work demonstrates one promising application field, i.e., predicting the reflection response in real-time-computation.

Bibliography

[1]   T. P. Ehrhard, *Air Force UAV's: The Secret History*. Mitchell Inst for Airpower Studies Arlington VA, 2010.

[2]   K. Zikidis, A. Skondras, and C. Tokas, "Low observable principles, stealth aircraft and anti-stealth technologies," *Journal of Computations & Modelling*, vol. 4, no. 1, pp. 129–165, 2014.

[3]   M. E. Brown, "8. The Politics of Stealth: The B-1B and B-2." *Flying Blind*. Cornell University Press, pp. 268–304, 2019.

[4]   D. Summerfield, D. Raslau, B. Johnson, and L. Steinkraus, "Physiologic challenges to pilots of modern high performance aircraft," *Aircraft technology*, pp. 43–73, 2018.

[5]   K. K. Agnihotri, "Modernisation of the Chinese Air Force and its implications for India." *Maritime Affairs: Journal of the National Maritime Foundation of India* 7.2, pp. 33–49, 2011.

[6]   E. F. Knott, J. F. Schaeffer, and M. T. Michael, *Radar cross section*, SciTech Publishing, Raleigh, NC, 2004.

[7]   T. A. Khan, J. X. Li, Z. Li, M. Abdullah, J. Chen, and A. X. Zhang, "Design of Vivaldi antenna with wideband reduced radar cross section," *AEU International Journal of Electronics and Communications*, vol. 95, pp. 47–51, 2018.

[8]   M. Paquay, J. -C. Iriarte, I. Ederra, R. Gonzalo, and P. de Maagt, "Thin AMC structure for radar cross-section reduction," *IEEE Transactions on Antennas and Propagation*, vol. 55, no. 12, pp. 3630–3638, 2007.

[9]   Y. Zhao, X. Cao, J. Gao, Y. Sun, H. Yang, X. Liu, Y. Zhou, T. Han, and W. Chen, "Broadband diffusion metasurface based on a single anisotropic element and optimized by the simulated annealing algorithm," *Scientific Reports*, vol. 6, p. 23896, 2016.

[10]   M. Panda, P. Samaddar, and P. Sarkar, "Artificial neural network for the analysis and design of a frequency selective surface with slits," *International Journal of Chemical and Environmental Sciences*, vol. 3, pp. 81—83, 2013.

[11]   U. Hakan, "Radar cross section reduction," *Deniz Bilimleri ve MühendisliÉi Dergisi*, vol. 9, no. 2, 2013.

[12]   M. Paquay, J. -C. Iriarte, I. Ederra, R. Gonzalo, and P. de Maagt, "Thin AMC structure for radar cross-section reduction," *IEEE Transactions on Antennas and Propagation*, vol. 55, no. 12, pp. 3630-3638, 2007.

[13]   C. A. Balanis, *Advanced Engineering Electromagnetics*. 2nd ed., John Wiley & Sons, Hoboken, 2012.

[14]   R. F. Harrington, *Time-Harmonic Electromagnetic Fields*. 1st ed., McGrawHill, New York, 1965.

[15]   R. E. Collin, *Field Theory of Guided Waves*. 1st ed., IEEE Press, New York, 1991.

[16] R. E. Collin, *Foundations for microwave engineering*. 1st ed., McGraw-Hill, New York, 1966.

[17] D. M. Pozar, *Microwave Engineering*. 4th ed., Wiley, New York, 2012.

[18] C. A. Balanis, *Antenna Theory: Analysis and Design*. 4th ed., John Wiley & Sons, Hoboken, 2016.

[19] R. C. Hansen, *Phased array antennas*. John Wiley & Sons, 2009, vol. 213.

[20] A. Y. Modi, *Metasurface-Based Techniques for Broadband Radar Cross-Section Reduction of Complex Structures*. PhD diss., Arizona State University, 2020.

[21] E. F. Knott, M. T. Tuley, and J. F. Shaeer, *Radar cross section*. 2nd ed., Artech House, Norwood, MA, USA, 1993.

[22] A. Aul and N. Engheta, "Cloaking a sensor," *Physical Review Letters*, vol. 102, no. 23, p. 233901, 2009.

[23] M. Selvanayagam and G. V. Eleftheriades, "Experimental demonstration of active electromagnetic cloaking," *Physical review X*, vol. 3, no. 4, p. 041011, 2013.

[24] B. A. Munk, *Frequency selective surface: Design and theory*, Wiley, New York, 2000.

[25] F. Yang and Y. Rahmat-Samii, *Electromagnetic band gap structures in antenna engineering*. Cambridge, University Press Cambridge, UK, 2009.

[26] R. Paknys, *Applied frequency-domain electromagnetics*. John Wiley & Sons, 2016.

[27] J. N. Reddy, *Introduction to the finite element method*. McGraw-Hill Education, 2019.

[28] S. D. Gedney, *Introduction to the Finite-Difference Time-Domain (FDTD) method for electromagnetics*, Morgan & Claypool, 2011.

[29] Y. Kim, F. Yang, and A. Z. Elsherbeni, "Compact artificial magnetic conductor designs using planar square spiral geometries," *Progress in Electromagnetics Research*, vol. 77, pp. 43–54, 2007.

[30] A. P. Feresidis, G. Goussetis, S. Wang, and J. C. Vardaxoglou, "Artificial magnetic conductor surfaces and their application to low-profile high-gain planar antennas," *IEEE Transactions on Antennas and Propagation*, vol. 53, no. l , pp. 209–215, 2()05.

[31] J. Epis, "Broadband antenna polarizer," Aug. 21 1973, US Patent 3,754,271.

[32] D. Sievenpiper, L. Zhang, R. F. Broas, N. G. Alexopolous, and E. Yablonovitch, "High impedance electromagnetic surfaces with a forbidden frequency band," *IEEE Transactions on Microwave Theory and Techniques*, vol. 47, no. 1 1, pp. 2059–2074, 1999.

[33] M. E. d. Cos G6mez, F. L. Las Heras Andrés et al., "Novel flexible artificial magnetic conductor," *International Journal of Antennas and Propagation*, vol. 2012, Article 353821, 2012.

[34] D. Sievenpiper, L. Zhang, R. F. J. Broas, N. G. Alexopolous, and E. Yablonovitch, „High-impedance electromagnetic surfaces with a forbidden frequency band," *IEEE*

Transactions on Microwave Theory and Techniques, vol. 47, no. 11, pp. 2059–2074, 1999.

[35]   F. Samadi, M. Akbari, M. R. Chaharmir, and A. R. Sebak, "Wideband RCS suppression based on FSS structures for millimeter applications," in *2017 XXXIInd General Assembly and Scientific Symposium of the International Union of Radio Science (URSI GASS)*, 2017, PP. 1–3.

[36]   F. Samadi, M. Akbari, M. R. Chaharmir, and A. R. Sebak, "Scattering behavior of AMC chessboard for RCS reduction application," in *2017 XXXIInd General Assembly and Scientific Symposium of the International Union of Radio Science (URSI GASS)*, 2017, pp. 1–4.

[37]   C. Simovski, P. De Maagt, S. Tretyakov, M. Paquay, and A. Sochava, "Angular stabilisation of resonant frequency of artificial magnetic conductors for TE-incidence," *Electronics Letters*, vol. 40, no. 2, pp. 92–93, 2004.

[38]   D. D. King, "The measurement and interpretation of Antenna scattering," *Proceedings of the IRE*, vol. 37, no. 7, pp. 770–777, 1949.

[39]   S. H. Dike and D. D. King, "The absorption Gain and back scattering cross section of the cylindrical Antenna," *Proceedings of the IRE,* vol. 40, no.7, pp. 853–860, 1952.

[40]   R. B. Green, "The general theory of antenna scattering," *Southern Journal of Philosophy,* vol. 6, no. 2, pp. 108–114, 1963.

[41]   M. Basravi, M. Maddahali, Z. L. Firouzeh, et al., "Design of a novel ultra broadband single layer absorber usingdouble fractal square loops," *24th Iranian Conference on Electrical Engineering (ICEE)*, Shiraz, Iran, 2016.

[42]   A. P. Sohrab and Z. Atlasbaf, "A circuit analog absorber with optimum thickness and response in X-band," *IEEE Antennas & Wireless Propagation Letters*, vol. 12, pp. 276–279, 2013.

[43]   Y. Shang, Z. Shen, S. Xiao, "On the designing of single layer circuit analog absorber using double square loop array," *IEEE Transactions on Antennas & Propagation*, vol. 61, no. 12, pp. 6022–6029, 2013.

[44]   C. M. Dikmen, S. Cimen, and G. Cakir, "Planar octagonal shaped UWB antenna with reduced radar cross section," *IEEE Transactions on Antennas & Propagation*, vol. 62, no. 6, pp. 2946–2953, 2014.

[45]   J. B. Pendry, D. Shurig, D. R. Smith, "Controlling electromagnetic fields," *Science*, pp. 1780–1782, 2006.

[46]   U. Leonhardt, Optical conformal mapping," *Science*, pp. 1777–1780, 2006.

[47]   D. R. Smith, J. B. Pendry, and M. Wiltshire, "Metamaterials and negative refractive index," *Science*, pp. 788–792, 2004.

[48]   M. Paquay, J. C. Iriarte, and I. Ederra, "Thin AMC structure for radar cross section reduction," *IEEE Antennas & Wireless Propagation Letters*, vol. 55, no. 12, pp. 3630–3634, 2007.

[49] Y. Zhao, X. Cao, J. Gao, et al., "Broadband metamaterial surface for Antenna RCS reduction and gain enhancement," *IEEE Transactions on Antennas & Propagation*, pp. 1–1, 2015.

[50] Y. Zheng, J. Gao, X. Cao, et al., "Wideband RCS reduction of a Microstrip antenna using artificial magnetic conductors," *IEEE Antennas & Wireless Propagation Letters*, vol. 14, pp. 1582–1585, 2015.

[51] J. I. Galarregui, A.T. Pereda, J. L. Falcon, et al., "Broadband radar cross section reduction using AMC technology," *IEEE Transactions on Antennas & Propagation*, vol. 61, no. 12, pp. 6136–6143, 2013.

[52] L. Cong, X. Cao, J. Gao, et al., "Ultra wideband low RCS circularly polarized metasurface based array antenna using tightly coupled anistropic element," *IEEE Access*, vol. 6, pp. 41738–41744, 2018.

[53] Y. Liu, Y. Hao, H. Wang, et al., "Low RCS Microstrip patch antenna using frequency selective surface and microstrip resonator," *IEEE Antennas & Wireless Propagation Letters*, vol. 14, pp. 1290–1293, 2015.

[54] W. Chen, C. A. Balanis, C. R. Birtcher, et al., "Checkerboard EBG surfaces for wideband radar cross section reduction," *IEEE Transactions on Antennas & Propagation*, vol. 63, no. 6, pp. 2636–2645, 2015.

[55] Y. Liu, K. Li, Y. Jia, et al., "Wideband RCS reduction of a Slot array Antenna using polarization conversion metasurfaces," *IEEE Transactions on Antennas & Propagation*, vol. 64, no. 1, pp. 326–331, 2015.

[56] M. Long, W. Jiang, and S. Gong, "Wideband RCS reduction using polarization conversion metausrface and partially reflecting surface," *IEEE Antennas & Wireless Propagation Letters*, vol. 16, pp. 2534–2537, 2017.

[57] Y. Liu, Y. Hao, K. Li, et al., "Wideband and polarization independent radar cross section reduction using holographic metasurface," *IEEE Antennas & Wireless Propagation Letters*, vol. 15, pp. 1028–1031, 2016.

[58] T. J. Cui, M. Q. Qi, X. Wan. et al., Coding metamaterials, digital metamaterials and programmable metamaterials," *Light Science & Applications*, vol. 3, e218, 2014.

[59] B. Lusch, J. N. Kutz, and S. L. Brunton, "Deep learning for universal linear embeddings of nonlinear dynamics," *Nature Communications*, vol. 9, Art. no. 4950, 2018.

[60] X. Lin, Y. Rivenson, N. T. Yardimci, M. Veli, Y. Luo, M. Jarrahi, and A. Ozcan, "All-optical machine learning using diffractive deep neural networks," *Science.*, vol. 361, pp. 1004–1008, 2018.

[61] A. D. Tranter, H. J. Slatyer, M. R. Hush, A. C. Leung, et al., "Multiparameter optimisation of a magneto-optical trap using deep learning," *Nature Communications*, vol. 9, Art. no. 4360, 2018.

[62] J. Peurifoy, Y. Shen, L. Jing, Y. Yang, F. Cano-Renteria, et al., "Nanophotonic particle simulation and inverse design using artificial neural networks," *Science Advances*, vol. 4, Art. no. 4206, 2018.

[63] T. W. Simpson, J. D. Poplinski, P. N. Koch, and J. K. Allen, "Meta-models for computer-based engineering design: survey and recommendations," *Engineering Computations*, vol. 17, no. 2, pp. 129–150, 2001.

[64] X. Chen, W. Xue, H. Shi, J. Yi, and W. E. I Sha, "Orbital angular momentum multiplexing in highly reverberant environments," *IEEE Microwave Wireless Component Letters*, vol. 30, no. 1, pp. 112–115, 2020.

[65] X. Chen, W. Xue, H. Shi, L. Wang, S. zhu, and A. Zhang, "Improving field uniformity using source stirring with orbital angular momentum modes in a reverberation chamber," *IEEE Microwave Wireless Component Letters*, vol. 29, no. 8, pp. 560–562, 2019.

[66] S. Koziel and S. Ogurtsov, *Antenna design by simulation-driven optimization. Surrogate-based approach*. Springer, New York, 2014.

[67] S. Koziel and S. Ogurtsov, "Simulation-driven design in microwave engineering: Methods," In: S. Koziel S., X. S. Yang (Eds.) Computational Optimization, Methods and Algorithms. Studies in Computational Intelligence, vol 356. Springer, Berlin, 2011.

[68] X. S. Yang, *Engineering optimization: An introduction with metaheuristic applications*. Wiley, New York, 2010.

[69] J. Nocedal and S. J. Wright, *Numerical optimization*. Springer, New York, 2006.

[70] A. R. Conn, N. I. M. Gould, and P. L. Toint, *Trust-region methods*. Society for Industrial and Applied Mathematics, 2000.

[71] CST MICROWAVE STUDIO®, 2011, CST AG, Bad Nauheimer Str. 19, D-64289 Darmstadt, Germany.

[72] C. Portal, '{Ansys} {Hfss}', *ANSYS HFSS Featur.*, 2014.

[73] D. E. Goldberg, *Genetic algorithms in search, optimization, and machine learning*. Addison Wesley, Boston, MA,1989.

[74] T. Beck, D. B. Fogel, and Z. Michalewicz, *Evolutionary computation 1: Basic algorithms and operators. CRC Press*, Boca Raton, FL, 2000.

[75] R. C. Eberhart, J. Kennedy, and Y. Shi, *Swarm intelligence*. Elsevier, New York, 2001.

[76] R. Storn and K. Price, „Differential evolution - A simple and efficient heuristic for global optimization over continuous spaces," *Journal of Global Optimization*, vol. 11, pp. 341–359, 1997.

[77] F. J. Ares-Pena, J. A. Rodriguez-Gonzalez, E. Villanueva-Lopez, and S. R. Rengarajan, „Genetic algorithms in the design and optimization of antenna array patterns," *IEEE Transactions on Antennas & Propagation*, vol. 47, no. 3, pp. 506–510, 1999.

[78] P. J. Bevelacqua and C. A. Balanis, 'Optimizing antenna array geometry for interference suppression', *IEEE Transactions on Antennas & Propagation*, vol. 55, no. 3, pp. 637–641, 2007.

[79] S. Koziel and L. Leifsson, *Simulation-driven design by knowledge-based response correction techniques*. Springer, New York, 2016.

[80] T. W. Simpson, J. D. Poplinski, P. N. Koch, and J. K. Allen, "Metamodels for computer-based engineering design: survey and recommendations," *Engineering Computations*, vol. 17, no. 2, pp. 129–150, 2001.

[81] S. Koziel, L. Leifsson, and X. S. Yang, "Surrogate-based optimization," in *Simulation-Driven Design Optimization and Modeling for Microwave Engineering*, S. Koziel, X. S. Yang, and Q. J. Zhang, Eds. London, U.K.: Imperial College Press, 2012, pp. 41–80.

[82] S. Koziel and A. Pietrenko-Dabrowska, "Expedited optimization of antenna input characteristics with adaptive Broyden updates," *Engineering Computations*, vol. 37, no. 3, 2019.

[83] T. A. Khan, J. Li, J. Chen, M. U. Raza, and A. Zhang, "Design of a low scattering metasurface for stealth applications," *Materials*, vol. 12, no. 18, 3031, 2019.

[84] T. A. Khan, "Study on Wideband Low Radar Cross Section Antenna Designs," *MSc. dissertation*, Dept. Info. Comm. Eng., Xi'an Jiaotong Univ., Xi'an, China, 2019.
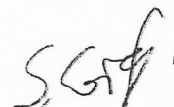
Department of Engineering
Reykjavík University
Menntavegur 1
102 Reykjavík, Iceland
Tel. +354 599 6200
Fax +354 599
www.ru.is

The undersigned hereby certify that they recommend to the Department of Engineering, School of Technology, Reykjavík University that this dissertation, entitled „Supervised-Learning-Enabled EM-Driven Development of Low Scattering Metasurfaces", submitted by Muhammad Abdullah, be accepted as partial fulfillment of the requirements for the degree of Doctor of Philosophy (Ph.D.) in Engineering.
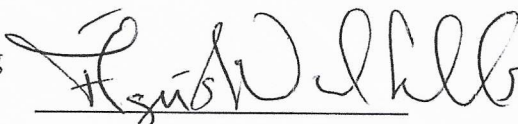
Thesis Committee:

Slawomir Koziel, Professor
Reykjavík University, Reykjavík, Iceland

Anna Pietrenko-Dabrowska, Associate Professor
Gdansk University of Technology, Poland

Ágúst Valfells, Chair of Department of Engineering
Reykjavík University, Reykjavík, Iceland

Ubaid Ullah, Assistant Professor
Al-Ain University, UAE

Thesis Examiner:

Adam Narbudowicz, Senior Research Fellow
Trinity College Dublin, Ireland